

PREPARED FOR SUBMISSION TO JCAP

Background model systematics for the Fermi GeV excess

Francesca Calore,^a Ilias Cholis^b and Christoph Weniger^a

^aGRAPPA, University of Amsterdam, Science Park 904, 1090 GL Amsterdam, Netherlands

^bFermi National Accelerator Laboratory, Center for Particle Astrophysics, Batavia, IL 60510, USA

E-mail: f.calore@uva.nl, cholis@fnal.gov, c.weniger@uva.nl

Abstract. The possible gamma-ray excess in the inner Galaxy and the Galactic center (GC) suggested by *Fermi*-LAT observations has triggered a large number of studies. It has been interpreted as a variety of different phenomena such as a signal from WIMP dark matter annihilation, gamma-ray emission from a population of millisecond pulsars, or emission from cosmic rays injected in a sequence of burst-like events or continuously at the GC. We present the first comprehensive study of model systematics coming from the Galactic diffuse emission in the inner part of our Galaxy and their impact on the inferred properties of the excess emission at Galactic latitudes $2^\circ < |b| < 20^\circ$ and 300 MeV to 500 GeV. We study both theoretical and empirical model systematics, which we deduce from a large range of Galactic diffuse emission models and a principal component analysis of residuals in numerous test regions along the Galactic plane. We show that the hypothesis of an extended spherical excess emission with a uniform energy spectrum is compatible with the *Fermi*-LAT data in our region of interest at 95% CL. Assuming that this excess is the extended counterpart of the one seen in the inner few degrees of the Galaxy, we derive a lower limit of 10.0° (95% CL) on its extension away from the GC. We show that, in light of the large correlated uncertainties that affect the subtraction of the Galactic diffuse emission in the relevant regions, the energy spectrum of the excess is equally compatible with both a simple broken power-law of break energy $E_{\text{break}} = 2.1 \pm 0.2 \text{ GeV}$, and with spectra predicted by the self-annihilation of dark matter, implying in the case of $\bar{b}b$ final states a dark matter mass of $m_\chi = 49^{+6.4}_{-5.4} \text{ GeV}$.

Contents

1	Introduction	2
2	Data analysis	4
2.1	Data selection	4
2.2	Statistical framework	5
2.3	Adopted templates	7
3	Galactic diffuse emission models	9
3.1	Building GDE models with Galprop	10
3.2	The explored parameter space	13
3.3	Discussion about the template approach	16
4	Non-parametric analysis of the Galactic center excess	20
4.1	Theoretical model systematics	20
4.2	Empirical model systematics	25
4.2.1	Analysis of test regions along the Galactic disk	26
4.2.2	The covariance matrix of empirical model systematics	27
4.2.3	Other systematics and the GCE spectrum	28
4.3	The morphology from ten sky segments	29
5	Parametric fits to the Galactic center excess	31
5.1	Spectral fits with correlated errors	34
5.2	Dark Matter models	34
5.3	Astrophysical models	36
6	Discussions	38
6.1	Astrophysical interpretations	38
6.2	A signal from dark matter annihilation?	41
6.3	The energy spectrum at sub-GeV energies	42
7	Conclusions	43
A	Description of Galactic diffuse models	46
B	Further properties of the Galactic center excess	51
B.1	Characterization of the morphology	51
B.2	Correlation with <i>Fermi</i> bubbles	52
C	Systematic uncertainties	54
C.1	An analytical model for the empirical model uncertainty	54
C.2	Various method uncertainties	55
D	Miscellaneous	56

1 Introduction

The study of Galactic cosmic rays (CRs) and gamma-ray physics has been a very active field in the last few decades with the launch of PAMELA [1, 2], AMS-02 [3] aboard the International Space Station (ISS) and, in particular, of the Large Area Telescope (LAT) aboard the Gamma-Ray Space Telescope (*Fermi*) [4]. The latter has produced the most detailed maps of the gamma-ray sky ever, in a wide energy range and with good energy and angular resolution [5]. The interaction of Galactic CRs with the interstellar medium (ISM) results in the diffuse emission from the Milky Way, which is the brightest source of gamma rays seen with the *Fermi*-LAT. Thus, the *Fermi*-LAT data provide an important handle for understanding the origin and the propagation of CRs in our Galaxy. This is complemented by measurements in microwaves [6, 7], X-rays [8], lower energy [9] and higher energy gamma rays [10–12], and neutrinos [13].

More specifically, focused studies of known Galactic sources in gamma rays by both the *Fermi*-LAT and Atmospheric Cherenkov Telescopes (ACTs), together with measurements in X-rays, microwaves and now neutrinos, have helped us in studying and modeling the source properties and the primary CRs composition injected [14–22] by for example supernova remnants (SNRs) and pulsars. Moreover, the analysis of gamma-ray data has led to the discovery of the *Fermi* bubbles [23, 24], which are believed to be the inverse Compton scattering (ICS) counterpart [23] of the WMAP haze [25, 26], recently observed also with Planck [27].

In addition, the unprecedented energy and angular resolution of *Fermi*-LAT, combined with an energy range of more than three orders of magnitude (30 MeV to 500 GeV) and the large field of view, have led to a revolution in the measurement of the gamma-ray properties for specific classes of objects such as active Galactic nuclei [28, 29], star-forming galaxies [30–32] and millisecond pulsars (MSPs) [33–35]. For the latter class of objects very few detections and even fewer spectral measurements had been made at gamma-ray energies. Those same properties of the LAT instrument have also facilitated an unprecedented measurement of the isotropic gamma-ray background (IGRB) [36, 37] and, for the first time, of its power-spectrum [38]. These measurements have improved our understanding of extragalactic astrophysical objects [32, 37, 39–41] and ultra-high-energy CRs [42–44].

A wide range of cosmological and astrophysical observations have shown that about 85% of the matter content in the Universe is non-baryonic, dark and cold [45]. The currently leading candidates for this *dark matter* (DM) are Weakly Interacting Massive Particles (WIMPs), which appear in a large number of scenarios of beyond-the-Standard Model physics [46–48]. The ‘freeze-out mechanism’ that sets their abundance in the early Universe provides clear predictions for the self-annihilation rate of these particles today. Their annihilation products could contribute to the cosmic- and gamma-ray fluxes observed at Earth with rates that are tantalizingly close to the sensitivity of current experiments.

Recently, a number of groups searching for DM signals have analyzed the gamma-ray emission from the inner few degrees around the Galactic center (GC), and either claimed [49–56] or refuted [57] the existence of an extended diffuse and spherical emission component on top of the standard astrophysical backgrounds. It was found that the excess emission is compatible with a radial volume emissivity profile $\propto r^{-\Gamma}$, with Γ in the range 2.2 [52] to 2.4 [53], and with r denoting the Galacto-centric distance. Furthermore, it was demonstrated that the excess features an energy spectrum that peaks at a few GeV and is broadly consistent

with a signal from DM annihilation, although other source spectra (a log-parabola or a power-law with exponential cutoff) can be accommodated by the data, see e.g. refs. [50, 53, 54].

However, the modeling of the Galactic diffuse emission (GDE) is very uncertain in the inner few hundred pc of the GC (150 pc projected distance corresponds to about 1°), and is strongly affected by systematics related to point source subtraction and the modeling of diffuse backgrounds [54, 57, 58]. Complementary observations, like local measurements of CRs, are not able to set strong constraints on the CR propagation properties or gas densities in that region. Moreover, the magnetic field intensity can be only indirectly constrained by the synchrotron emission at microwaves (or the dispersion measures) for given assumptions on high (low) energy electrons. Indeed, given the high density of astrophysical objects and CRs at the GC, and the unprecedented sensitivity of *Fermi*-LAT, it seems far from surprising that residuals were found above the astrophysical emission that had been anticipated [58, 59].

If the observed GC excess is indeed caused by the annihilation of DM particles (which is a very exciting but also exotic possibility), it should visibly extend tens of degrees above and below the GC [60, 61]. The solid confirmation of an excess emission with the *same* spectral properties as observed in the inner few degrees around the GC is hence a necessary (though not sufficient) criterion for the interpretation of the excess at the GC in terms of DM annihilation, and as such of utmost importance. The first claim that such an extension to high latitudes, up to tens of degrees, is indeed observed in the *Fermi*-LAT data (most notably in the *Fermi* bubble regions [24], which happen to have a good signal-to-noise for DM signals), was put forward in ref. [62], and reproduced in refs. [55, 63]. Nonetheless, also this high latitude region is extremely difficult to analyze, mainly because of the dominant background represented by gamma rays originating from the interactions of CRs with the ISM and photon fields.

Besides its status as a “compelling case for annihilating DM” [55], the GC excess emission has also been interpreted in terms of various astrophysical processes. Firstly, the excess gamma-ray emission could originate from a population of gamma-ray MSPs associated with the central stellar cluster and not yet detected by the *Fermi*-LAT [54, 64–66] (as already suggested in ref. [67] years ago using EGRET data). Recently, several arguments disfavor the MSPs hypothesis, suggesting that only up to 5–10% of the observed emission can originate from MSPs [68–70].

Another possible explanation of the GC excess relies on the interactions of CRs with gas, for example non-thermal bremsstrahlung from a population of electrons scattering off neutral molecular clouds in the inner 2° [71], or interactions between the gas and protons accelerated by the super-massive black hole sitting at the GC [72]. In general, those mechanisms would lead to an excess emission correlated with the gas distribution itself. In particular, the former process could not only explain part of the GeV excess emission in the Galactic ridge region, but also the excess at TeV energies as seen by HESS [73, 74]. However, in both cases an extended signal up to a few kpc is excluded, unless a large amount of unidentified spherically distributed gas is present at the GC. It has also been suggested that burst-like events during an active past of our Galaxy may represent a viable mechanism for producing gamma rays in the inner Galaxy with the observed spectrum and morphology. Hadronic [75] or leptonic [76] scenarios might explain some of the observed excess features at high latitudes.

In this paper, we will reanalyze the *Fermi*-LAT gamma-ray data at high Galactic latitudes. We will consider a Region Of Interest (ROI) at Galactic latitudes $2^\circ \leq |b| \leq 20^\circ$

and Galactic longitudes $|\ell| < 20^\circ$, which we refer to as the *inner Galaxy* throughout. This region avoids the inner 2 degrees of the Galactic disk, which is the region of the sky that is most contaminated with strong gamma-ray point sources and large uncertainties in the diffuse emission.

The aims of this paper are the following: *i*) to robustly confirm the existence of an extended excess emission in the inner Galaxy on top of the standard astrophysical background, henceforth the *Galactic center excess* (GCE); *ii*) to characterize its spectral and morphological properties and its status as the extended counterpart of the excess seen at the GC; and *iii*) to investigate in a comprehensive manner the systematic uncertainties related to the modeling of diffuse backgrounds. To this end, we study *theoretical* model systematics, which are related to variations in the different possible models for the GDE, and *empirical* model systematics, which we estimate by an analysis of residuals from a large number of test regions along the Galactic disk.

We adopt template-based multi-linear regression techniques to fit the *Fermi*-LAT data in our ROI. To this end, we model the GDE from the Milky Way based on physical models for the production and propagation of CRs in the Galaxy. By means of the `Galprop` code, we build a large set of GDE models with the aim of spanning the full range of possible physical conditions that affect the gamma-ray emission coming from direction of the inner Galaxy. Each background model is then tested against *Fermi*-LAT data during the fitting procedure.

Two criteria guide our search for GDE models for the inner Galaxy: *a*) a *good statistical fit*, i.e. small TS values, where $TS \equiv -2 \ln \mathcal{L}$ throughout; and *b*) *self-consistency*, i.e. agreement between the predicted and measured levels of the individual GDE components (this is not guaranteed in a template fit, where spectra can vary arbitrarily).

The paper is organized as follows: In section 2 we discuss the data reduction, the statistical methods and the modeling of some of the backgrounds. Section 3 is dedicated to a detailed explanation about how we model the main components of the Galactic diffuse emission. In section 4 we then present the results on the spectrum and morphology of the excess emission, and estimate theoretical and empirical model systematics. We perform parametric fits to the data in section 5, and leave our discussion to section 6. Finally, in section 7 we state our conclusions.

2 Data analysis

In this work, we study gamma rays collected by the *Fermi*-LAT from the inner Galaxy with template-based multi-linear regression techniques, see e.g. ref. [23, 24]. The main difference with respect to previous studies is an extensive treatment and discussion of systematics related to the modeling of the GDE, and an incorporation of these uncertainties in the final spectral and morphological fits to the GCE. In addition, we introduce a few technical improvements, including a weighted adaptive masking of point sources, the proper treatment of the point-spread-function (PSF) of *Fermi*-LAT, and the non-logarithmic binning of energies which facilitates flux measurements at high energies.

2.1 Data selection

In our analysis, we use 284 weeks of reprocessed *Fermi*-LAT data (starting from 4 Aug 2008) with energies between 300 MeV and 500 GeV.¹ We apply the standard zenith-angle

¹See <http://fermi.gsfc.nasa.gov>.

cut $\theta < 100^\circ$ in order to avoid contamination from the Earth limb, and the recommended `gtmktime cut (DATA_QUAL>0) && (LAT_CONFIG==1)`. To maximize the available number of photons at high energies we use front- and back-converted `P7REP_CLEAN` events.² The initial event selection and the calculation of exposure maps is done using the standard `Fermi ScienceTools v9r32p5` with the instrument response functions (IRFS) `P7REP_CLEAN_V15`.

We use the `healpix` projection for the spatial binning of data [78]. The `healpix` grid is a hierarchical equal-area iso-latitude pixelization of the sphere, and it is well suited for full-sky analyses of astronomical data. In our work, we adopt the resolution parameter $n_{\text{size}} = 256$, which corresponds to a pixel size of 1.598×10^{-5} sr (roughly 0.23° edge length for square pixels). All mask definitions in this paper refer to the pixel center as defined in the `healpix` grid, leading to $\pm \sim 0.1^\circ$ variations at the mask edges.

As noted above, the baseline ROI of this work, which we refer to as *inner Galaxy*, is defined as

$$|\ell| \leq 20^\circ \quad \text{and} \quad 2^\circ \leq |b| \leq 20^\circ, \quad (2.1)$$

where ℓ and b are the Galactic longitude and latitude, respectively. As discussed above, the lower latitude cut is applied to reduce contamination with diffuse and point source emission from the Galactic disk. The overall region is kept small (compared to previous analyses [55, 62]) in order to avoid biasing our analysis results by potential mis-modeling of the diffuse emission in regions of the sky that are irrelevant for the GCE. However, we will use a number of additional ROIs for validation tests as well as for estimates of model systematics.

In contrast to previous studies, we use energy bins that increase in logarithmic size with energy. This will partially counterbalance the reduced photon statistics that usually complicate the analysis at energies above 10 GeV. To this end, we define energy bins such that for a given photon flux with a spectral index of Γ , each bin contains an equal number of expected events. For a given energy range $E_0 \equiv E_{\text{min}}$ to E_{max} , and a given number of bins n_{bins} , we find that the boundaries of these energy bins can be recursively determined by

$$E_{j+1} = \left(E_j^{1-\Gamma} - \frac{E_{\text{min}}^{1-\Gamma} - E_{\text{max}}^{1-\Gamma}}{n_{\text{bins}}} \right)^{\frac{1}{1-\Gamma}}, \quad \text{with} \quad j = 0, 1, \dots, n_{\text{bins}}. \quad (2.2)$$

In the present analysis, we use $n_{\text{bins}} = 20$ bins in the range 500 MeV to 500 GeV and adopt the value $\Gamma = 1.45$, which is harder than the actual spectrum. This is a compromise between a loss in statistics at high energies on the one hand, and unreasonably wide energy bins on the other hand. Furthermore, we add four linearly spaced energy bins between 300 and 500 MeV.

2.2 Statistical framework

We use the maximum likelihood technique for parameter inference and confidence interval estimation. To this end, we adopt a weighted Poisson likelihood function for the photon data [79],

$$-2 \ln \mathcal{L} = 2 \sum_{i,j} w_{i,j} (\mu_{i,j} - k_{i,j} \ln \mu_{i,j}) + \chi_{\text{ext}}^2, \quad (2.3)$$

²We leave an analysis based on a subset of events with better angular resolution at sub-GeV energies for future work [77].

where $\mu_{i,j}$ and $k_{i,j}$ are, respectively, the expected and observed number of photons in the i^{th} energy bin and j^{th} pixel, and χ_{ext}^2 allows for external constraints on the model parameters. The definition of the point source (PSC) mask weights $w_{i,j} \in [0, 1]$, as well as of the external constraints χ_{ext}^2 , will be discussed below.

The expected number of photons is given by the sum of different space- and sometimes energy-dependent templates that represent: *i*) the GDE (tying π^0 and bremsstrahlung components together, cf. section 3 for details), *ii*) the *Fermi* bubbles, *iii*) the IGRB, *iv*) the emission from the detected PSCs in the *Fermi*-LAT Second Source catalogue (2FGL) [80], and *v*) a spherically symmetric profile, centered at the GC that accounts for the GCE excess emission (cf. section 2.3). We leave the normalization of each model component free to float in each energy bin. The total model is defined by

$$\mu_{i,j} = \sum_k \theta_{i,k} \mu_{i,j}^{(k)}, \quad (2.4)$$

where $\theta_{i,k}$ is the normalization of component k in energy bin i , and $\mu_{i,j}^{(k)}$ is the predicted number of events of component k when $\theta_{i,k} = 1$.

External constraints will be adopted both for the IGRB and for the *Fermi* bubbles, which we leave free to float in our analysis, but which can be more efficiently determined in regions outside of our ROI. The constraints are assumed to be Gaussian, such that χ_{ext}^2 is of the form

$$\chi_{\text{ext}}^2 = \sum_{i,k} \left(\frac{\phi_{i,k} - \bar{\phi}_{i,k}}{\Delta\phi_{i,k}} \right)^2, \quad (2.5)$$

where $\phi_{i,k}$ denotes the predicted flux of component k in energy bin i , and $\bar{\phi}_{i,k}$ and $\Delta\phi_{i,k}$ are the externally supplied mean and standard deviation (see section 2.3).

We obtain the best-fit model parameters by minimizing $-2 \ln \mathcal{L}$ with respect to all parameters, using the minimizer `Minuit`.³ For the template analysis, we derive error bars from the covariance matrix of $-2 \ln \mathcal{L}$, and checked that our results remain essentially unchanged when using the more accurate (but much more time-consuming) `minos` algorithm in `Minuit`. Note that we allow negative values of $\theta_{i,k}$ in our fits, which improves the stability of `Minuit` without affecting our conclusions.

The finite angular resolution of the LAT is incorporated by following the prescription described in ref. [58]. Using `healpix`, we decompose the skymap into spherical harmonics, re-weight the moments according to the decomposition of the *Fermi*-LAT PSF (taking the GC as reference position), and then transform them back to sky coordinates. This method is used for all diffuse emission components, except the GCE templates (which remains non-smoothed for simplicity), and the PSC templates (which we instead smooth using the more accurate `gtmodel` from the *Fermi ScienceTools*). We found that our results are not significantly affected by the details of the smoothing (more specifically, neglecting smoothing of the diffuse components entirely or smoothing them instead with a fixed-width Gaussian with 2° FWHM induces changes in the spectra at the % level).

In order to minimize the impact of known point sources on our analysis, we use a ‘soft’ PSC mask, with values that can range from zero to one. In practice, this mask acts as an

³See <http://seal.web.cern.ch/seal/MathLibs/Minuit2/html/>.

energy-dependent re-weighting of the exposure and the associated count numbers in different regions of the sky. The corresponding reweighting factor, $w_{i,j}$, enters eq. (2.3) as a simple prefactor that multiplies the likelihood contributions from individual pixels. In the Gaussian limit, this corresponds to increasing statistical errors by a factor $w_{i,j}^{-1}$.

The weights are defined as follows. We infer the expected number of photons from PSCs, $\mu_{i,j}^{\text{PSC}}$, in different pixels and energy bins by creating a model map that contains all point sources of the 2FGL [80], fixing their fluxes to the best-fit parameters of the catalogue. We compare these numbers with the expected number of background events from the GDE (including only the π^0 , ICS and Bremsstrahlung components at their nominal normalization), $\mu_{i,j}^{\text{BG}}$. For definiteness, we take the model P.⁴ The weights are defined by

$$w_{i,j} = \frac{1}{\left(\frac{\mu_{i,j}^{\text{PSC}}}{f_{\text{PSC}} \mu_{i,j}^{\text{BG}}} \right)^{\alpha_{\text{PSC}}} + 1}, \quad (2.6)$$

where f_{PSC} denotes the threshold of the fraction of point source contamination above which a pixel is masked, and α_{PSC} parameterizes the smoothness of the transition between $w = 0$ and $w = 1$. As default values, we select $\alpha_{\text{PSC}} = 5$ and $f_{\text{PSC}} = 0.1$. We discuss the systematics related to our choices concerning the PSC mask definition in section 4.1.

We emphasize that we apply the PSC mask *only* when performing fits and calculating likelihood values. The calculation of *fluxes* integrated over our ROI, as shown in various figures throughout the paper, remains unaffected by the PSC mask, in order to simplify comparison with other work. Furthermore, as described below, we include as a default template in all analysis steps the PSC flux derived from all of the 2FGL point sources with a normalization that is fixed to one. By construction, the 2FGL sources do not affect the fits to the data, but they contribute to the overall flux in our ROI and indicate where PSC are relevant and where not.

2.3 Adopted templates

The PSC template is derived from the 2FGL [80], as described above. The GDE templates will be extensively discussed in section 3. We describe here briefly the remaining spatial templates that we use in our analysis and highlight their main characteristics.

***Fermi* bubbles.** In our main analysis, we model the emission of the *Fermi* bubbles as flat within the region defined in ref. [24]. We will discuss the impact of a possible latitude dependence of the *Fermi* bubbles emission in appendix B.2.

As mentioned in section 2.2, when performing fits in our main ROI, which is relatively small and does not include the whole *Fermi* bubbles template, we introduce an additional external constraint on the bubbles flux implemented as in eq. (2.5). Mean and standard deviations are taken from measurements in ref. [81], where the errors incorporate systematics related to the uncertainties in the GDE.⁵

⁴We refer to appendix A for the definition of model parameters. It represents the reference model of ref. [58].

⁵During the final stages of our work, the first *Fermi* bubbles analysis by the *Fermi*-LAT Collaboration has been released [83]. Data above 10° in latitude have been analyzed and the spectrum and morphology of the *Fermi* bubbles have been derived. Since we do use preliminary results of this analysis to constrain the bubbles spectrum, we do not expect a large variation of our results due to the imposed bubbles spectral shape.

Name	Notes	Ref.
PSC	Spectra fixed to 2FGL	[80]
<i>Fermi</i> bubbles	Flat emission — Spectrum constrained	[24, 81]
IGRB	Constant emission — Spectrum constrained	[37]
GCE	Generalized NFW profile with inner slope γ	—
Ackermann+ GDE models ($\times 13$)	$(\pi^0 + \text{Bremss}) + \text{ICS}$	[58]
Additional GDE models ($\times 47$)	$(\pi^0 + \text{Bremss}) + \text{ICS}$	This work

Table 1. Different templates and models used throughout the analysis. We construct the models in the bottom row by using the `Galprop v54` code [82]. As indicated, in our template analysis we tie both the bremsstrahlung and π^0 components together, “ $\pi^0 + \text{Bremss}$ ”, and vary them simultaneously by a common factor. Furthermore, we will split the GCE (ICS) templates in 10 (9) different segments during the morphology analysis in section 4.3.

IGRB. Fits within our main ROI do not well constrain the very subdominant IGRB emission. We hence constrain this component – similarly to what we do for the *Fermi* bubbles – by introducing additional terms in the likelihood function, with mean values and standard deviations (which include statistical errors and systematical errors from the GDE and other sources) as given in ref. [37].

GCE template. Throughout most of our analysis (except for the morphology studies in sections 4 and 5 and appendix B), we will parametrize the volume emissivity of the GCE in terms of the spherically symmetric⁶ generalized NFW profile, as given by

$$\rho(r) = \rho_s \frac{(r/r_s)^{-\gamma}}{(1 + r/r_s)^{3-\gamma}}, \quad (2.7)$$

squared. This is clearly motivated by the DM annihilation interpretation of the GCE. We will use the common normalization $\rho(r_\odot) = 0.4 \text{ GeV}/\text{cm}^3$ at the position of the Sun and a scale radius of $r_s = 20 \text{ kpc}$ to ease of comparison with previous results in the literature. If not stated otherwise, we will furthermore adopt the value $\gamma = 1.2$, which is compatible with previous (see e.g. refs. [55, 62]) and our own findings below.

In general, the gamma-ray flux ($\text{GeV}^{-1} \text{ cm}^{-2} \text{ s}^{-1} \text{ sr}^{-1}$) from self-conjugate DM particles, χ , annihilating in the Galactic DM halo is given by

$$\frac{dN}{dE} = \frac{\langle \sigma v \rangle}{8\pi m_\chi^2} \frac{dN_\gamma}{dE} \int_{\text{l.o.s.}} ds \rho^2(r(s, \psi)), \quad (2.8)$$

where m_χ is the DM mass, $\langle \sigma v \rangle$ the velocity averaged total annihilation cross-section, dN_γ/dE the averaged energy spectrum of photons produced per annihilation, and $\rho(r)$ the radial DM energy density distribution as function of the Galacto-centric distance r . The coordinate $s \geq 0$ runs along the line-of-sight and is related to the distance from the GC by $r(s, \psi) = \sqrt{(r_\odot - s \cos \psi)^2 + (s \sin \psi)^2}$, where ψ is the angular distance from the GC and $r_\odot = 8.5 \text{ kpc}$ denotes the distance between Sun and GC.

⁶Although the DM profile is generally assumed to be spherically symmetric, N-body simulations predict some degree of tri-axiality of the halos in their inner part, see for example ref. [84] for a recent discussion. In this case, an elongation of the DM associated emission would be expected towards a specific direction. We discuss the elongation of the measured excess in appendix B.

3 Galactic diffuse emission models

The observed gamma rays with energies above 100 MeV typically originate from CRs that propagate in the Galaxy. Firstly, CR nuclei produce via inelastic nucleon-nucleon collisions with the interstellar gas neutral mesons (mainly π^0 s), which subsequently decay to gamma-ray pairs [82, 85, 86]. This is typically, and throughout this work, referred to as the π^0 Galactic diffuse component. Secondly, CR electrons interact with the interstellar gas, giving rise to bremsstrahlung emission [87–89], which can be a significant diffuse gamma-ray component below a few GeV in the gas-rich regions of our Galaxy. Finally, CR electrons up-scatter low-energy photons via ICS into the gamma-ray energy regime [89, 90]. ICS, bremsstrahlung and π^0 constitute the three components of the GDE. Various ingredients enter the evaluation of these three GDE components, which we will discuss in the remainder of this section.

Firstly, the exact distribution of the CR sources is very important. This is especially true for electrons because they lose energy quickly, such that their distribution in the Galaxy – at higher energies – is strongly correlated to their initial injection (i.e. acceleration and production) region.⁷ In addition, the assumptions on the diffusion scale height of the Galaxy, the diffusion coefficient⁸ $D(= \frac{1}{2}\lambda c)$ and its dependence on CR rigidity (which together set the time scale nuclei of a given rigidity stay in the Galaxy before escaping to the intergalactic medium) can strongly affect the diffuse components. The large scale assumptions about diffusion, convection and re-acceleration can strongly impact – and are thus constrained by – the CR spectra [91–93] that we measure locally. The same applies for the large scale (angular and spatial) gamma-ray spectra [58, 94, 95], which, in turn, impact any indirect DM search, either in antiprotons [96–98], positrons [99] or gamma-rays [100].

Furthermore, the exact assumptions on the gas distribution in the inner Galaxy, which is the target of CRs responsible for the π^0 and the bremsstrahlung emission, affect in a direct manner the gamma-ray observations. The main constituent of the interstellar gas is the atomic hydrogen (HI) traced by its 21 cm line emission [101, 102], while the other important component of the ISM gas is the molecular hydrogen (H₂), which is traced indirectly by the 2.6 mm line emission from CO [103]. Additionally, since CR electrons of energies $\mathcal{O}(1)$ GeV and above suffer from fast energy losses due to synchrotron and ICS, the exact assumptions on the magnetic field distribution and the interstellar radiation field (ISRF) in the region of interest is of vital importance. In this context, magnetic fields, which have a random and an ordered component at every position of the Galaxy, can affect both the synchrotron electrons losses, which are important above few GeV in energy, and the way CRs diffuse especially in regions with strong ordered magnetic fields (see ref. [104] for an example on the impact magnetic fields can have on causing anisotropic diffusion of CRs and its impact on potential gamma-ray signals from DM). The ISRF assumptions matter for a second reason, namely the fact that those photons are the target of CR electrons that up-scatter them to the observed gamma-ray energy regime.

Emission directly correlated with the GC or the inner Galaxy comes only from the inner 1–2 kpc of the Galaxy where the CRs propagation conditions can be very different from those locally. For example, one may need to consider the impact of potentially strong convective winds that could exist in that region and could be associated to the *Fermi* bubbles. Moreover,

⁷CR electrons are of different origin: They are diffusive shock accelerated ISM electrons at SNRs, secondaries from inelastic pp and pHe collisions (predominantly), and electrons produced in pulsars magnetospheres and further accelerated at the termination shock of Pulsar Wind Nebulae (PWNe).

⁸Assuming that CRs diffuse isotropically in the Galaxy, λ is the diffusion length.

CR diffusive re-acceleration may be different in that part of the Galaxy compared to the local environment. In fact, the propagation conditions in the inner Galaxy can have only a very mild effect on the local CR spectra, which instead depend much more on the assumptions regarding, for example, the spiral arms (see for instance ref. [105]), and are hence only weakly constraint.

In the following subsection we describe how the GDE can be modeled starting from the fundamental ingredients of production and propagation of CRs in the Galaxy. By using the **Galprop** code and varying the physical parameters at stake, we build a set of GDE models in order to explore physical scenarios for such a gamma-ray background. We discuss the parameter ranges that are considered and the main assumptions of this approach. Finally, we will discuss typical template variations that different assumptions on the GDE components can lead to.

3.1 Building GDE models with Galprop

In our analysis, we make use of the **Galprop v54** code [106–108] to produce gamma-ray templates for the GDE at various energies. Additionally we download the **healpix** GDE π^0 , bremsstrahlung and ICS component maps from some of the models of ref. [58], which were also produced with **Galprop v54**. We refer for further details to ref. [58]. We will briefly summarize the properties of the adopted GDE models here, and provide more details in appendix A.

CR sources are assumed to be distributed with a rotational symmetry on the disk, with varying radial dependence. Their distribution can either follow the distribution of SNRs, pulsars, OB stars (see ref. [58]) or combinations of them. The primary CR electrons, protons and nuclei are then injected into the interstellar medium with a power-law $dN/dE_{\text{kin}} = E_{\text{kin}}^{-\alpha}$, which can vary between species and with kinetic energy (per electron or nucleon) E_{kin} .⁹ For the Galactic gasses, as we described, there are two major neutral hydrogen components HI and H2 and a subdominant contribution of ionized hydrogen HII. These are all modeled as separate components, with H2 suffering from the fact that a conversion from CO to H2 has to be performed (see refs. [103, 107]).¹⁰

Diffusion of CRs in the Galaxy is assumed to be homogeneous and isotropic within a cylindrical volume of $r \leq r_D$ and $|z| \leq z_D$, where z and r parametrize the position along the longitudinal and polar axes. It is described by a scalar diffusion coefficient depending on rigidity R as

$$D(R) \equiv D_{xx}(R) = D_0 \left(\frac{R}{4\text{GV}} \right)^\delta, \quad (3.1)$$

where D_0 is the diffusion coefficient at 4 GV and δ is the diffusion index with values between 0.3–0.6.¹¹ Diffusive re-acceleration in turn is connected to spatial diffusion through a simple relation

$$D_{pp}(R) = \frac{4}{3\delta(2-\delta)(4-\delta)(2+\delta)} \frac{R^2 v_A^2}{D_{xx}(R)}, \quad (3.2)$$

⁹We include all species up to Carbon stable isotopes (Iron for the models of ref. [58]) and take the CR protons and heavier CR nuclei to have the same injection indices.

¹⁰For the GDE models that we built ourselves, we use the conversion factor X_{CO} profile from ref. [109], while the models from ref. [58] come with their own X_{CO} profiles. Given that most of the H2 emission close to the inner Galaxy is actually masked by our low latitude cut $|b| > 2^\circ$, the precise radial dependence of X_{CO} is of little relevance here.

¹¹ δ can vary with rigidity but for our work we keep it fixed to 1/3.

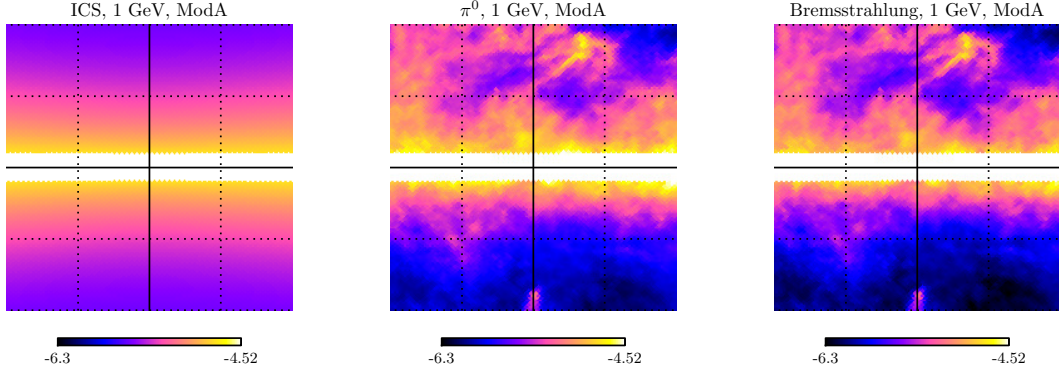


Figure 1. Predicted emission for the GDE components of model A. From *left to right*: ICS, π^0 , and bremsstrahlung. The fluxes are shown in the $40^\circ \times 40^\circ$ sky-region, centered at the GC and masking out $|b| < 2^\circ$. The corresponding units are $\log_{10}(\text{GeV}^{-1} \text{cm}^{-2} \text{s}^{-1} \text{sr}^{-1})$.

with v_A being the Alfvén speed.

Convection is considered to be taking place perpendicularly away from the Galactic disk, with the convection velocity being zero on the disk but having a gradient dv/dz . The Galactic magnetic field responsible for synchrotron losses of CR electrons is assumed to have a cylindrical symmetry with the parametrization

$$B(r, z) = B_0 e^{(r_\odot - r)/r_c} e^{-|z|/z_c}, \quad (3.3)$$

where B_0 is the local magnetic field and r_c and z_c are the radial and longitudinal extension, respectively (r_\odot is 8.5 kpc).

Finally, the ISRF is built from the contribution of many stellar components and includes the effects of absorption and re-emission from dust grains (see ref. [107] for further details and ref. [110] for a description on how it is constructed). Within the code the ISRF is divided into three basic components, related to the direct emission from stars, dust grains and CMB. The user is free to vary the normalization of each of these components.

In figure 1, we show the typical morphology of the three different diffuse emission components at 1 GeV from a model, model A, which has parameters that are defined in table 2. We will refer to model A as our reference model for further discussions, since as we will see below it well describes the gamma-ray data and spectra in the inner Galaxy. The left panel of figure 1 refers to the ICS emission, which is smooth and depends mainly on the electron distribution and the properties of the B -field and the ISRF. On the other hand, π_0 (middle) and bremsstrahlung (right) morphologies trace directly the distribution of the gas and depend mainly on the proton and electron CR densities, as well as on the properties of CR diffusion, re-acceleration and convection.

The observed emission as shown in figure 1 receives contributions from all distances along the line-of-sight. However, whether the overall emission is dominated by locally produced gamma rays (within a few kpc), or by gamma rays from the GC, is a strong function of the Galactic latitude. This is illustrated in figure 2, where we show the fractional contributions to the GDE components as function of the line-of-sight for a typical GDE model.¹² We find

¹²To generate this figure, we used our own modified version of `Galprop 54.1.984` where the line-of-sight integration can be restricted. We adopted a simple GDE model defined by the `galdef` file `54.01`.

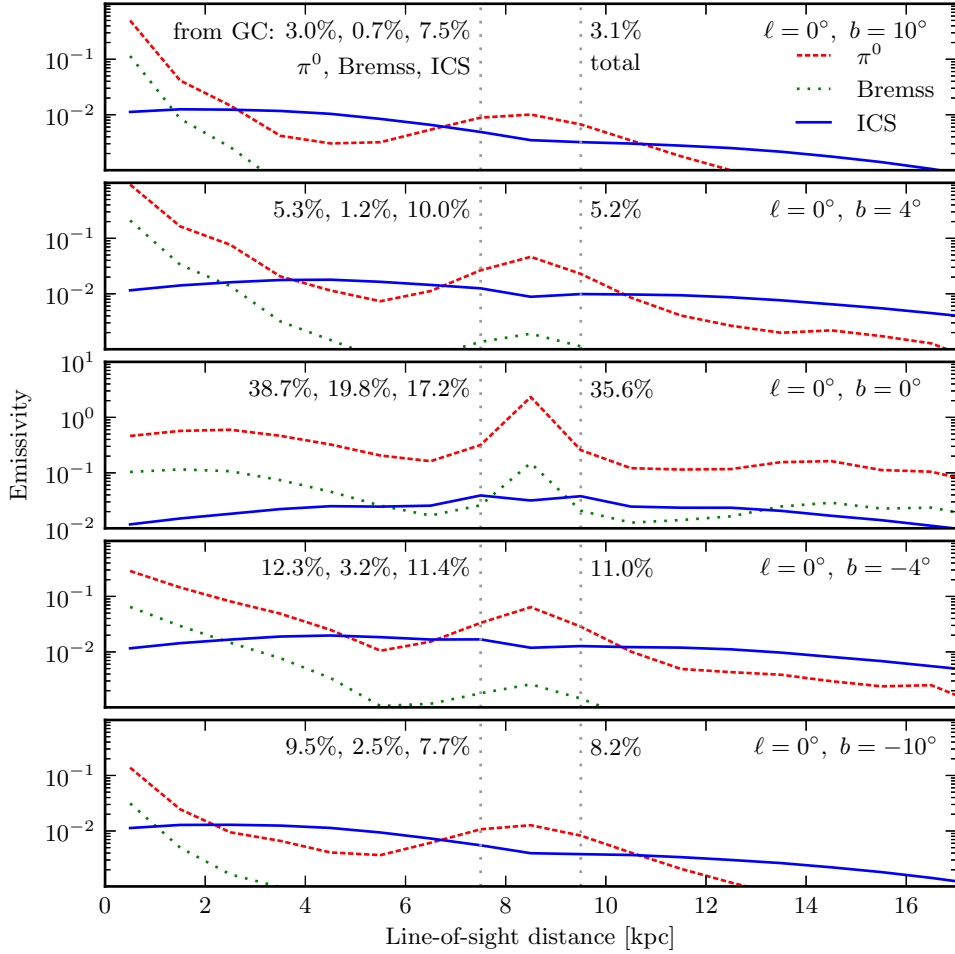


Figure 2. Typical differential volume emissivity $dN/dV/dt/dE$ (in arbitrary units) of the three GDE components along the line-of-sight at five different Galactic latitudes, zero Galactic longitude, and gamma-ray energies of 2.6 GeV. The numbers show the fraction of π^0 , bremsstrahlung, ICS and total emission that comes from the distance range 7.5–9.5 kpc (with the GC being at 8.5 kpc). At latitudes above $|b| \geq 4^\circ$, less than about 11% of the total GDE comes from this central region. Note that the reduced amount of *local* gas in the southern hemisphere leads at negative latitudes to larger relative contributions from the Galactic center.

that in the case of our baseline ROI, less than 14% (and for $|b| \geq 4^\circ$ less than 11%) of the GDE actually comes from regions close to the GC. The main challenge in extracting the GCE in the inner Galaxy is hence to characterize the uncertainties and properties of the *local* gamma ray emissivity.

We close this subsection with a discussion of our model A, which we adopt as a reference model throughout. We *tuned* model A to be “self-consistent” in the sense that, after the fit to the data that we will perform below, the *measured* and *predicted* normalizations of the GDE template components agree with high accuracy (see introduction, and see section 4 below). The purpose of this model is to constitute a proof-of-principle that shows that such a self-consistent model is indeed possible with physically not unreasonable parameters.

However, we note that there are significant degeneracies between the physical assump-

Name	z_D	D_0	v_A	dv/dz	Source	$\alpha_e(\alpha_p)$	$N_e(N_p)$	B -field	ISRF
A	4	5.0	32.7	50	SNR	2.43(2.47)	2.03(5.8)	090050020	1.36,1.36,1.0
B	4	28.0	31.0	0	SNR	2.43(2.39)	1.00(4.9)	105050015	1.4,1.4,1.0
C	4	5.0	32.7	0	SNR	2.43(2.39)	0.40(4.9)	250100020	1.0,1.0,1.0
D	4	5.2	32.7	0	SNR	2.43(2.39)	0.40(4.9)	050100020	0.5,0.5,1.0
E	4	2.0	32.7	0	SNR	2.43(2.39)	0.40(4.9)	050100020	1.0,1.0,1.0

Table 2. The properties of GDE models A–E. Here, z_D is in kpc, while r_D is taken to be 20 kpc. D_0 is in units of $10^{28} \text{ cm}^2 \text{ s}^{-1}$, v_A is in km s^{-1} and dv/dz in $\text{km s}^{-1} \text{ kpc}^{-1}$. The CR electron and proton normalizations are $N_e(N_p)$ in units $10^{-9} \text{ cm}^{-2} \text{ sr}^{-1} \text{ s}^{-1} \text{ MeV}^{-1}$ and refer to the differential flux at E_{kin} of 34.5 and 100 GeV. α_e and α_p are the electron and proton injection indices above rigidities of 2.18 and 11.3 GV, respectively (and are respectively equal to 1.6 and 1.89 below these rigidities). For the gas assumptions we take, $T_S = 150 \text{ K}$ and an E(B-V) magnitude cut of 5 (see discussion in section 3.2). For model A the magnetic field “090050020” denotes in eq. (3.3) $B_0 = 9.0 \mu\text{G}$, $r_c = 5 \text{ kpc}$ and $z_c = 2 \text{ kpc}$ (similarly for the other models). Finally, the three numbers in the “ISRF” column refer to the multiplication factors of the “optical”, “IR” and CMB components of the ISRF model used in `Galprop v54 webrun`.

tions that can have a similar impact on the resulting diffuse gamma-ray spectra. For instance, a harder ICS spectrum could be the result of a harder injection spectrum for the CR electrons, a lower energy loss rate (due to a reduced B -field), a different rigidity dependence of the CR diffusion or a different distribution in the energy density of the ISRF. Thus, we can have different combinations of physical properties leading to self-consistent models.

Our model A adopts a CR electron normalization that is significantly higher (by a factor of 5) than the typical $dN_e/dE \simeq 0.4 \times 10^{-9} \text{ cm}^{-2} \text{ sr}^{-1} \text{ s}^{-1} \text{ MeV}^{-1}$ at $\sim 30 \text{ GeV}$ that is required to fit the *local* CR lepton data. In particular, for the ICS emission at GeV scale gamma-ray energies, the responsible CR electrons have typically energies $\sim 50 \text{ GeV}$ or higher. At these energies, the CR electron fluxes are dominated by the contribution of sources within $\sim 1 \text{ kpc}$ from the Sun’s position and are not very sensitive to higher normalizations in the electron flux at few kpc distances. Thus, a higher CR electrons normalization *along the line-of-sight* and towards the GC is quite well possible. Such a higher flux may be due to some young or middle aged pulsars that lie along that direction, either in the spiral arms or in the inner part of the Galaxy. We note that both the adopted B -field and ISRF have relatively high energy densities. Given the uncertainties along the line-of-sight toward the GC, they are still viable. In fact model A suggests a B -field with an amplitude of $50 \mu\text{G}$ at the GC, which is in agreement with the lower limit of ref. [111]. All the other assumptions of model A are very conventional ones.

3.2 The explored parameter space

Different assumptions on the source distribution, gas distribution, diffusion, re-acceleration, convection, magnetic field distribution and the ISRF in the inner part of the Galaxy (and along its relevant line-of-sight) will lead to different GDE models. The assumptions on all these factors and their associated uncertainties need to be taken into consideration in any study of gamma rays from the inner Galaxy.

To conservatively estimate the impact of these uncertainties on the extraction of the GCE, we systematically explore a large range of model parameters that go beyond what is imposed by CRs measurements, allowing even for extreme scenarios. We are interested in testing uncertainties pertaining to the CR source distribution and injection index, gas

distribution, diffusion scale height and coefficient, re-acceleration, convection and energy losses for the CR electrons. As we will discuss in section 3.3, the uncertainties in the ICS are potentially the most important ones in the search of diffuse excess emission towards the GC. For that reason, we change both the ISRF energy density and the Galactic magnetic field amplitude and profile in a large range. In the present work, we present 60 different GDE models to bracket the uncertainties related to what we discussed above.

Our starting point are the 128 GDE models from ref. [58], which were created using **Galprop v54** to probe different distributions in sources, diffusion scale heights and radii, and different assumptions on the Galactic gasses. CR sources distribution are assumed to follow: *i*) the SNRs distribution of ref. [112] (we will denote it as just “SNR”), *ii*) the pulsar distribution of ref. [113] (“Pls_L” option), or *iii*) the one of ref. [114] (“Pls_Y” option) and *iv*) the distribution of OB stars as described in ref. [115] (“OB” option). For the diffusion scale heights and radii, ref. [58] considers values of $4 \leq z_D \leq 10$ kpc and r_D being either equal to 20 or 30 kpc. Gasses were associated to assumptions on the spin temperature T_S that corrects the opacity of the 21 cm line of the HI gas: a more conventional assumption of $T_S = 150$ K and a more extreme one with $T_S = 10^5$ K. In addition, dust can be taken as an alternative tracer of neutral hydrogen (HI & H2) and allow to model out some of the GDE residuals from π^0 and bremsstrahlung as was first done using EGRET data by ref. [116].¹³ We refer the reader to ref. [58] for further details. In ref. [58] each of these 128 models was fitted to the 21-month full-sky *Fermi*-LAT data as well as the most relevant local CR measurements. We note that the models from ref. [58] were however not optimized for an inner Galaxy study, but provide physical examples that give a good overall fit to gamma-ray and CR data.

In order to avoid redundancies, and since we are interested in exploring more extreme propagation scenarios as described above, we use only 13 of the models from ref. [58] that probe the different choices in sources, r_D , z_D and gas (see appendix A for further details). Having added more of these models in the analysis would have not changed our general results (see also ref. [56] for a discussion on all the 128 models of ref. [58]).

In addition to our selection of 13 models from ref. [58], we generate our own models specifically for this study, using **Galprop v54** (webrun version). Those models explore remaining uncertainties, mainly related to the diffusion coefficient, re-acceleration, convection, ISRF and B -field distributions. For the diffusion coefficient described in eq. (3.1), a conventional value for D_0 in the range of $5\text{--}10 \times 10^{28} \text{ cm}^2 \text{ s}^{-1}$ (at 4GV) is used to fit the CR data and the large scale gamma-ray data. As we discussed earlier, we probe significantly larger ranges for the physical assumptions (which could well be realized in the inner 2 kpc of the Galaxy without affecting much the CR data). Thus for D_0 we take a range between $2\text{--}60 \times 10^{28} \text{ cm}^2 \text{ s}^{-1}$. For the re-acceleration, typical values coming from studying CRs are in the range of $10\text{--}30 \text{ km s}^{-1}$ for the Alfvén speed, while we consider in this work values between 0 and 100 km s^{-1} . For the gradient of convection velocity dv/dz , we allow values between 0 and $500 \text{ km s}^{-1} \text{ kpc}^{-1}$, with CR antiprotons and large scale gamma-ray data not showing any preference for values of $dv/dz > 50 \text{ km s}^{-1} \text{ kpc}^{-1}$ for the Galactic disk [94, 96]. The standard assumption for the ISRF model factors, is “1.0, 1.0, 1.0”, see text in section 3.3. We allow the “optical” and “IR” factors to span between 0.5–1.5 as our extreme options, given the level of complexity of these models. Finally, the magnetic field is known to have a

¹³In ref. [58], two different magnitude cuts (2 or 5) were used on the E(B-V) reddening maps of ref. [117] when fitting to that (dust) map a linear combination of the HI 21 cm line map and the CO line map, which is directly related to the H2 map for a homogeneous conversion factor between the two gasses ($X_{CO} = \text{const.}$).

local value in the (generous) range of 3–10 μG with its r_c and z_c scaling distances providing only a very rough description (see ref. [118] for a discussion on the Galactic magnetic field distribution and uncertainties). Typical **Galprop** assumptions include $B_0 = 5 \mu\text{G}$, $r_c = 10 \text{ kpc}$ and $z_c = 2 \text{ kpc}$ as described in eq. (3.3). Yet, the magnetic field close to the GC is expected to have values as large as 50 μG [111]. We take combinations of B_0 , r_c and z_c that allow values for the magnetic field at the GC as low as 5.8 μG and as high as 117 μG with $5 \leq r_c \leq 10 \text{ kpc}$ and $1 \leq z_c \leq 2 \text{ kpc}$. Also, we include the possibility of a significantly higher/lower CR electron population than what is measured locally.

We summarize the parameter ranges as follows:

- geometry of the diffusion zone: $4 \leq z_D \leq 10 \text{ kpc}$ and $r_D = 20 \text{ or } 30 \text{ kpc}$;
- source distributions: SNR, pulsars, OB stars;
- diffusion coefficient at 4 GV: $D_0 = 2 - 60 \times 10^{28} \text{ cm}^2 \text{ s}^{-1}$;
- Alfvén speed: $v_A = 0 - 100 \text{ km s}^{-1}$;
- gradient of convection velocity: $dv/dz = 0 - 500 \text{ km s}^{-1} \text{ kpc}^{-1}$;
- ISRF model factors (for optical and infrared emission): 0.5 – 1.5;
- B -field parameters: $5 \leq r_c \leq 10 \text{ kpc}$, $1 \leq z_c \leq 2 \text{ kpc}$, and $5.8 \leq B(r=0, z=0) \leq 117 \mu\text{G}$.

It is evident that some (and in fact many) of our extreme models would be completely ruled out by CR data and large scale diffuse gamma-ray data (or even microwave data), if those options would describe the general Galactic properties. We include them with the attitude of testing whether the GCE properties are significantly affected by *extreme* Galactic diffuse model assumptions.

Limitations of our approach. When constructing the 60 GDE models for the estimate of theoretical model uncertainties, we deliberately made a few simplifying assumptions that we will summarize in the following. This will be a useful starting point for future attempts to explain the GCE in terms of standard astrophysical processes. However, the possible impact of those limitations will be partially bracketed by the study of empirical model uncertainties along the Galactic disk that we will present in section 4.2.

Galprop in its standard implementation solves the propagation equation on a two dimensional spatial grid (assuming cylindrical symmetry), which is prohibitive to the modeling of structures like the spiral arms and their impact on the source distribution and CR propagation. Any radial (and in the last two cases also longitudinal) dependence in the description of convection, re-acceleration or diffusion is absent from our GDE models. Diffusion is taken to be isotropic which can only be a rough approximation given the fact that there are large scale magnetic fields in our Galaxy.¹⁴ We summarize the main limitations as follows:

¹⁴An example of a modification of the **Galprop** code to account for inhomogeneous and anisotropic diffusion of CRs due to the presence of large scale ordered magnetic fields can be seen in ref. [104]. The anisotropic diffusion of CRs strongly depends on the assumptions made about the ordered and turbulent components of the Galactic magnetic field. Without including rotation measures and also microwave data to probe the synchrotron total and polarized intensity, we can not constrain those B -field components just from gamma-ray observations. We let such questions for future work.

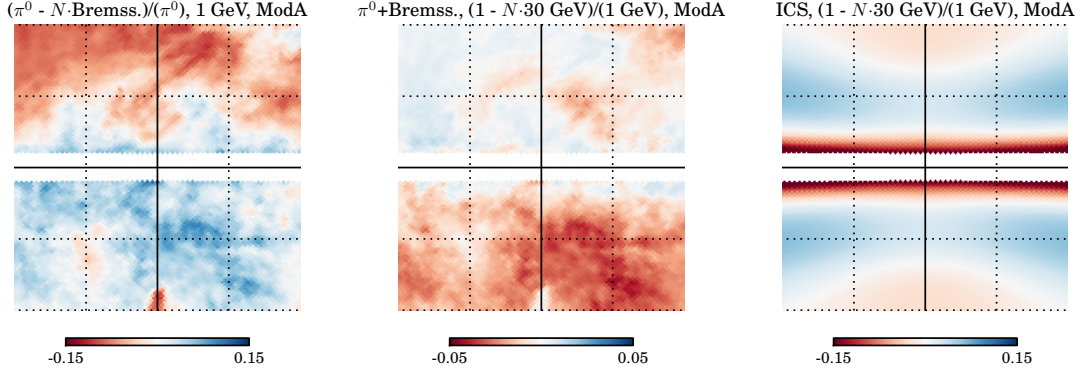


Figure 3. Variations in the template morphologies within our baseline ROI, eq. (2.1). *Left panel:* Ratio of the π^0 map - $N \cdot \text{Bremss}$ map over the π^0 map at 1 GeV for model A. The factor N is fitted to minimize the sum of absolute residuals (we find $N = 1.25$). The relative residuals exceed 5% (10%) in 30% (0.36%) of the pixels. The differential ratio map in combination with the fact that at 1 GeV the two diffuse components are comparable makes it necessary to model the π^0 and bremsstrahlung emissions independently. *Central panel:* Ratio of the $\pi^0 + \text{Bremss}$ map at 1 GeV - $N \cdot (\pi^0 + \text{Bremss}$ map) at 30 GeV over the $\pi^0 + \text{Bremss}$ map at 1 GeV. The relative residuals never exceed a few %. Thus the $\pi^0 + \text{Bremss}$ map is morphologically the same in the energy range of interest and within the window of interest (at the % level accuracy). *Right panel:* Ratio of the ICS map at 1 GeV - $N \cdot \text{ICS}$ map at 30 GeV over the ICS map at 1 GeV. The relative residuals exceed 5% (10%) close to the disk, in about 18% (5.6%) of the pixels. Thus there is an energy dependence of the ICS morphology that can lead to over/under subtracting the ICS emission at different energies if not taken into account.

- assumption of homogeneity and isotropy of CR diffusion, eq. (3.1);
- assumption of homogeneity of CR re-acceleration, described through a scalar quantity, eq. (3.2);
- lack of radial dependence of CR convection;
- assumption of radial symmetry of CR source distribution in the Galactic disk, not fully accounting for the spiral arms;
- assuming a steady state solution for the CRs, excluding transient phenomena;
- same spatial distribution of hadronic and leptonic CR sources;
- lack of a physical model for the *Fermi* bubbles.

All these limitations will become important for future refined analyses of the GCE, but are beyond the scope of the present work.

3.3 Discussion about the template approach

Before presenting our main results, we will illustrate and quantify the limitations of the monolithic energy-independent templates for the individual GDE components that were used in previous template-regression analyses. We will also show the impact of variations of the astrophysical conditions (the relevant reference models are summarized in table 2).

Typically template analyses model both the π^0 and the bremsstrahlung emission with a single template assuming that their morphological differences are not significant. In figure 3

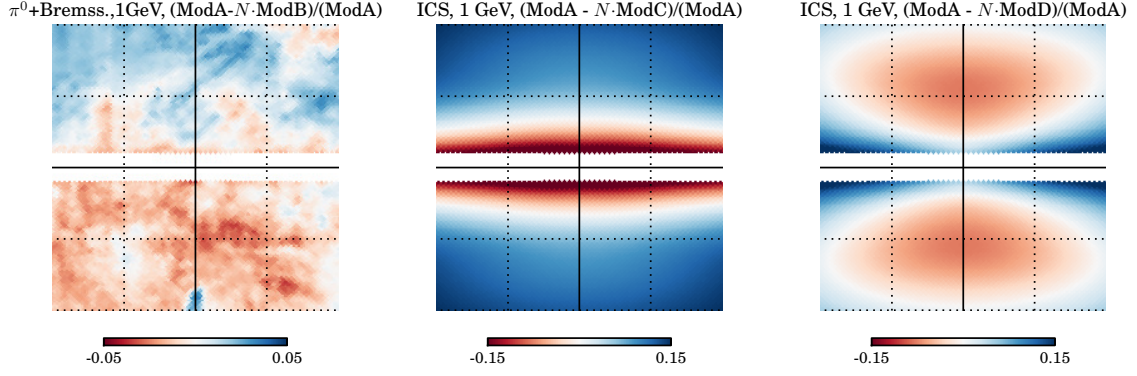


Figure 4. We show in the *left panel* the impact of faster CR diffusion on the π^0 +Bremss map at 1 GeV. The differential ratio map does not exceed the few % level after including a normalization freedom on the combined π^0 +Bremss map. In the *central* and *right panels* we show the impact of different Galactic magnetic field and ISRF conditions on the ICS map. The differential ratio maps at 1 GeV exceed the 5%(10%) level in 79%(47%) of the pixels when comparing model A and C, and 32%(4.4%) of the pixels when comparing models A and D. Disk-like, spherical and bubble-like morphologies can emerge in the differential ratio map, making it necessary to track down the exact physical assumptions towards the GC.

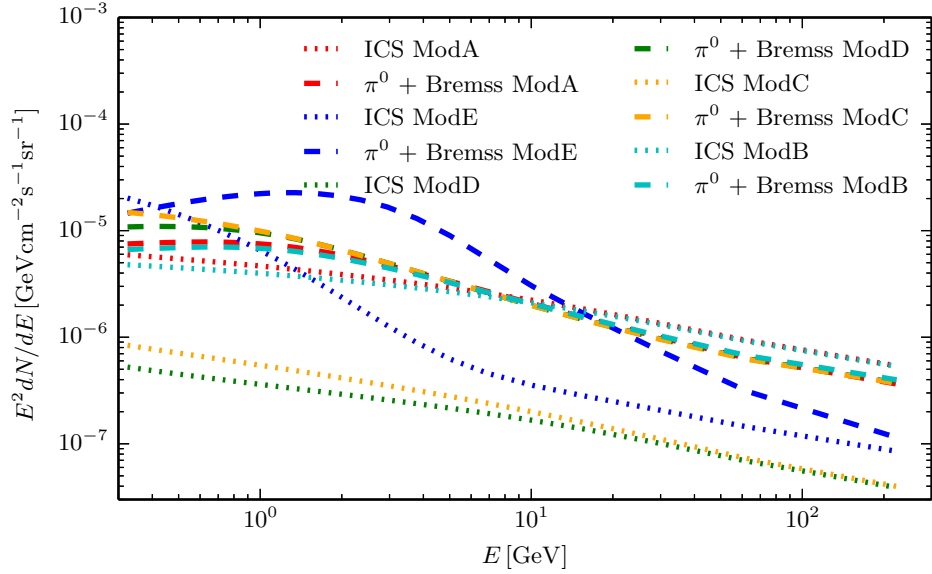


Figure 5. Illustration of the predicted emission for the GDE components π^0 +Bremss (dashed lines) and ICS (dotted lines) from five different models averaged over our baseline ROI.

left, we show that such an assumption has limitations. We take the π^0 and the bremsstrahlung maps at 1 GeV from the predictions of model A, and fit the bremsstrahlung map to the π^0 one within the shown region by minimizing the residual template $|\pi^0 - N \cdot \text{Bremss}|$ (summing over all pixels). These two diffuse emission maps have generically a similar averaged brightness at 1 GeV in that region of the sky (indeed, we find in the specific case $N = 1.25$ from the fit). We then plot the ratio of the $(\pi^0 - N \cdot \text{Bremss})/\pi^0$ maps at 1 GeV. As can be seen, in

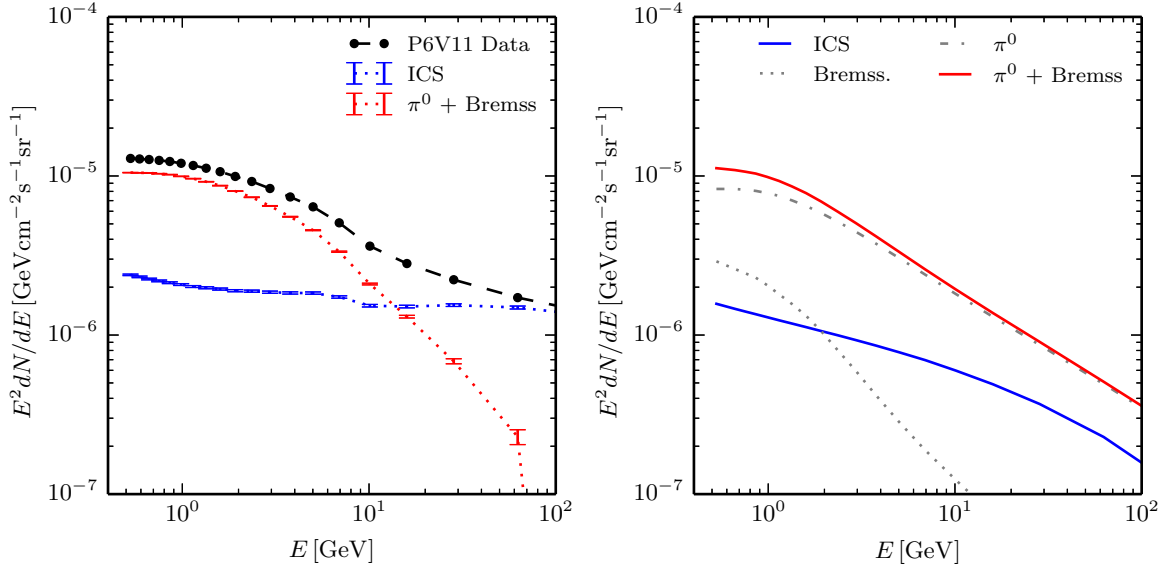


Figure 6. *Left panel:* Decomposition of the P6V11 background model into its contributions from ICS and π^0 +Bremss. The plot was generated by fitting simultaneously the ICS and π^0 +Bremss components of the model P to P6V11 (see text for details). It does not vary much when other diffuse models are used instead. The extremely hard ICS emission at energies > 10 GeV is an *intrinsic* property of the P6V11, which affects any analysis that employs it as GDE template. *Right panel:* For comparison we show the actual spectra predicted by model P for ICS, π^0 and bremsstrahlung emission. Fluxes are displayed in the $40^\circ \times 40^\circ$ ROI, $|b| > 2^\circ$.

30% of the ROI, the pixels deviate from zero by more than 5%. Thus the disagreement between the π^0 and the bremsstrahlung emission morphologies at 1 GeV can easily exceed 5% toward the inner Galaxy.¹⁵ This makes necessary to model the π^0 and the bremsstrahlung emissions independently. Therefore, for each considered GDE model, we build separately π^0 and the bremsstrahlung emission templates. However, as mentioned above, due to the large degeneracies between both components we tie them together to a single π^0 +Bremss template and rescale them simultaneously in our template fit.

Given that the bremsstrahlung emission has generically a softer spectrum than the π^0 , one can understand that the π^0 +Bremss template will change with energy. We show the impact of that in figure 3 middle plot, where we compare the π^0 +Bremss map at 1 GeV with the one at 30 GeV by producing the $(\pi^0$ +Bremss(1GeV) - $N \cdot \pi^0$ +Bremss(30GeV))/ π^0 +Bremss(1GeV) map. The change in the morphology is very smooth and at the few % level. For consistency we include the energy dependence of the individual and the combined emission maps. However, the ICS template does change significantly faster with energy from 1 to 30 GeV (see right panel of figure 3). This is related to the fact that CR electrons are solely responsible of the ICS emission, losing their energy much faster than the CR protons responsible for the π^0 emission. In about 18%(5.6%) of the pixels in the ROI shown we find relative absolute residuals above 5% (10%). Thus there is a sizeable energy dependence of the ICS morphology that can lead to over/under subtracting the ICS emission at different

¹⁵While both the π^0 and bremsstrahlung emission maps correlate with the same gasses, the fact that CR electrons lose their energy much faster than CR protons as they propagate away from the sources makes the bremsstrahlung maps brighter towards the disk at the GeV energies.

energies if not taken into account.

As discussed above, in the present work we are interested in *extremal* templates for the GDE emission, because we want to bracket the uncertainties in extracting properties of the GCE. Additionally, as stated earlier, the physical conditions in the inner Galaxy can be quite different from what they are locally, and we have fewer data to probe them than we do to probe the local or the large scale averaged conditions.

In figure 4 left we compare the π^0 +Bremss maps from models A and B. Their main difference is that model B assumes significantly faster diffusion of CRs (factor of 5 in the diffusion coefficient, see appendix A). The ratio of (Mod A - N ·Mod B)/Mod A at 1 GeV remains below 5% (in absolute value) in all pixels, which shows that after allowing for a free template normalization, this effect remains rather small.

In the case of the ICS templates (shown in the central and right panels of figure 4) the assumptions on the physical conditions, in particular the B -field and the ISRF distributions, can have a size-able impact. We find, again at 1 GeV, absolute residuals in the differential ratio maps (Mod A - N ·Mod C)/Mod A and (Mod A - N ·Mod D)/Mod A that exceed 5% (10%) in 79%(47%) and 32%(4.4%) of the pixels. This can be rather relevant for the GCE extraction, since the ICS component is the one that is closest in morphology to the adopted GCE template. In fact, in these differential ratio maps, disk-like, spherical and bubble-like morphologies can potentially emerge, suggesting that the precise modeling of ICS emission is of high importance for extracting information about the GCE.

Besides the morphology, also the spectral energy distribution of the different components varies significantly from one model to another. To illustrate this point, we show in figure 5 the energy spectra of the combined π^0 +Bremss component and the ICS component for five different GDE models, averaged over our baseline ROI, eq. (2.1). Models B (E) adopts a significantly faster (slower) CRs diffusion, while models C and D refer to different assumptions on the ISRF and the B -field distribution in the inner Galaxy. As can be seen in figure 5, these models predict very different π^0 , bremsstrahlung and ICS spectra. However, the details of the spectra are not of relevance for the final results of this work, since we allow a bin-by-bin refitting of the normalization of the individual components, which, after the fit, leads to only small variations in the overall flux of the template components. Nevertheless, differences in the spectra are relevant for the self-consistency check.

A simple model for the GDE that has been widely used in the literature is the P6V11 model by the LAT Collaboration. This model was developed for background subtraction in the study of point sources, and introduces systematics into any analysis of the gamma-ray diffuse emission that are basically unknown.

Since the P6V11 Galactic diffuse model has just one free parameter (its total normalization), the relative contributions from ICS, π^0 and bremsstrahlung are fixed. We show a *decomposition* of this model into its main components (π^0 +Bremss and ICS) in figure 6 (left panel). To obtain this plot, we perform a full-sky ($|b| > 2^\circ$) fit of the π^0 +Bremss and ICS components of the model P to the P6V11 model. The expected fluxes from the model in the region of interest are shown in the right panel of figure 6. We checked that our results do not change qualitatively when using the π^0 +Bremss and ICS of other diffuse models, and can hence be considered as robust. The plot shows that the P6V11 features an extremely hard ICS component at energies above 10 GeV, which in a template regression analysis can easily

lead to over-subtraction of other diffuse components in the data.¹⁶ It is easily conceivable that this property of the P6V11 contributes to the softening of the GCE emission above 10 GeV that was found e.g. in refs. [55, 62], but is absent in our analysis.

The reason for this hard ICS component at high energies is not obvious. It could potentially be related to neglecting the contribution from the *Fermi* bubbles during its construction, which, in turn, could have been partially absorbed into the ICS component. Whatever the exact reason for this hard ICS spectrum is, it shows that the P6V11 is not self-consistent in the above sense.

4 Non-parametric analysis of the Galactic center excess

In this section we present our main results from the template-based multi-linear regression analysis, and describe in detail how we estimate the various model systematics for the GCE. Parametric fits to the spectrum and morphology of the GCE are kept for section 5.

In subsection 4.1 we discuss the theoretical model systematics of the GCE spectrum that we infer from a set of 60 GDE models. In subsection 4.2 we estimate and discuss the empirical model systematics by analyzing *Fermi*-LAT data in 22 test regions along the Galactic disk. In subsection 4.3 we finally present a study of the GCE in different segments of our baseline ROI, which provides a handle for a later study of the morphology and extension of the GCE.

4.1 Theoretical model systematics

In figure 7 we show the main result of this subsection: the energy spectrum of the GCE that we find when adopting *any* of our GDE models. The individual diffuse components that contribute to the fit were discussed above and are summarized in table 1. They include a set of 60 GDE models that span a rather large range of physical conditions. As described above, the normalization of each emission component is left free to float in each energy bin, but additional external constraints are applied to the IGRB and *Fermi* bubbles templates.

We use our set of 60 GDE models to bracket the theoretical uncertainties that affect the extraction of the GCE. It is remarkable that the GCE emission spectrum is rather stable. At energies above 1 GeV, the overall flux varies by less than a factor of 2–3, and features in all cases a pronounced peak at energies around 1–3 GeV. At higher energies, the spectrum appears to be well described by a power-law with a spectral slope of ~ -2.7 (but see discussion in section 5). At lower energies we observe a pronounced rise in the energy spectrum with a spectral index that is significantly harder than ~ 2 for all of the GDE models, though the exact form of the spectrum is rather dependent on the adopted GDE model.

In figure 7, we also highlight the spectra that we obtain for the GDE model F, which yields formally the best fit, and for the GDE model A, which we used above in section 3 as reference model (cf. parameters in table 5). These spectra are shown together with their statistical errors, which are – except at the highest energies – smaller than the width of the theoretical model systematics band.

In figure 8, we show the energy spectra of the different diffuse and PSC components for model A and model F, averaged over the baseline ROI and compared to the data. Since the normalization of all components is left free to float, independently in each energy bin, it is not guaranteed that the individual measured spectra actually correspond to a physical

¹⁶This peculiarity of the P6V11 is also contained in the *Fermi* documentation at http://fermi.gsfc.nasa.gov/ssc/data/P6V11/access/lat/ring_for_FSSC_final4.pdf.

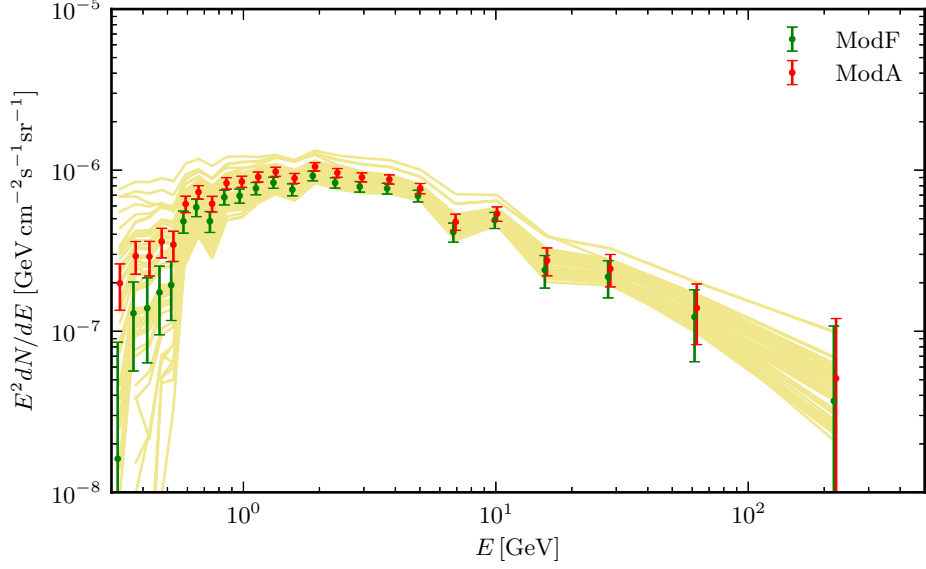


Figure 7. Plain GCE energy spectrum as extracted from our baseline ROI, assuming a generalized NFW profile with an inner slope $\gamma = 1.2$, for all of the 60 GDE models (*yellow lines*). We highlight the model that provides the best overall fit to the data (model F, *green points*) and our reference model from the discussion in section 3 (model A, *red points*), together with $\pm 1\sigma$ statistical errors. For all 60 GDE models, we find a pronounced excess that peaks at around 1–3 GeV, and follows a falling power-law at higher energies.

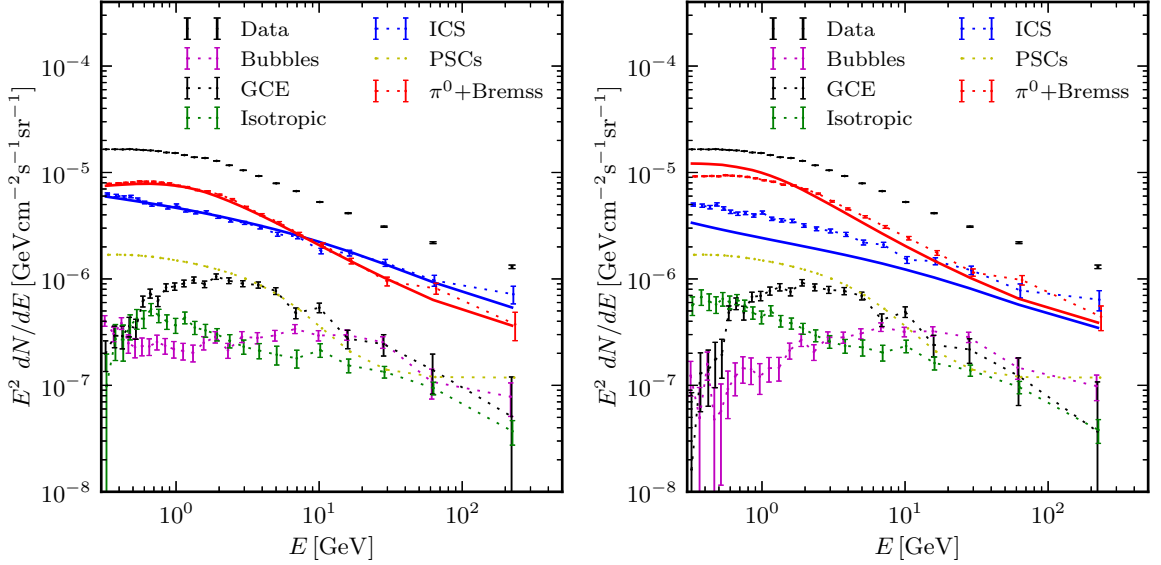


Figure 8. Energy spectra of different components (*dotted lines*) from a template fit to the data (*black points*), compared to the predicted GDE model fluxes (*solid lines*). The reference model A is shown in the *left panel*, while the GDE model that provides the best-fit to the data, model F, is shown in the *right panel*.

model. However, as already discussed above, we find that for model A (which was specifically constructed for that purpose) the *predicted* and the *measured* energy spectra of the GDE components agree very well at the level of 5–10%.¹⁷ This serves as a proof-of-principle that the results obtained from the template fit can actually correspond to a physical GDE model. For model F, which yields the best-fit, the fitted GDE fluxes deviate somewhat from the predicted ones, but are still close to what we found for model A. Below, we will use model A and F as reference scenarios.¹⁸

In figure 9, we show the latitude (top left panel) and longitude (remaining panels) profiles of the individual diffuse and PSC components, and their sum compared to the actually measured fluxes for model A. Data and model are in general in very good agreement. We remind that, although the contributions from point sources are shown in these plots for completeness, the corresponding regions are actually masked during the fit. However, we find that even in the re-added masked regions the agreement between model and data is reasonably good, except for regions that contain very bright sources.

One of the most striking, but also most critical aspect of the GCE spectrum is the steep rise at sub-GeV energies. It is instructive to see how the predictions at low energies would change *in absence* of such a rise. To this end, we show in the bottom left panel of figure 9 the GCE template and total emission for a GCE spectrum that is extrapolated down from its value at 2 GeV with a spectral slope of -2. In that case, the longitudinal profile of the gamma-ray emission would be significantly enhanced close to the GC, which is not observed. Note that we selected for this plot the latitude range at which this effect is best visible by eye. In the right bottom panel of figure 9, we show for completeness the flux that would be predicted in absence of a GCE emission at energies around 3 GeV.

In figure 10, we show exemplary count and residual maps for model A. The left panel of each row shows a map of photon counts in our baseline ROI adopting also the PSC mask as described in section 2.2. The other panels show the total residuals (data - model counts) when the emission associated with all templates is subtracted from data (central panel) or when all templates but the GCE template are subtracted (right panel). The comparison of the residuals with and without GCE template gives a rough but useful idea about the intensity of the emission associated with the GCE template and its spatial extension.

In general, we find correlated residuals that are well above the level expected from Poisson noise: about 10% at $E < 1$ GeV and about 25% for $E \sim 3$ GeV (including the GCE contribution). The emission associated with the GC excess is, after other components are subtracted, the most pronounced large-scale excess in our ROI (and, as a matter of fact, in the entire Galactic plane with $|\ell| \leq 70^\circ$). However, we will discuss in the next subsection that excesses of similar size are observed in other regions along the Galactic disk, and we will characterize their properties and implications for the interpretation of the GCE.

The residual plots in figure 10 illustrates that it is hard to construct an a priori model of the GDE that is in agreement with the observations at the level of Poisson noise. In fact, for our best-fit GDE model F, the reduced χ^2 in the energy range from 500 MeV to 3.31

¹⁷We checked that this is also true when applying the latitude cut $|b| \geq 5^\circ$ instead and repeating the fits.

¹⁸As can be seen in figure 8, the spectrum of the IGRB (in the left panel) and the *Fermi* bubbles (in the right panel) is sometimes overly suppressed at energies below 1 GeV, which suggests an over-subtraction of the GDE. We checked that this possible over-subtraction has only minor impact on our results and decided to keep these energy ranges in our analysis, see discussion in subsection 4.2.

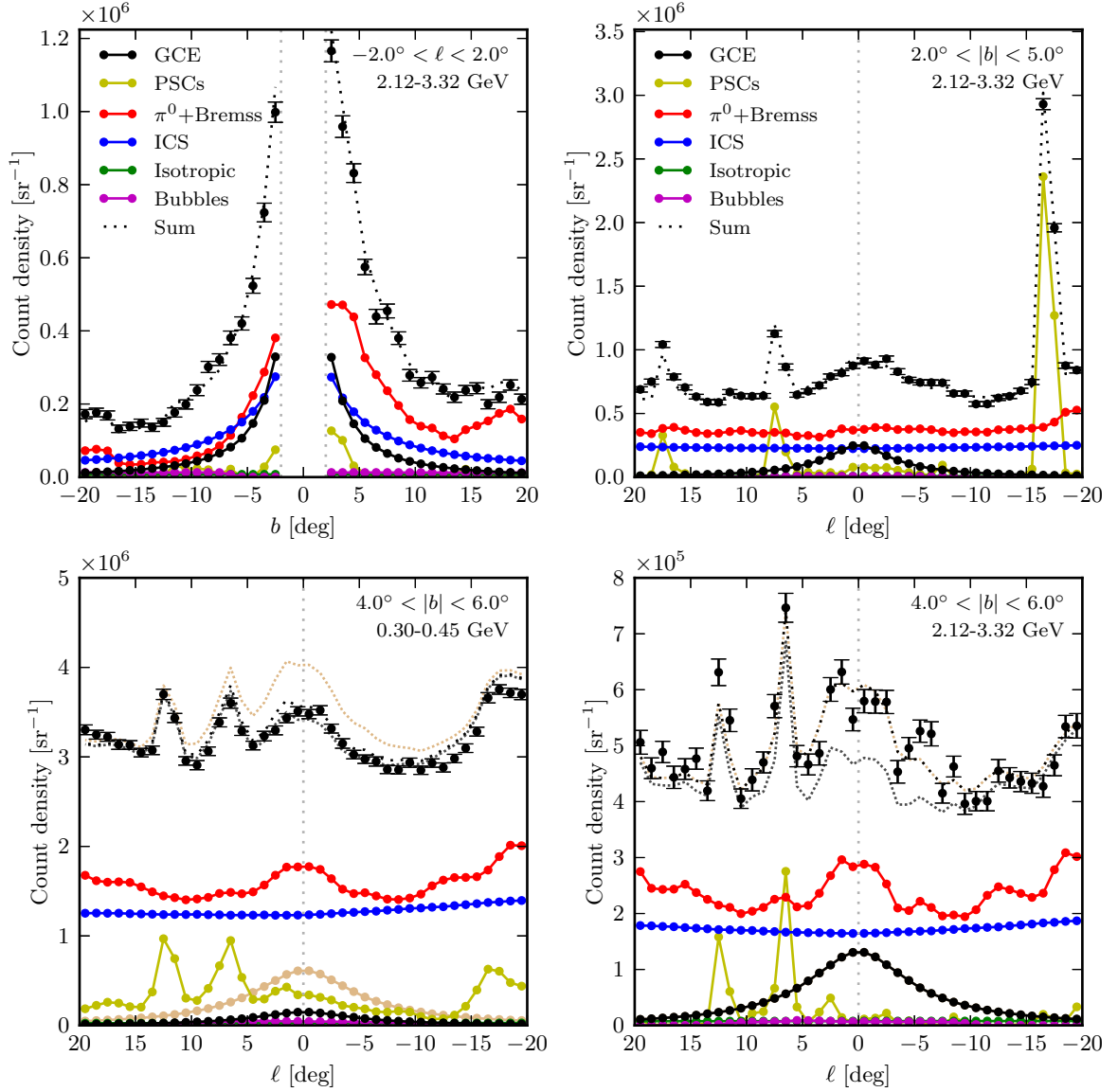


Figure 9. *Top panels:* Latitude (*left*) and longitude (*right*) dependence of the different components in narrow spatial strips, at energies around 3 GeV, for model A. *Bottom panels:* Same as top right panel, but further away from the Galactic disk in the latitude range of $4^\circ < |b| < 6^\circ$, at energies around 400 MeV (*left*) and 3 GeV (*right*). Furthermore, in the *bottom left panel*, the *light pink line* illustrates the situation of a GCE spectrum that is softer than the one that we find in our template fits. For comparison, we show here the case where the GCE component flux would follow a simple power-law with spectral index 2.0 at energies below 2 GeV, keeping the normalization fixed to the one measured at 2 GeV. The summed spectrum clearly overshoots the data in the inner few degrees. Finally, in the *bottom right panel*, the *gray densely dotted line* shows in addition the sum of fluxes when the GCE component is neglected.

GeV¹⁹ is around $\chi^2/\text{dof} \simeq 295000/267000 \simeq 1.10$. Although this value is close to one, thanks to the large number of degrees of freedom the corresponding p -value is utterly small and

¹⁹At higher energies the low number of photons prohibits a simple goodness-of-fit analysis.

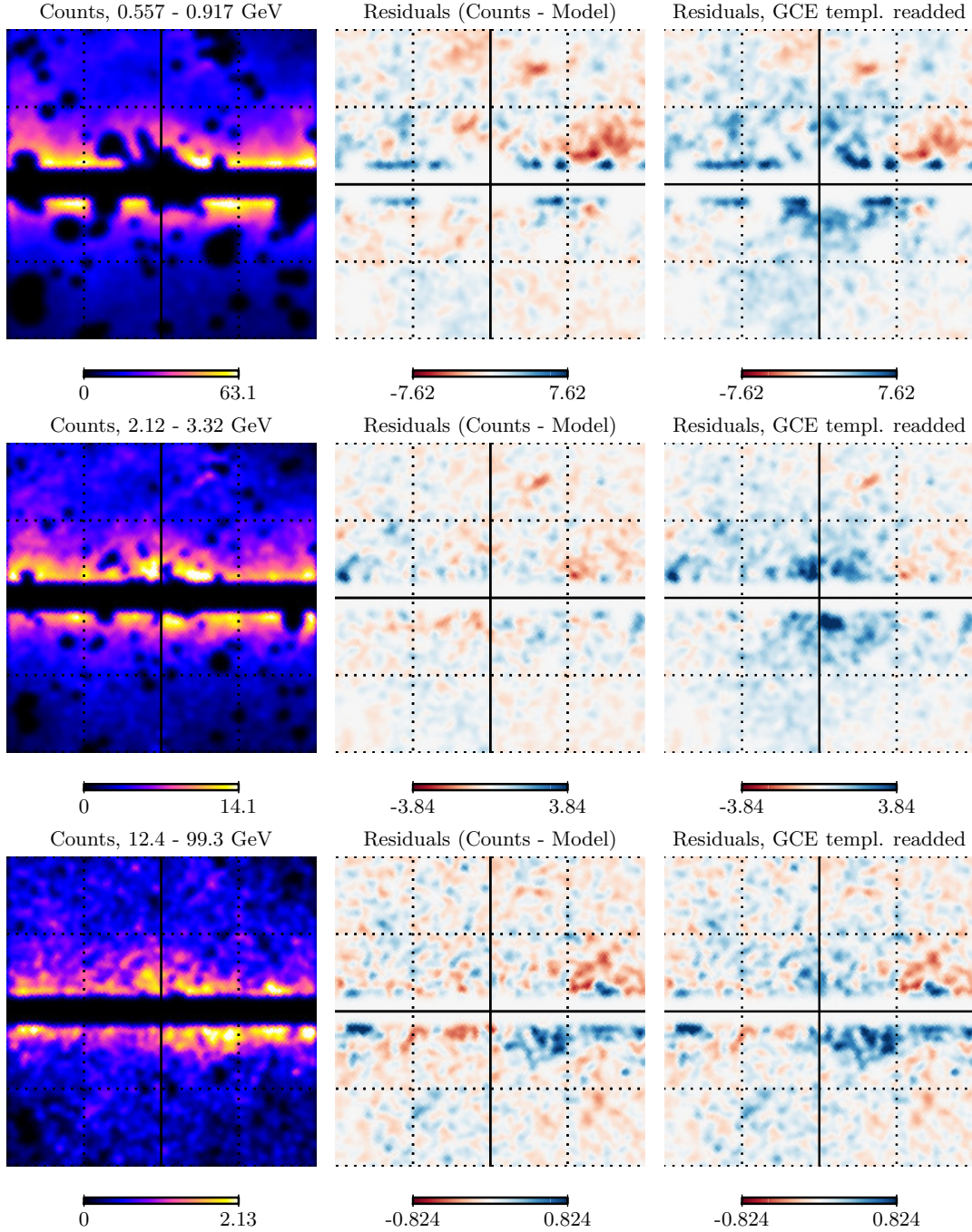


Figure 10. *Left panels:* Count maps at various energies (from *top* to *bottom*), with the disk cut $|b| > 2^\circ$ and PSC mask applied. *Central panels:* Residuals after subtracting our self-consistent GDE model A. *Right panels:* Residuals after subtracting our self-consistent GDE model, but re-adding the GCE template associated to the model. A Gaussian smoothing with $\sigma = 0.4^\circ$ is applied to all plots.

around 10^{-300} . Given the high quality and statistics of *Fermi*-LAT data, and the still rather rudimentary treatment of the GDE, this is hardly surprising.

In any case, the comparison of TS values remains an important tool for selecting GDE

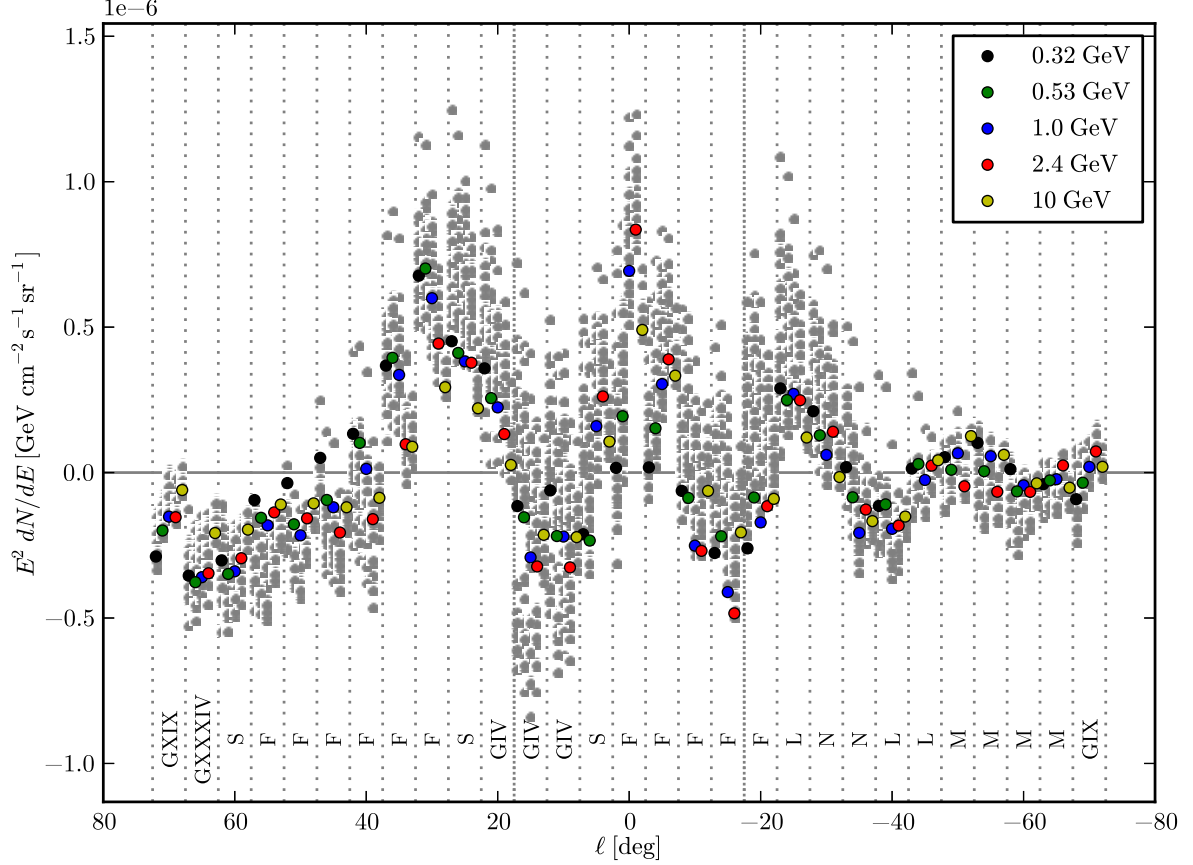


Figure 11. Flux absorbed by the GCE template when moving it, as well as the ROI, along the Galactic disk in steps of $\Delta\ell = \pm 5^\circ$, for five different reference energies. The *colored dots* indicate the flux for the GDE model that gives *locally* the best-fit (these models are listed in the bottom of the plot), whereas the *gray dots* indicate the fluxes for all other models. The excess observed at the GC is – at around 1–3 GeV – clearly the largest in the considered region, although other excesses exist as well (see text for a discussion). Regions with $|\ell| \gtrsim 20^\circ$ (indicated by the *vertical dotted lines*) will be used as test regions for estimates of the empirical model uncertainties of the adopted GDE models.

models that provide gradual improvements when fitting the data. However, the extremely small p -values that one obtains when fitting the data suggest that it is mandatory to study the typical uncertainties of the GDE modeling in light of the data before drawing strong conclusions from purely statistical fits. This is what we will do in the next subsection.

4.2 Empirical model systematics

The modeling of the GDE in the present analysis is entirely based on the numerical code `Galprop`. The agreement between the GDE modeling and actual data in the inner Galaxy is quite satisfactory, with typical residuals that are significantly smaller than the GCE (see figures 9 and 10). However, in order to increase the confidence in these results and to study the robustness of the inferred GCE spectrum, we will estimate typical residuals above the `Galprop` predicted GDE by analyzing the diffuse emission from the Galactic disk, away from the GC, in a systematic way.

As discussed above, a significant part of observed the gamma-ray emission towards the inner Galaxy is actually produced *locally*, with typical distances of a few kpc along the line-of-sight (cf. figure 2). At first approximation one can hence expect that the accuracy of GDE modeling, at least at the $|b| > 2^\circ$ latitudes we are interested in, is of a similar level along the entire inner part of the Galactic disk, including the region close to the GC. We will here consider variations in the longitude range $|\ell| < 90^\circ$, and use them to estimate the model systematics at the GC.

4.2.1 Analysis of test regions along the Galactic disk

We consider a number of ROIs along the Galactic disk, away from the GC, and measure how much of the observed gamma-ray emission is absorbed in the transposed GCE template centered in that ROI. Namely, we consider gamma-ray data in the region $|\ell| \leq 90^\circ$ and $|b| \leq 20^\circ$, in 29 overlapping ROIs defined by $-20^\circ + k \cdot 5^\circ \leq \ell \leq 20^\circ + k \cdot 5^\circ$ and $2^\circ \leq |b| \leq 20^\circ$, with $k = -14, -13, \dots, 14$. The GCE emission template moves along and is centered at $\ell = k \cdot 5^\circ$. For all of our 60 GDE models and all of the ROIs we perform a template analysis as above for the GC.

The excess emission that we find along the Galactic disk is summarized in figure 11 in a rather compact way. For all 60 GDE models we show as gray dots the flux that is absorbed by the (transposed) GCE template, as function of the template center in longitude steps of $\Delta\ell = \pm 5^\circ$, for five different reference energy bins centered at 0.32, 0.53, 1.0, 2.4, and 10 GeV. For each longitude step, we determine the *locally* best-fit-model in that ROI. We then highlight by colored points the fluxes measured for that model at each of the five different energies. This allows to read off a rudimentary estimate of the excess spectrum in each region of the Galactic disk.

As can be seen in figure 11, we clearly reproduce the pronounced excess at the GC ($\ell = 0^\circ$), with a peak in the spectrum at energies around 2.4 GeV (see the trend of the colored points at $\ell = 0^\circ$). At these energies, the GC excess is the most pronounced excess in the entire test region. However, at Galactic longitudes around $\ell \sim \pm 25^\circ$, we observe residuals with almost identical size. Further away from the GC, at $|\ell| \geq 40^\circ$, residuals are mostly consistent with zero, though sometimes biased towards negative values.

The excesses along the Galactic disk might be on first sight discouraging, since they show that uncertainties of the GDE as we model it in the present analysis are almost of the same magnitude as the GCE itself. This brings up the question whether any reliable conclusions about the morphology, spectrum and distinctiveness of the GCE can be drawn at all.

From figure 11 we find a number of differences between the GCE and the excess emission away from the GC at $\ell \sim \pm 25^\circ$. The most notable one is that the emission at GC has a different spectrum, with a peak at energies around 2 GeV, which is not present in any of the regions away from the GC. Furthermore, the GCE is strongly peaked at the GC, and falls off rapidly as function of longitude, whereas the excesses away from the GC have a smoother dependence on ℓ . Already this suggests that the GCE and excesses away from the GC are of different physical origin.

At least one of the excesses away from the GC, at $\ell \sim 25^\circ$, appears to be associated with a known structure, the Aquila Rift region, which is a molecular cloud complex that is well identified in CO [119], and has an enhanced star formation rate [120]. With a distance from the Sun of a few hundred pc [121], it is the closest molecular complex towards the inner

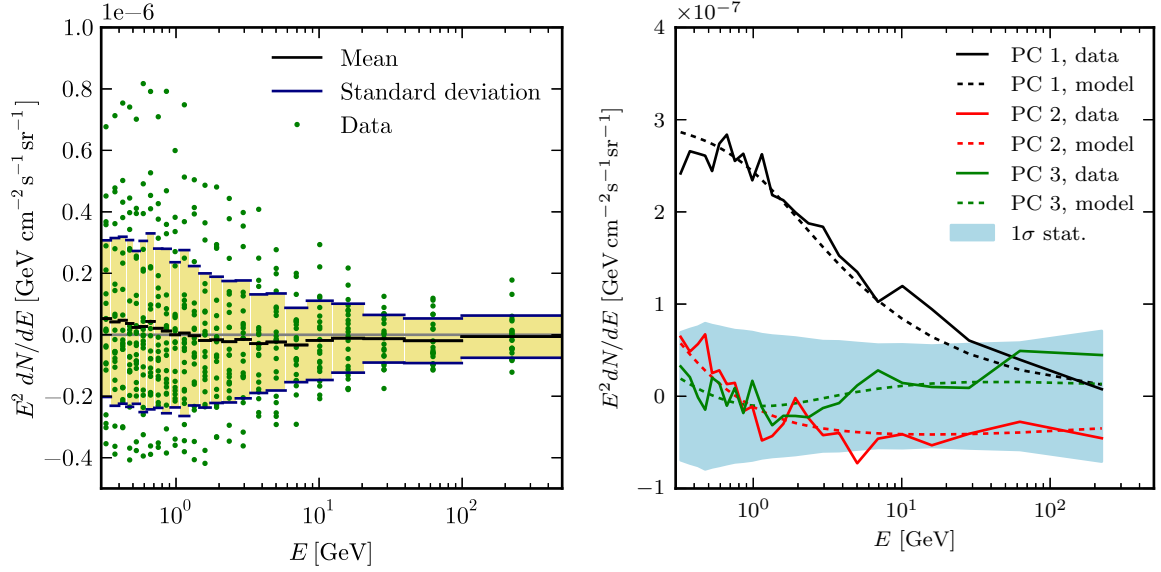


Figure 12. *Left panel:* Residuals absorbed by the transposed GCE template in 22 test regions along the Galactic disk (*green points*), as shown in figure 11 by the colored dots; the *yellow boxes* indicate the mean and standard deviation. *Right panel:* Decomposition of the covariance matrix of the residuals in principal components. We only show the three components with the largest standard deviation (*solid lines*), and compare them to the statistical errors from the GCE fit at the GC (*blue area*). The *dashed lines* show model predictions from a four parameter analytical model. It provides a good fit and traces the observed variations back to uncertainties in the normalization and slope of the π^0 and ICS components (see appendix. C.1 for details about the model).

Galactic region. Indeed, the observed excess spectrum appears to be a featureless power-law with a spectral index of very roughly 2.3, compatible with the typical expectations for star forming regions [32]. More generally, longitudes around $\ell \sim \pm 25^\circ$ (with a projected distance of at least 3.6 kpc from the GC) coincide with the molecular ring with a high projected star formation along the line-of-sight [122].

We tried to account for the observed excesses by allowing additional variations in the HI and H2 maps or subsets thereof, however without much success. The *Fermi* team encountered similar problems and used ad hoc templates to account for the excess emission in models for the GDE.²⁰ In the present work, we will simply accept these excesses along the Galactic disk as model uncertainties of state-of-the-art GDE models, and incorporate them in our analysis below.

4.2.2 The covariance matrix of empirical model systematics

We will make use of the observed residuals in figure 11 as an estimate for empirical model systematics along the Galactic disk. To this end, we show in the left panel of figure 12 the flux that is absorbed by the transposed GCE templates in different energy bins. Each dot represents one of the 22 test ROIs in the longitude range $20^\circ \leq |\ell| \leq 70^\circ$. We also indicate the mean values, which remain close to zero, and the standard deviations.

²⁰See P7V6 discussion, http://fermi.gsfc.nasa.gov/ssc/data/access/lat/Model_details/Pass7_galactic.html.

The observed variations along the disk are correlated in energy. We quantify this by analyzing the covariance matrix of the fluctuations, which is given by

$$\Sigma_{ij, \text{mod}} = \left\langle \frac{dN}{dE_i} \frac{dN}{dE_j} \right\rangle - \left\langle \frac{dN}{dE_i} \right\rangle \left\langle \frac{dN}{dE_j} \right\rangle, \quad (4.1)$$

where the average runs over the 22 test ROIs, and dN/dE_i denotes the GCE-like residual flux in energy bin i as shown in the left panel of figure 12.

We analyse the properties of this covariance matrix in terms of its principal components. These are simply the eigenvectors of this matrix, normalized to the corresponding variance. The three principal components with the largest standard deviation are shown in figure 12, compared with the $\pm 1\sigma$ statistical error of the GCE at the GC. We find that only the first principal component is at almost all energies significantly larger than the statistical errors. It follows very roughly a power-law with a spectra slope of 2.2, which is reminiscent of ICS emission.

The origin of the observed empirical model systematics can be understood in terms of a simple analytical model that we discuss in appendix C.1. It takes as four parameters only the uncertainties in the normalization and slope of the π^0 +Bremss and ICS components. Fitting these four parameters to the three largest principal components of the covariance matrix gives rise to a *modeled* covariance matrix with principal components as shown by the dashed lines in the right panel of figure 12. The agreement is rather satisfactory, except at the very lowest energies below 600 MeV where the modeled first principal component overshoots slightly the observed one. We hence conclude that the empirically derived model systematics can be understood in terms of variations in the normalization and spectral slopes of the primary diffuse background components.

Below, we will use the empirical covariance matrix when performing fits to the GCE spectrum instead of the analytical model. However, in order to avoid a double-counting of statistical errors, we will truncate the principal components that enter the empirical covariance matrix and restrict them to the first three. We will refer to this truncated matrix as $\Sigma_{ij, \text{mod}}^{\text{trunc}}$.

4.2.3 Other systematics and the GCE spectrum

Before showing the GCE spectrum with empirical model uncertainties, we summarize further systematics that enter our analysis in figure 13. Namely, we display the impact on the flux absorbed in the GCE template when *a)* decreasing the width of the PSF by a reference factor of 0.8, *b)* including PSF smoothing also for the GCE template, *c)* changing the definition of the PSC mask by varying f_{mask} as indicated or using model E instead of model P for the PSC mask definition, *d)* fixing the flux of the IGRB and the *Fermi* bubbles to their external constraints rather than leaving them free to vary, and *e)* using a different GDE model to define the PSC mask. At energies above 1 GeV, all of these variations are well below the statistical error and negligible. However, we take the variations below 1 GeV into account by modeling them as $dN/dE^{\text{res}} = 6 \times 10^{-8} \text{ GeV}^{-1} \text{ cm}^{-2} \text{ s}^{-1} \text{ sr}^{-1} (\text{E}/1 \text{ GeV})^{-3}$. We include this uncertainty in the final fit *twice*: once as uncorrelated error and once as fully correlated errors with a free normalization. This gives rise to a covariance matrix $\Sigma_{ij, \text{res}} = dN/dE_i^{\text{res}} dN/dE_j^{\text{res}} + \delta_{ij} dN/dE_i^{\text{res}} dN/dE_i^{\text{res}}$.

Finally, figure 14 shows, as one of the main result of this subsection, the spectrum of the GC excess emission for model F (cf. figure 7), together with statistical errors and the

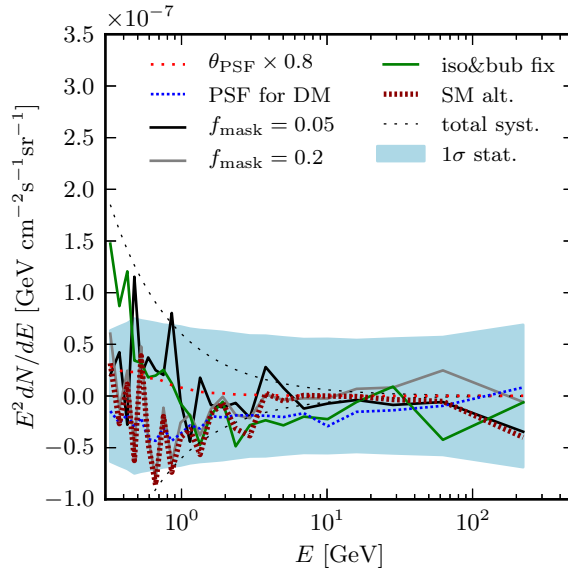


Figure 13. Summary of different analysis systematics. The impact of choices made in the PSC mask definition is shown by the *solid black* and *gray lines* (for variations in f_{mask}), and by the *dotted dark red line* (for adopting an alternative GDE model in the mask definition). We also show the impact of smoothing the GCE template with the *Fermi-LAT PSF* (*blue dotted line*), fixing the isotropic and bubbles normalization to their external constraints (*green solid line*), rescaling the *Fermi-LAT PSF* by a factor close to one (*red dotted line*). The *light blue region* represents the statistical errors. Results are shown for the reference model A, but should be rather similar for other GDE models. The *thin dotted line* shows our estimate for the overall analysis systematics, which at energies below 1 GeV clearly exceed the statistical errors of the GCE. See text for details on the implementation in spectral fits.

(diagonal part of the) empirical model systematics as inferred above (note that we omit the sub-dominant method uncertainties $\Sigma_{ij, \text{res}}$ in this plot). Statistical and systematic errors are shown at $\pm 1\sigma$. For comparison, we overlaid the envelope of the GCE spectra associated with the 60 GDE models as shown of figure 7, to indicate the theoretical model systematics. We find that empirical and theoretical systematics are roughly of the same order in the considered energy range and ROI.

4.3 The morphology from ten sky segments

We will now set the stage for an investigation of the morphology of the GCE in section 5 below. We are interested in studying a) the symmetry of the excess emission around the GC, and, more importantly, b) how far from the disk the GCE extends. To this end, we split the GCE template in ten segments and repeat the analysis of the previous two subsections. Furthermore, we allow additional freedom in the ICS templates, as we explain below. We present additional morphological studies of the GCE, which mostly reconfirm findings from previous works, in appendix B.

We divide the GCE template within our main ROI, see eq. (2.1), into *ten GCE segments* as shown in figure 15 and defined in table 3. Each of the ten segments is zero outside of its boundaries, and equals the standard GCE template (generalized NFW with $\gamma = 1.2$) inside its boundaries. The normalization of each of the ten templates is allowed to float freely in

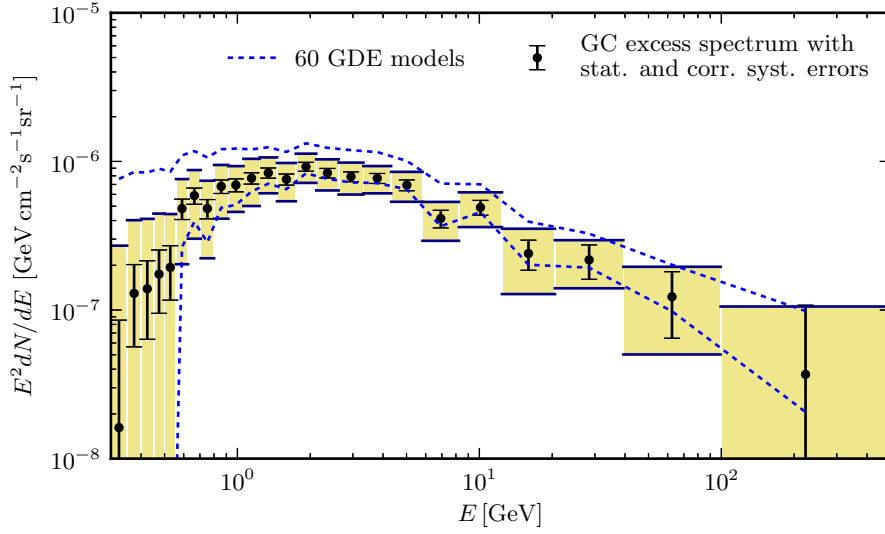


Figure 14. Spectrum of the GCE emission for model F (*black dots*) together with statistical and systematical (*yellow boxes*, cf. figure 12) errors. We also show the envelope of the GCE spectrum for all 60 GDE models (*blue dashed line*, cf. figure 7).

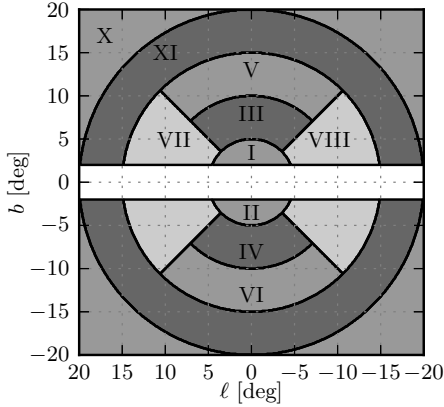


Figure 15. Geometry of the ten GCE segments used in our morphology analysis, see table 3.

#ROI	Definition	Ω_{ROI} [sr]
I, II	$\sqrt{\ell^2 + b^2} < 5^\circ, \pm b > \ell $	6.0×10^{-3}
III, IV	$5^\circ < \sqrt{\ell^2 + b^2} < 10^\circ, \pm b > \ell $	1.78×10^{-2}
V, VI	$10^\circ < \sqrt{\ell^2 + b^2} < 15^\circ, \pm b > \ell $	2.93×10^{-2}
VII, VIII	$5^\circ < \sqrt{\ell^2 + b^2} < 15^\circ, \pm \ell > b $	3.54×10^{-2}
IX	$15^\circ < \sqrt{\ell^2 + b^2} < 20^\circ$	1.51×10^{-1}
X	$20^\circ < \sqrt{\ell^2 + b^2}$	1.01×10^{-1}

Table 3. Definition of the ten GCE segments that are shown in figure 15, as function of Galactic latitude b and longitude ℓ , together with their angular size Ω_{ROI} .

the fit. The definition of the segments aims at studying the symmetries of the GCE around the GC: Allowing regions in the North (I, III, and V) and South (II, IV, and VI) hemisphere, as well as in the West (VII) and East (VIII) ones, to vary independently, we can test the spectrum absorbed by the GCE template in the different regions of the sky. Moreover, with the same segments, we can investigate its extension in latitude.

To facilitate the study of morphological properties of the excess, we furthermore allow additional latitudinal variations in the ICS components of the individual GDE models. We split our ICS component into *nine ICS segments*, corresponding to 9 latitude strips with boundaries at $|b| = 2.0^\circ, 2.6^\circ, 3.3^\circ, 4.3^\circ, 5.6^\circ, 7.2^\circ, 9.3^\circ, 12.0^\circ, 15.5^\circ$ and 20° . We then allow the normalization of the ICS strips to vary independently, though we keep the normalization

of strips that are symmetric under $b \rightarrow -b$ bound to the same value; this gives nine free parameters for the ICS emission.²¹ The advantage of these additional degrees of freedom is that they allow to mitigate the effects of over- or under-subtraction of data at different latitudes. The GCE component has a significant correlation with the ICS emission. An unbiased treatment of the ICS is hence important. Physically, this variability makes sense since it accounts in a simple but efficient way for uncertainties in the CR electron density and the ISRF at different latitudes along the line-of-sight. Practically, it reduces the scatter between the 60 GDE models and removes outliers, without much affecting results for the best-fit models.

With the above setup, namely ten GCE segments and nine ICS templates plus all remaining components from table 1, we analyze the *Fermi*-LAT data within our main ROI as well as the test regions along the Galactic disk for all of our 60 GDE models (for the test regions we actually use only one combined ICS template for efficiency, which might lead to a slight overestimation of the empirical model systematics). In analogy to what we did above, we estimate the variance in each of the ten GCE template segments from fits in ROIs that are centered at $20^\circ \leq |\ell| \leq 70^\circ$ and $b = 0^\circ$.

The results for the extracted GCE template fluxes are shown in figure 16. The error bars correspond to the model that yields the best TS value (which is still model F), but we also indicate the envelope from all models, as well as the model systematics that we found from the Galactic disk analysis (cf. figure 14). In the regions I–IV, the GC excess is clearly visible with a peak at energies around 1–3 GeV, and with a drop at energies above and below. Similar excesses are observed in the other template segments, with spectra that suggest compatibility with what is observed in I–IV. Such a compatibility of spectra of the different segmented templates indicates that there is no clear asymmetry with respect to the GC—neither in the North vs South hemispheres, nor in the West vs East hemispheres. We present a quantitative discussion about the actual extension of the excess to higher latitudes and the compatibility of spectra in the different sky regions in section 5.

We end with a few words about the covariance matrix of empirical model uncertainties that we find for the segmented GCE template. We analyze the principal components of this matrix for each of the ten segments independently. In general, we find that the observed fluctuations are significantly larger than the ones that would be predicted from the analytical model in appendix C.1 when using the same model parameters that we found in the previous subsection for the single GCE template. This suggests that there are, not surprisingly, variations in the backgrounds of the individual GCE segments that average out when considering the single GCE template. We take these additional variations automatically into account in the subsequent analysis by making use of the (truncated) covariance matrix in our spectral and morphological fits. However, we will neglect here possible segment-to-segment correlations.

5 Parametric fits to the Galactic center excess

Equipped with information about the GCE spectrum and morphology, and with estimates for the theoretical and empirical model uncertainties, we perform in this section a number of

²¹We note that the spectral shape of the GC excess, as well as the envelope discussed in section 4.1 and shown in figure 7, remains basically the same when applying this additional degrees of freedom in these fits. See further discussion in appendix B.

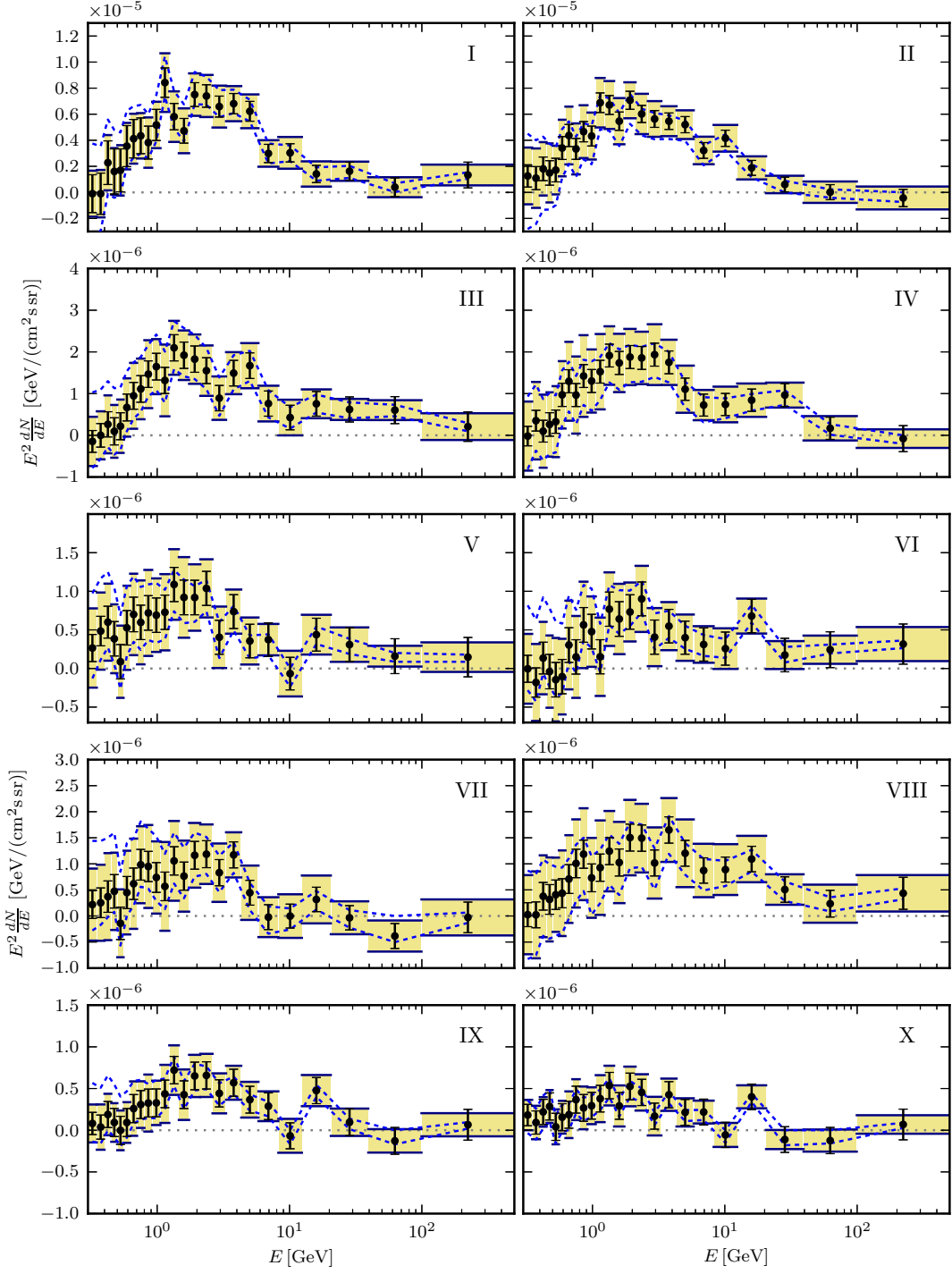


Figure 16. Same as figure 14, but from a fit with the segmented GCE template as illustrated in figure 15. We show results for GDE model F (*black dots*), as well as the envelope for all 60 GDE models (*blue dotted lines*) and the systematic errors that we derived from fits in 22 test regions along the Galactic disk (*yellow boxes*, in analogy to figure 12). See figure 28 below for the spectra of all components.

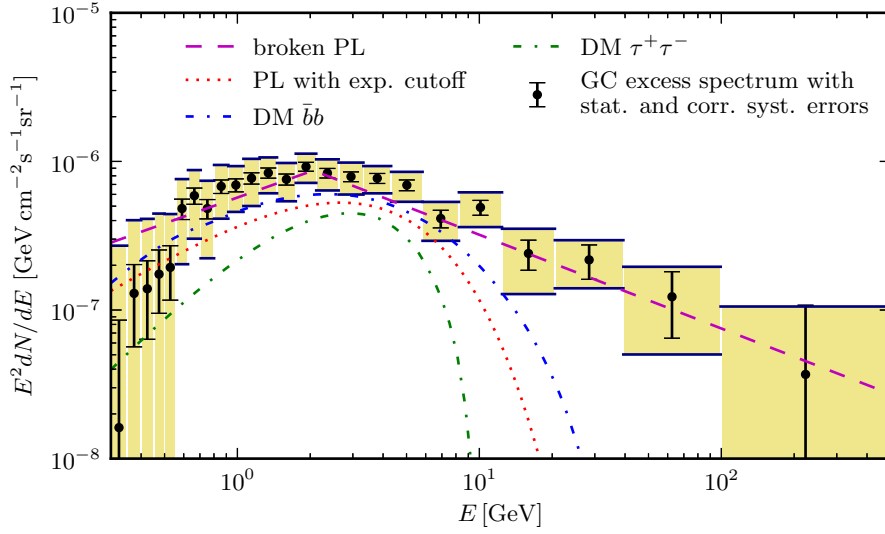


Figure 17. Spectrum of the GCE emission, together with statistical and systematical errors, for model F (cf. figure 14). We show fits to the GCE with various spectral models. We emphasize that the shown systematic errors are *correlated*, and that the spectral models actually *do* provide a good fit to the data in most cases. We show the best-fit model parameters, along with indicators for the fit quality, in table 4 (cf. figures 18 and 20). See text for details on the fitting procedure.

parametric fits to the data.

In the previous section, we found that theoretical and empirical model uncertainties affect the GCE spectrum at a similar level (see figure 14). However, theoretical model uncertainties in the way we discussed them here are difficult to interpret in a purely statistical sense, since the TS values that we find for fits with our 60 GDE models differ typically by $> \mathcal{O}(100)$ values (see appendix A), and even our best-fit model for the GDE gives formally a poor fit to the data. This is a generic problem of modeling the GDE [58], as we discussed at the end of section 4.1. On the other hand, the empirical model uncertainties are simple to interpret statistically and give by construction a realistic account for typical systematics of state-of-the-art GDE modeling.

We will hence adopt the following *strategy*: We will use the GCE spectrum and associated statistical errors from model F only, which gives formally the best-fit to the *Fermi*-LAT data in our ROI. In fits to the GCE spectrum we then only consider the *empirical* model systematics, and neglect the theoretical ones. Given the small scatter for the GCE spectrum that we find for different GDE models, this is well justified. We checked explicitly that using different GDE model as starting point in the spectral fits would not alter our results significantly (see appendix C.2). Hence, we consider our approach as statistically sound and sufficiently robust to derive meaningful results.

We will introduce general aspects of fits with correlated errors in subsection 5.1, and then test the most common interpretations of the GCE emission in terms of a number of DM and astrophysical toy models in subsection 5.2 and 5.3.

5.1 Spectral fits with correlated errors

For spectral fits to the extracted GCE spectra (as they are shown in figures 14 and 16), we make use of a χ^2 function with a non-diagonal covariance matrix. This allows to take into account the correlated empirical model systematics that we derived in the previous section.²²

The χ^2 function is given by

$$\chi^2 = \sum_{ij} \left(\frac{d\tilde{N}}{dE_i}(\boldsymbol{\theta}) - \frac{dN}{dE_i} \right) \Sigma_{ij}^{-1} \left(\frac{d\tilde{N}}{dE_j}(\boldsymbol{\theta}) - \frac{dN}{dE_j} \right), \quad (5.1)$$

with the covariance matrix

$$\Sigma_{ij} = (\sigma_i^{\text{stat.}})^2 \delta_{ij} + \Sigma_{ij, \text{mod}}^{\text{trunc}} + \Sigma_{ij, \text{res}}. \quad (5.2)$$

Here, dN/dE_i ($d\tilde{N}/dE_i$) denotes the measured (predicted) GCE flux in the i^{th} energy bin, $\boldsymbol{\theta}$ the model parameters, $\sigma_i^{\text{stat.}}$ the corresponding statistical error, $\Sigma_{ij, \text{mod}}^{\text{trunc}}$ the truncated (24×24) covariance matrix accounting for empirical model systematics, and $\Sigma_{ij, \text{res}}$ the residual systematics at sub-GeV energies that we discussed in subsection 4.2.3. For fits to the *segmented* GCE template fluxes, the corresponding (240×240) correlation matrix is taken to be block diagonal in the different GCE segments (we neglect segment-to-segment correlations), and we set $\Sigma_{ij, \text{res}} = 0$, as it is not very relevant for morphology fits.

Like above, all fits are performed using the minimizer `Minuit`. For the two-dimensional contour plots, we define the one, two and three sigma contours (which we show in the plots if not otherwise stated) at $\Delta\chi^2 = 2.3, 6.2$ and, 11.8 , and derive them with the `minos` algorithm. Note that we will neglect the effects of the finite energy resolution of *Fermi*-LAT, which is below 15% in the energy range of interest, but could be easily incorporated.

5.2 Dark Matter models

The most exciting interpretation of the GCE is that it is caused by the annihilation of DM particles, and indeed all of the previous studies analyzing *Fermi*-LAT data focus on this possibility [49–55, 57]. Instead of presenting fits to a large number of DM annihilation spectra, we will here simply concentrate on the most common cases discussed in the literature. We concentrate on the hadronic annihilation channels $\bar{b}b$ and $\bar{c}c$ and on pure $\tau^+\tau^-$ lepton final states. The gamma-ray yields are taken from `DarkSUSY 5.1.1` [123].

In the left panel of figure 18 we show the constraints in the $\langle\sigma v\rangle$ -vs- m_χ plane that we obtain from a fit to the GCE spectrum in figure 14. Correlated model systematics are taken into account as discussed above. We find that both $\bar{b}b$ and $\bar{c}c$ provide rather good fits to the data, with p -values around 0.4–0.5 (see table 4). For $\tau^+\tau^-$ final states, the p -value is with 0.065 significantly lower, though it remains marginally compatible with the data at 95% CL. We find that in the canonical case of $\bar{b}b$ final states, DM masses around $m_\chi = 49_{-5.4}^{+6.4}$ GeV are favored by the data, and an annihilation cross-section of $\langle\sigma v\rangle = 1.76_{-0.27}^{+0.28} \times 10^{-26} \text{ cm}^3 \text{ s}^{-1}$.²³

In the right panel of figure 18 we show how the cross-section $\langle\sigma v\rangle$ depends on the slope γ of the adopted NFW profile, for the case of annihilation into $\bar{b}b$ final states with the DM

²²It is worth pointing out that summing systematic and statistical errors in quadrature, which is common practice in the DM-phenomenology literature, does *not* lead to the weakest (or ‘most conservative’) constraints on model parameters in almost all of the cases.

²³We remind that we adopt a local DM density of $\rho_\odot = 0.4 \text{ GeV cm}^{-3}$.

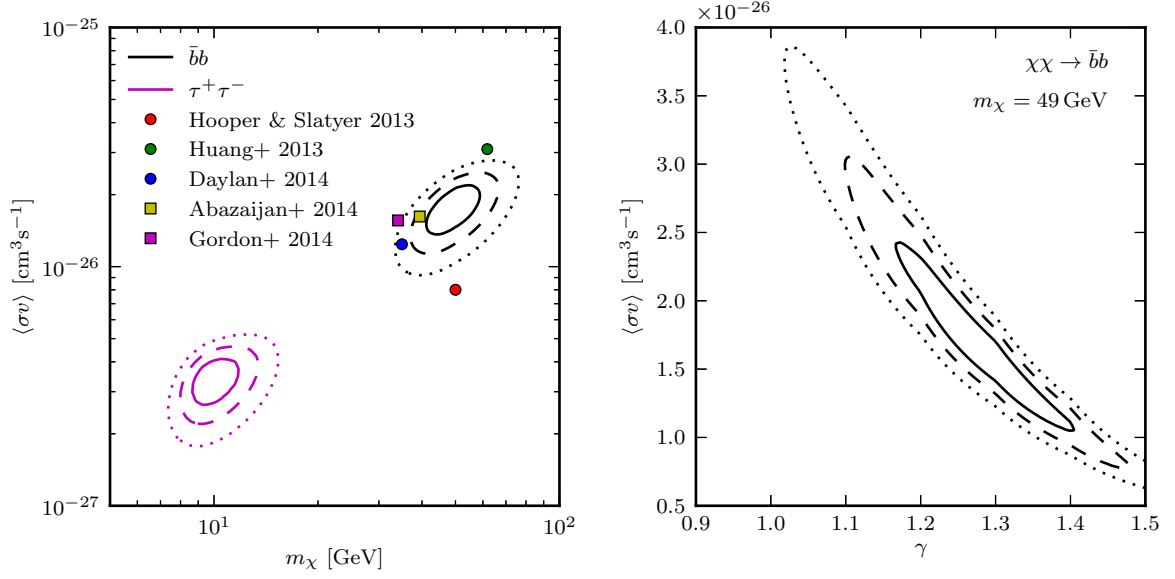


Figure 18. *Left panel:* Constraints on the $\langle\sigma v\rangle$ -vs- m_χ plane for three different DM annihilation channels, from a fit to the spectrum shown in figure 14 (cf. table 4). *Colored points (squares)* refer to best-fit values from previous Inner Galaxy (Galactic center) analyses (see discussion in section 6.2). *Right panel:* Constraints on the $\langle\sigma v\rangle$ -vs- γ plane, based on the fits with the ten GCE segments.

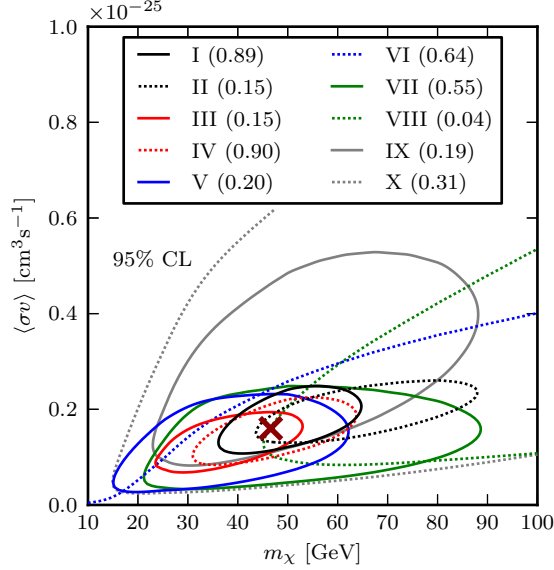


Figure 19. Constraints on the $\langle\sigma v\rangle$ -vs- m_χ plane at 95% CL, individually for the GCE template segments shown in figure 15, for the channel $\chi\chi \rightarrow b\bar{b}$. The cross indicates the best-fit value from a fit to all regions simultaneously ($m_\chi \simeq 46.6$ GeV, $\langle\sigma v\rangle \simeq 1.60 \times 10^{-26} \text{ cm}^3\text{s}^{-1}$). Note that we assume a NFW profile with an inner slope of $\gamma = 1.28$. The individual p -values are shown in the figure legend; the combined p -value is 0.11.

mass fixed at 49 GeV. This plot is based on the fluxes from the segmented GCE template, see figure 16. As expected, the cross-section is strongly correlated with the profile slope. We

find best-fit values of $\gamma = 1.28^{+0.8}_{-0.7}$ and $\langle\sigma v\rangle = 1.65^{+0.5}_{-0.4} \times 10^{-26} \text{ cm}^3 \text{ s}^{-1}$.

Note that in the case of $\gamma = 1.2$, we obtain actually a somewhat larger cross-section than in the left panel, though still marginally consistent within one sigma. By using different values of γ in the template analysis that lead to figure 14, we checked that the γ -dependence of the cross-section shown in the left panel of figure 18 is practically identical to the one shown in the right panel.

The constraints on the cross-section that we show in the right panel of figure 18 are, for a fixed value of γ , somewhat tighter than in the left panel. This is likely related to the neglect of segment-to-segment correlations when determining the empirical model systematics, which then tend to average out in fits to the spectrum. This is a caveat of spectral fits based on the segmented GCE templates. For that reason, we recommend using the spectral constraints derived from the non-segmented GCE template instead, as shown in figure 14 and used in the left panel of figure 18.

In figure 19, we show constraints at 95% CL on the $\langle\sigma v\rangle$ -vs- m_χ plane that are obtained from fits to the spectra from the individual GCE segments shown in figure 16. We consider for definiteness only the case of annihilation $\bar{b}b$ final states, and assume our contracted NFW profile with an inner slope of $\gamma = 1.28$, which gives the best fit in this case. Again, we fully take into account the empirical model systematics as discussed above. We find that the resulting constraints on the GCE spectrum that we derive from the individual GCE segments are in mutual good agreement to within 95% CL. There is no obvious bias for the GCE in the north/south or east/west direction, though at higher latitudes the preferred DM masses are slightly higher.

The constraints in figure 19 are also in good agreement with the central value that we obtain from a fit in all of the ten segments simultaneously (assuming $\gamma = 1.28$; note that this is different from a fit using a single GCE template), which yields $m_\chi \simeq 46.6 \text{ GeV}$ and $\langle\sigma v\rangle \simeq 1.60 \times 10^{-26} \text{ cm}^3 \text{ s}^{-1}$. We show the corresponding p -values in the figure label. For the hypothesis of a single uniform excess spectrum (again using a $\bar{b}b$ spectrum with m_χ and $\langle\sigma v\rangle$ as the two fitting parameters, keeping $\gamma = 1.28$ fixed) we obtain a combined p -value of 0.11.

We find that the hypothesis of a spherically symmetric excess emission with a uniform energy spectrum is compatible with the Fermi-LAT data from the inner Galaxy to within 95% CL.

Obviously, this is not a proof that the emission absorbed by the GCE template in different parts of our ROI is caused by the *same* physical mechanism, but the result is rather suggestive. We will below proceed under the assumption that the entire GCE emission is generated by a single extended source with uniform spectrum, and explore the consequences of this hypothesis.

5.3 Astrophysical models

We start this subsection with a simple broken power-law fit to the GCE spectrum. This spectrum is so generic that it is capable of approximately describing a large number of scenarios, and it is given by

$$\frac{dN}{dE} = \zeta \left(\frac{E}{E_{\text{break}}} \right)^{-\alpha} \quad \text{with} \quad \alpha = \begin{cases} \alpha_1 & \text{if } E < E_{\text{break}} \\ \alpha_2 & \text{if } E \geq E_{\text{break}} \end{cases}, \quad (5.3)$$

where $0 > \alpha_1 > \alpha_2$ denote respectively the spectral indices above and below the break energy E_{break} , and ζ is a normalization parameter.

Spectrum	Parameters	χ^2/dof	$p\text{-value}$
broken PL	$\alpha_1 = 1.42_{-0.31}^{+0.22}, \alpha_2 = 2.63_{-0.095}^{+0.13}, E_{\text{break}} = 2.06_{-0.17}^{+0.23} \text{ GeV}$	1.06	0.47
DM $\chi\chi \rightarrow \bar{b}b$	$\langle\sigma v\rangle = 1.76_{-0.27}^{+0.28} \times 10^{-26} \text{ cm}^3 \text{ s}^{-1}, m_\chi = 49_{-5.4}^{+6.4} \text{ GeV}$	1.08	0.43
DM $\chi\chi \rightarrow \bar{c}c$	$\langle\sigma v\rangle = 1.25_{-0.18}^{+0.2} \times 10^{-26} \text{ cm}^3 \text{ s}^{-1}, m_\chi = 38.2_{-3.9}^{+4.6} \text{ GeV}$	1.07	0.44
PL with exp. cutoff	$E_{\text{cut}} = 2.53_{-0.77}^{+1.1} \text{ GeV}, \alpha = 0.945_{-0.5}^{+0.36}$	1.37	0.16
DM $\chi\chi \rightarrow \tau^+\tau^-$	$\langle\sigma v\rangle = 0.337_{-0.048}^{+0.047} \times 10^{-26} \text{ cm}^3 \text{ s}^{-1}, m_\chi = 9.96_{-0.91}^{+1.1} \text{ GeV}$	1.52	0.065

Table 4. Results of spectral fits to the GCE emission as shown in figure 14, together with $\pm 1\sigma$ errors (which include statistical as well as model uncertainties, see text). We also show the reduced χ^2 , and the corresponding p -value. The best-fit is given by a broken power-law, though annihilation into $\bar{b}b$ final states is completely compatible with the observed spectrum as well. We find that even annihilation into $\tau^+\tau^-$ cannot be excluded with 95% CL significance.

In the left panel of figure 20, we show constraints on the broken PL spectrum in the α_1 -vs- α_2 plane, obtained from a fit to the data shown in figure 14. The break position is left free to vary in the fit. As best-fit parameters for the slopes we find $\alpha_1 = 1.42_{-0.31}^{+0.22}$ and $\alpha_2 = 2.63_{-0.10}^{+0.13}$ (cf. table 4); the position of the break is given by $E_{\text{cut}} = 2.06_{-0.17}^{+0.23} \text{ GeV}$. We find that a simple broken PL provides already a very good fit to the data, with a p -value of 0.47. This is marginally smaller than the p -values that we found for the DM annihilation spectra.

Another generic and simple spectrum is a power-law with an exponential cutoff, as given by

$$\frac{dN}{dE} = \zeta \left(\frac{E}{1 \text{ GeV}} \right)^{-\alpha} e^{-E/E_{\text{cut}}} . \quad (5.4)$$

Here, α is the spectral index, E_{cut} denotes the cutoff energy, and ζ is a normalization parameter. Constraints on the α -vs- E_{cut} plane that we found from a fit to the GCE spectrum in figure 14 are shown in the right panel of figure 20. In this figure, we also indicate the point in the parameter space that corresponds to the stacked spectrum of MSPs that was derived from a reanalysis of the *Fermi*-LAT data in ref. [35]. We find that the best-fit is obtained for a cutoff energy of $E_{\text{cut}} = 2.53_{-0.77}^{+0.11}$ and a spectral index of $\alpha = 0.945_{-0.5}^{+0.36}$. However, the p -value for this fit is with 0.16 relatively poor. Again, the best-fit parameters are summarized in table 4.

Finally, we explore the *morphology* of the GCE with a simple parametric model. As a spatial template, we consider a generic spherically symmetric volume emissivity with a radial dependence given by

$$q \propto r^{-\Gamma} e^{-r/R_{\text{cut}}} , \quad (5.5)$$

where r denotes the Galacto-centric distance. In contrast to the generalized NFW profile, it features a well-defined spatial cutoff at the Galacto-centric distance R_{cut} , which makes it possible to quantify the spatial extent of the GCE emission in the sky (note that the spatial index $\Gamma \approx 2\gamma$ at distances close to the GC).

We perform a fit to the GCE fluxes as shown in figure 16, assuming as fiducial spectrum the $\bar{b}b$ spectrum from table 4 with fixed mass and free normalization (the precise form of the spectrum does not matter much). We find that the template can fit the data as well as the NFW profile (which is not a surprise given that we allow Γ and R_{cut} freely to vary).

Constraints on the parameters in the Γ -vs- R_{cut} plane are shown in the left panel of figure 21. We find, for a freely varying Γ , as lower limit on the spatial extend of the excess $R_{\text{cut}} > 1.1 \text{ kpc}$ at 95% CL. This corresponds to an angular distance of about 7.4° from the GC. The constraint on Γ is for large values of R_{cut} about $\Gamma \sim 2.2\text{--}2.9$ (95% CL), which is compatible with what we found for the generalized NFW profile.

In the right panel of figure 21, we show constraints on the GCE intensity-vs- Γ plane, leaving R_{cut} free to vary. The intensity of the GCE emission is here determined at an energy of 2 GeV and at an angular distance of $\psi = 5^\circ$ from the GC. We find that $\psi = 5^\circ$ is a rather good pivot point for the determination of the signal brightness in the adopted inner Galaxy ROI, since the flux at this point is largely independent of the profile slope Γ .

It is instructive to compare the flux in the right panel of figure 21 to an extrapolation of the GeV excess emission that is seen in the inner few degrees of the Galactic center. We adopt here results from refs. [54, 65], which analyzed gamma-ray emission from the inner $7^\circ \times 7^\circ$, and found profile slopes in the range $\Gamma \approx 2\gamma = 2.2\text{--}2.4$. Taking their best-fit values for $b\bar{b}$ final states, we calculate what flux would be expected 5° away from the GC at 2 GeV, and indicate these values in figure 21. We also show how this flux would approximately vary when different values of Γ are adopted (we require here that the flux in the $7^\circ \times 7^\circ$ region remains constant). We conclude that for values of roughly $\Gamma \sim 2.3\text{--}2.6$ the excess emission in the inner Galaxy can indeed be interpreted as the high-latitude counterpart of the GeV excess seen in the inner few degrees.

Finally, as shown in the right panel of figure 21, a profile slope $\Gamma = 2.2$ is about the smallest value for which one can interpret the GCE in the inner Galaxy as extended counterpart of the GeV excess that is seen in the inner few degrees of the Galaxy. For this value of Γ , we obtain a stronger lower limit on the extent of the GCE, namely $R_{\text{cut}} > 1.48 \text{ kpc}$ at 95% CL. The corresponding angular distance from the GC is $\psi = 10.0^\circ$.

6 Discussions

6.1 Astrophysical interpretations

In what follows we briefly discuss the astrophysical interpretations that have been put forward in light of the results of section 5.3. Astrophysical processes that might explain the GC excess fall in two main categories: The emission from an unresolved population of sources concentrated at the GC and diffuse emission related to the interaction of CRs with the ISM and radiation fields in the extreme environment of the GC.

As for the emission from an unresolved point source population, MSPs has been for quite some time promising candidates for the explanation of the anomalous excess. Indeed, the gamma-ray MSPs source spectrum is measured to be compatible with a power-law with exponential cutoff usually at $E_{\text{cut}} \sim 2\text{--}3 \text{ GeV}$, thus suggesting a compatibility with the GCE spectrum. Recently, the best-fit (stacked) spectrum of the 61 MSPs detected by *Fermi*-LAT in 5.6 years has been parametrized by $E_{\text{cut}} = 3.78^{+0.15}_{-0.08} \text{ GeV}$ and $\alpha = 1.57^{+0.02}_{-0.01}$ [35]. Those parameter values lie inside our 99% CL contour of fig. 20, where the red cross represents the best fit result of ref. [35]. In section 5.3, we find that a power-law with exponential cutoff prefers a cutoff energy of $E_{\text{cut}} = 2.53^{+1.1}_{-0.77} \text{ GeV}$ and a slope of $\alpha = 0.945^{+0.36}_{-0.5}$. Our spectral parameters are in agreement with previous results from analyses of the inner few degrees ($7^\circ \times 7^\circ$ around the GC) of the Galaxy. Ref. [54] found $E_{\text{cut}} = 1.65 \pm 0.20 \text{ GeV}$ and

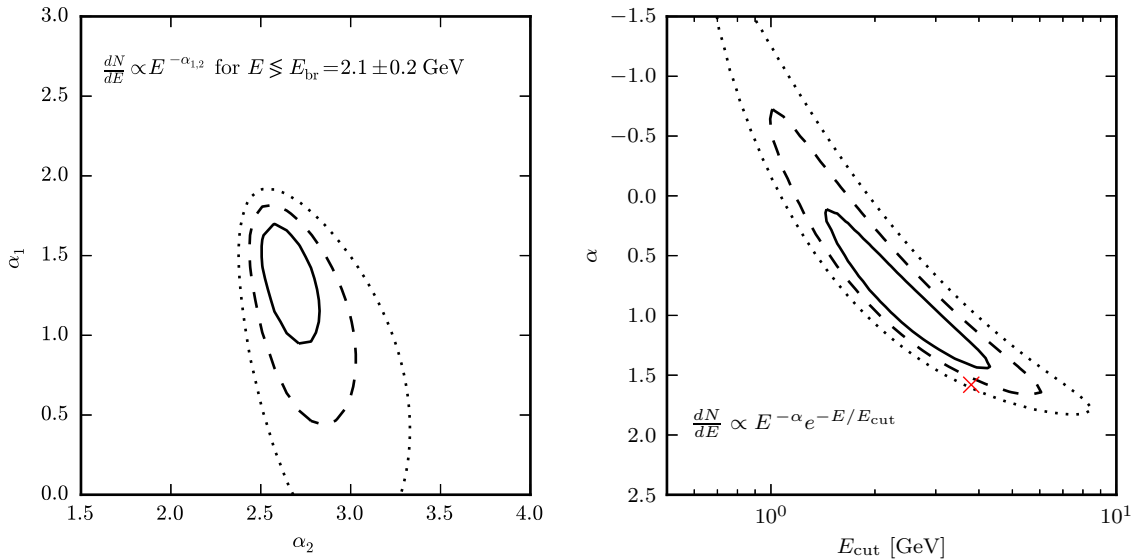


Figure 20. *Left panel:* Constraints on the two spectral indices of a broken power-law, where we leave the break position free to float, from a fit to the spectrum in figure 14. *Right panel:* Constraints on a power-law with exponential cutoff. For comparison we also show the values corresponding to observed MSPs from ref. [35], where red point shows the best-fit value from a fit to a stacked MSP spectrum. We emphasize that, although the spectrum appears to be marginally compatible, the normalization of the observed GCE is too high by a factor of $\simeq 20 - 30$ [68, 70] to be explained by MSPs.

$\alpha = 0.45 \pm 0.21$ (full model), while the values $E_{\text{cut}} = 3_{-1}^{+2}$ GeV and $\alpha = 1.4 \pm 0.3$ were derived in ref. [53] with the main difference being different methods for background and point source modeling.

In our analysis, the power-law with an exponential cutoff performs less well than the $\bar{b}b$, $\bar{c}c$ spectra or the broken power-law, as shown in table 4. Most interestingly, this is not so much due to the steep rise in the spectrum at low energies as is visible in figure 17, but to the sizable amount of excess emission at high energies above 10 GeV, which is difficult to accommodate with a power-law with an exponential cutoff. A sub-exponential cutoff (as indicated from stacked MSP spectra in ref. [35]) would here certainly help to improve the quality of the fit.

Additionally, it has been shown that the spatial distribution of MSPs is not easily able to account for the spatial extension of the GCE [68, 69]. Indeed, observed gamma-ray MSPs are well described by a disk-like distribution. In that case, predictions of the unresolved flux originating from MSPs generally estimate that this population might contribute up to 5%–10% of the excess emission in both GC and inner Galactic regions (see refs. [68, 69]).

The MSPs spatial profile has to steeply increase towards the center like approximately $\propto r^{-2.5}$ to be compatible with the morphology of the GCE. Hence, a population associated with the *bulge* is required (and to certain extent expected), yet a bulge component can not explain the extension of the signal up to $\sim 15^\circ$ [68]. To derive the spatial distribution of bulge MSPs, one can use low-mass X-ray binaries (LMXB) that are believed to be MSP progenitors as proxies. Measurements of the INTErNational Gamma-Ray Astrophysics Laboratory (INTEGRAL) suggest that the LMXB profile in the centre of the Milky Way could be steeper than $\propto r^{-2}$. One measure is available for LMXB in M31 [124]. Using that, ref. [125]

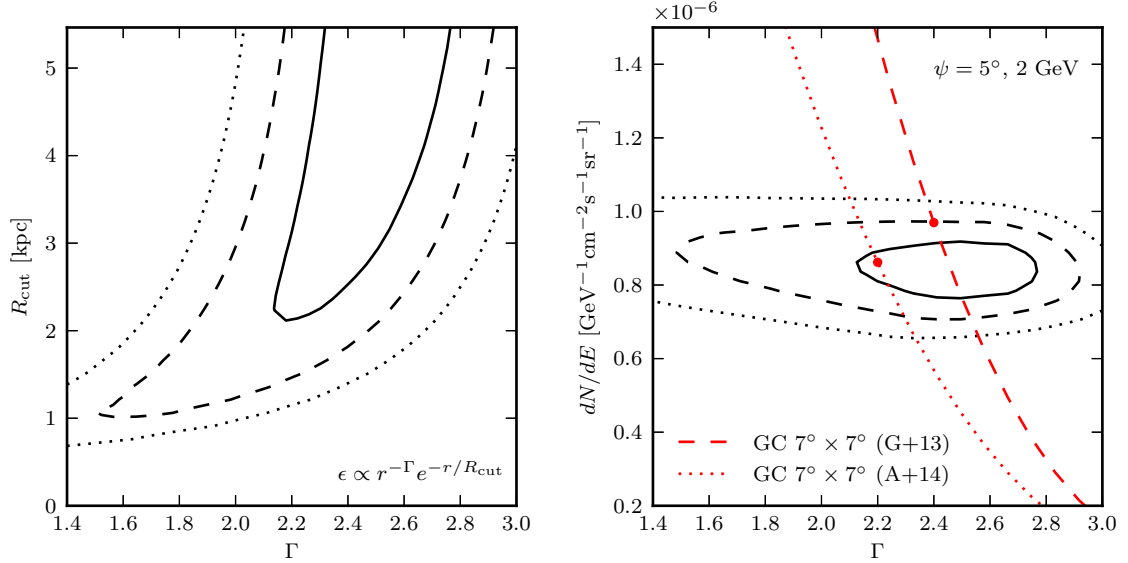


Figure 21. *Left panel:* Constraints on the morphology of the GCE, assuming a spherically symmetric emission profile with a radial dependence that follows a power-law with index Γ and exponential cutoff at radius R_{cut} as indicated in the panel. A $\bar{b}b$ spectrum with $m_\chi = 49$ GeV is adopted as energy (results are similar for other spectra). *Right panel:* Confidence contours for the flux of the GCE at 5° from the GC, and at an energy of 2 GeV, as function of the radial slope Γ (we assume a $\bar{b}b$ spectrum with $m_\chi = 49$ GeV, R_{cut} is left free to float in the fit). The *red lines* show an extrapolation to higher latitudes of the flux from the inner $7^\circ \times 7^\circ$ of the Galaxy, as determined in ref. [54] (*dotted line*) and ref. [65] (*dashed line*), with the *dots* being the actually measured values, and the lines being the expected scaling as function of Γ (see text for details).

claimed that MSPs may account for the emission in the inner 2° about the GC. Yet, making a connection between observed MSPs and LMXBs at globular clusters and with bright LMXBs observations towards the GC [70] found that only $\sim 5\%$ of the excess emission can be accounted for by MSPs laying at the inner 5° ($\simeq 0.8$ kpc).

In conclusion, our current knowledge of MSPs makes it questionable whether they are the main source of the GCE. Nonetheless, the excess emission may still be interpreted in terms of an unresolved diffuse emission from a yet unidentified source population. Those would be concentrated at the GC, without obvious members sitting close to us, which would help derive information on their spectra, spatial distribution, luminosity function or multi-wavelength properties.

Non-equilibrium processes involving burst-like events during an active past of our GC have been explored as well, see refs. [75, 76]. Although they deserve a careful study in light of the data, we will only mention them briefly at this point. In the case of one or more proton bursts injected from a few kilo-years up to a few mega-years ago [75], the induced morphology would be in general more disk-like than the GCE, trace the gas distribution and extend up from few degrees to tens of degrees depending on the age of the event. On the other hand, the injection of an additional electron population with total energy $\sim 10^{53}$ erg on the timescale of few mega-years ago [76] is expected to lead to a more symmetric emission around the GC because the ICS traces the smooth radiation field distribution, but no attempts of performing template fits based on this scenario have been made yet. In this case, the induced spectrum would need to reproduce, depending in the initial conditions and properties of the event, our

measured broken power-law spectrum (with $\alpha_1 \sim 1.42$, $\alpha_2 \sim 2.63$, $E_{\text{break}} \sim 2.06$ GeV as quoted in table 4).

6.2 A signal from dark matter annihilation?

As demonstrated in section 5.2, the spectrum and morphology of the GCE are compatible with a signal from WIMP DM annihilation in the halo of the Milky Way. Fits with typical annihilation spectra are found to give good p -values, despite the fact that, at first sight, the peaked DM spectra do not appear to be a good representation of the data shown e.g. in figure 17. This is due to the strong correlations of the empirical model systematics in energy, which to some degree allow a further subtraction of ICS-like and π^0 -like background spectra. When performing fits to the data this results especially at low and high energies, where the GCE flux is already small, in an additional suppression of the GCE spectrum, leading to a more pronounced peak at 1–3 GeV.

The results quoted in table 4 prefer annihilation into quarks ($\bar{b}b, \bar{c}c$), while heavy leptonic final states are almost excluded at 95% CL. For a generalized NFW DM spatial distribution with slope $\gamma=1.2$ and the representative case of annihilation into $\bar{b}b$, our fits prefer a DM mass in the range $m_\chi = 43.6\text{--}55.4$ GeV and a velocity-averaged annihilation cross-section of $\langle\sigma v\rangle = 1.76^{+0.28}_{-0.27} \times 10^{-26} \text{ cm}^3 \text{ s}^{-1}$. Compared to findings in the previous literature, our results are in general in good agreement, although we find typically somewhat larger masses and cross-sections. We will present a more detailed comparison in the following. In figure 18 (left panel), we display the points corresponding to the best-fit results from previous works we compare with. Notice that the $\langle\sigma v\rangle$ values have been opportunely rescaled for a fair comparison.²⁴

The first paper about the *inner Galaxy* found values $m_\chi \sim 50$ GeV and $\langle\sigma v\rangle \sim 0.8 \times 10^{-26} \text{ cm}^3 \text{ s}^{-1}$, [62], which fall largely outside our 99% CL contour. The results of the follow-up work in ref. [63] at latitudes $10^\circ < |b| < 20^\circ$ suggest a somewhat larger value for the WIMP mass $m_\chi \sim 61.8$ GeV and cross-section $\langle\sigma v\rangle \sim 3.1 \times 10^{-26} \text{ cm}^3 \text{ s}^{-1}$ (for e.g. $\bar{b}b$), which lies slightly outside our 99% CL contour. The most recent analysis of the *inner Galaxy* was presented in ref. [55], and pointed towards a DM mass $m_\chi \sim 35$ GeV (lower than our best-fit value) and cross-section $\langle\sigma v\rangle \sim 1.24 \times 10^{-26} \text{ cm}^3 \text{ s}^{-1}$ (for $\bar{b}b$), that agree with our results at 95% CL. Compared to this most recent analysis, there are a number of differences in the analysis set up. Ref. [55] uses e.g. the *Fermi*-LAT model P6V11 as their baseline GDE model to subtract diffuse backgrounds, which likely absorbs more ICS emission than any of our GDE models. Moreover, ref. [55] performs a full-sky fit, while we concentrate on a smaller region. In general, we find that with respect to previous results from the *inner Galaxy* our spectral fits do not show a strong trend and are broadly consistent.

²⁴To fairly compare previous findings with our results, we firstly rescale the DM profiles used in the previous literature. In particular, the generalised NFW profile can be reparametrized as:

$$\rho(r) = \rho_\odot \left(\frac{r}{r_\odot} \right)^{-\gamma} \left(\frac{(1 + r_\odot/r_s)}{(1 + r/r_s)} \right)^{3-\gamma}, \quad (6.1)$$

In the limit of small radii, we rescale the cross-sections in the literature such to match our parameters choice for ρ_\odot, r_\odot, r_s . We then further rescale the cross-sections in order to take into account the different mass and γ best-fit values found in the work we are comparing with. To this end, we derive the corresponding $\langle\sigma v\rangle$ -vs- γ contours with our fitting procedure (for m_χ fixed). In the text, we quote the final *rescaled* cross-section we compare with in the $\langle\sigma v\rangle$ -vs- m_χ plane of figure 18.

There is a number of analyses concentrating on studying the GCE in the *inner few degrees* of the Galaxy. Comparing our results with the results of the analyses of the GC is a quantitative way to test the consistency of the excesses observed at the GC and in the inner Galaxy in light of the DM interpretation. In ref. [54], the preferred mass and cross-section values for $\bar{b}b$ annihilation are found to be $m_\chi \sim 40$ GeV and $\langle\sigma v\rangle \sim 1.62 \times 10^{-26} \text{ cm}^3 \text{ s}^{-1}$, for an inner slope of the generalized NFW profile of $\gamma = 1.1$. We find that this results is in well in agreement with our analysis, lying inside the 95% CL contour. Instead, the results from ref. [65], $m_\chi \sim 34.1$ GeV and $\langle\sigma v\rangle \sim 1.56 \times 10^{-26} \text{ cm}^3 \text{ s}^{-1}$ (where $\gamma = 1.2$), agree with our findings at 99% CL. Lastly, we show in the right panel of figure 21 an extrapolation of the GeV excess emission measured in the inner $7^\circ \times 7^\circ$ of the Galaxy to higher latitudes, based on the results from refs. [54, 65] (see discussion above). For profile slopes of $\gamma \approx 1.15\text{--}1.3$ we indeed find good agreement between these and our results from the inner Galaxy.

We briefly mention the constraints on DM annihilation that come from other targets and messengers (see ref. [126] for a recent discussion in context of the GCE). Some of these constraints are already in mild tension with or show mild support for the DM interpretation of the GCE, and in the near future these probes will further help to support or exclude this possibility.

For gamma rays, the most robust limits on DM self-annihilation in hadronic final states (including also $\tau^+\tau^-$) come currently from observations of dwarf spheroidal galaxies [127–129], and probe DM annihilation down to the thermal cross-section for masses less than about 10 GeV (for $\bar{b}b$ final states). Interestingly, the most recent combined analysis of 15 dwarfs might already indicate first signs for a DM signal compatible with the GCE (at the level of 2.3σ) [127]. Antiprotons provide also a strong probe for DM [97, 130, 131], though uncertainties in the propagation assumptions remain relevant [96]. For the most common CR propagation scenarios they are already in mild tension with the DM interpretation of the GCE [98, 126]. For leptonic two-body final states the strongest limits come from a spectral analysis of the positron fraction measured by AMS-02 [132, 133], which excludes a thermal rate for $\chi\chi \rightarrow e^+e^-$ ($\chi\chi \rightarrow \mu^+\mu^-$) up to DM masses of $m_{\text{DM}} \simeq 200$ GeV (100 GeV), so that this channel can only play a very subdominant role in models explaining the GCE [126]. Limits from radio observations of the GC are in some tension with the GCE DM interpretation, unless the DM profile at the GC is somewhat cored out [126], or strong convective winds or ICS energy losses are important [134]. Finally, limits from observations of the cosmic microwave background constrain leptonic models for DM annihilation [135–139], though not at a level that is relevant for the GCE right now.

6.3 The energy spectrum at sub-GeV energies

Results below 1 GeV are potentially subject to large systematics related to the relatively large PSF of *Fermi*-LAT at those low energies. At the same time, the low-energy part of the GCE spectrum is of utmost importance when aiming at a discrimination of DM signals from astrophysical processes, see ref. [55]. Indeed, in the prototypical case of $\bar{b}b$ final states, DM spectra are predicted to follow a rising power-law with a spectral index of roughly ~ 1.5 and with a pronounced cutoff at energies above $\sim 0.05 m_\chi$. The observation of such a spectrum with high accuracy would be a strong support for a DM interpretation of the GCE.

We think our results below 1 GeV are reliable for a number of reasons. As described in section 4.2.3, we estimated the impact of a number of analysis choices that we make throughout our analysis. These include details about the point source mask, the treatment

of the *Fermi*-LAT PSF, and the impact of fixed IGRB and *Fermi* bubble contributions. As shown in figure 13. Some of these effects indeed start to dominate over the statistical error at energies below 1 GeV. We account for these uncertainties by additional terms in the covariance matrix for the spectral fits. In appendix C.2 we furthermore show that our results do not change much when neglecting these above systematics in the fit, or when instead restricting the fits to ranges above 600 MeV. Lastly, the absence of a stronger longitudinal variation at latitudes $4^\circ \leq |b| \leq 6^\circ$ as shown in the lower left panel of figure 9 is a visible indicator for the GCE spectrum featuring a spectral index harder than ~ 2 at energies below 2 GeV.

Our analysis supports a rise at energies below 1 GeV, with a spectral index harder than ~ 2 as can be seen e.g. in the bottom left panel of figure 9. Moreover, figure 16 suggests that such a low-energy trend extends up to 5° – 10° in latitude and higher. In the case of the broken power-law fit, the low-energy slope is $\alpha_1 = 1.42^{+0.22}_{-0.31}$, while in case of the power-law with exponential cutoff we obtain $\alpha = 0.945^{+0.36}_{-0.5}$, with the harder value being related to the GCE excess emission above 10 GeV. As discussed above, the spectrum from $\bar{b}b$ is perfectly consistent with the data.

7 Conclusions

During the last few years the presence of a gamma-ray excess at GeV energies and towards the GC has been suggested by a sequence of studies performed using *Fermi*-LAT gamma-ray data [49, 50, 53–57, 65, 125, 140]. Given the sphericity of the excess, its amplitude and the fact that it is centered within $\sim 0.05^\circ$ of the GC [55], a large number of follow-up studies have been interpreted this excess as a signal from DM self-annihilation. Additionally, less exotic possibilities, such as populations of dim point sources or diffuse emission from recently injected CRs, have also been proposed. Important ingredients for understanding the characteristics and the origin of this excess are first its morphology, namely its extension to Galactic latitudes above the inner few degrees, and second its energy spectrum.

Any description of the excess emission necessitates the adoption of several assumptions on all of the relevant Galactic diffuse and point-source backgrounds. One of the major limitations of previous high latitude analyses is the lack of a thorough study of background model systematics, which often causes overly constraining and sometimes biased results. As an example, previous analyses often adopted the P6V11 model, which provides a prediction for only the *total* Galactic diffuse emission (π^0 + bremsstrahlung + ICS). We demonstrated that the P6V11 model features an extremely hard ICS emission at energies above 10 GeV (figure 6), which – when used in a template analysis – easily over-subtracts components in regions relevant for DM searches, potentially leading to pronounced drops in the spectrum at energies around 10 GeV, as e.g. found in refs. [55, 62].

In this paper, we reanalyzed the *Fermi*-LAT data in the *inner Galaxy*. More specifically, we concentrated on high Galactic latitudes $|b| \geq 2^\circ$ in a Galacto-centric box of $40^\circ \times 40^\circ$. Given the often large variations in the predicted spectra and morphologies of the Galactic diffuse emission components (figures 3, 5 and 4), we modeled the three contributions π^0 , bremsstrahlung and ICS as separate templates. To probe the associated uncertainties in the Galactic diffuse emission, we used existing models in the literature [58] as well as our own models. The latter account for even extreme variations in the CR source distribution and injection, the gas distribution, the diffusion of CRs, convection and re-acceleration, the

interstellar radiation field distribution and the distribution and amplitude of the Galactic magnetic field. Equipped with these templates, and additional templates for the *Fermi* bubbles, the IGRB and known point sources, we performed a multi-linear regression analysis of the *Fermi*-LAT data in 24 energy bins from 300 MeV to 500 GeV. We repeated that analysis in several test regions along the Galactic disk. Our main results can be summarized as follows.

- We confirmed the existence of a diffuse Galacto-centric excess emission (“Galactic center excess”) in the inner Galaxy, above the modeled astrophysical backgrounds. We showed that the spectral properties are remarkably stable against theoretical model systematics, which we bracketed by exploring a large range of Galactic diffuse emission models (figure 7). The excess emission shows a clear peak at 1–3 GeV, which rises steeply at lower energies, and follows a power-law with slope ~ -2.7 above.
- We found residuals above the modeled astrophysical backgrounds in various test regions along the Galactic plane, which are of almost the same size as the Galactic center excess (figure 11). By means of a principal component analysis we traced these residuals back to non-uniform variations in the normalizations and spectral indices of the primary Galactic diffuse emission components (figure 12). We folded these uncertainties back into the analysis of the Galactic center excess as an estimate for the empirical model systematics (figure 14).
- In order to explore the morphology of the excess emission, we split the adopted Galactic center excess template in ten segments (figure 15), and repeated the above estimate of theoretical and empirical model systematics individually for each of them, finding consistent results (figure 16).
- We showed that the hypothesis of a spherically symmetric and spectrally uniform excess emission is compatible with the data from the inner Galaxy at 95% CL (right panel of figure 18). Under that hypothesis, and assuming a radial profile of the volume emissivity with a floating index Γ and an exponential cutoff R_{cut} , we found a robust lower limit on the radial extension of the excess of $R_{\text{cut}} > 1.1 \text{ kpc}$ at 95% CL. This corresponds to an angular distance from the GC of 7.4° (left panel of figure 21). For a radial index of $\Gamma = 2.2$, which is compatible with previous results from the inner few degrees of the Galaxy (right panel of figure 21), we obtained an even stronger limit of $R_{\text{cut}} > 1.48 \text{ kpc}$ at 95% CL, which corresponds to an angular distance of 10.0° .
- We do *not* confirm previous results that indicated that the Galactic center excess spectrum would drop to zero at $E \gtrsim 10 \text{ GeV}$ energies (figure 14). However, when we included the existing large model systematics as correlated errors into the spectral fits, we found that the excess spectrum is well described both by a broken power law with spectral indices $\alpha_1 = 1.42^{+0.22}_{-0.31}$ and $\alpha_2 = 2.63^{+0.13}_{-0.10}$ and break energy $E_{\text{break}} = 2.06^{+0.23}_{-0.17} \text{ GeV}$ (figure 20), and by the gamma-ray spectrum produced by DM particles annihilating into $\bar{b}b$ final states. In the latter case, we obtained as best-fit values $\langle\sigma v\rangle = 1.76^{+0.28}_{-0.27} \text{ cm}^3 \text{ s}^{-1}$ and $m_\chi = 49^{+6.4}_{-5.4} \text{ GeV}$ (figure 18). In both cases, the p -values of the spectral fit are close to 0.5 (table 4).

Although we find that the hypothesis of a spherical and spectrally uniform excess emission is in good agreement with the data, this does not exclude a more complicated morphology, a spatial dependence of the energy spectrum, or simultaneous contributions from

different physical mechanisms. The results shown in figure 19 suggest that an excess emission that becomes harder towards higher latitudes could easily be accommodated by the data. This would be relevant for explanations of the Galactic center excess in terms of the ICS emission (see section 6.1) from leptonic burst-like events.

Our results concerning the DM interpretation of the Galactic center excess are in reasonable agreement (at 95% CL) with most of the previous results from the inner Galaxy [55, 62] and Galactic center [65] analyses, however they are in slight tension (at 99% CL) with some result from the inner few degrees around the GC [54] (see section 6.2). Concerning the interpretation in terms of MSPs, the typically expected power-law with exponential cut-off spectrum is slightly disfavoured by the data, with a p -value of 0.16 (see discussion in section 6.1). Additionally, the magnitude of the excess emission and its extension up to latitudes of $\sim 15^\circ$ make the potential contribution of an unresolved MSP population towards the Galactic center even less significant than the quoted 5–10% upper limits discussed in refs. [68–70].

As mentioned above, we find that when we folded the strongly correlated residuals that are present along the Galactic disk back onto the GC, spectral fits in the inner Galaxy do not significantly discriminate between broken power-laws and DM related spectra for the Galactic center excess. Reducing these empirical model systematics, by improving our understanding of the residuals along the disk, is an important first step towards more reliable Galactic diffuse emission models for the inner Galaxy and a benchmark for future work, which might finally lead to a more precise determination of the Galactic center excess spectrum and morphology at high latitudes.

Acknowledgments. We thank Markus Ackermann, Luca Baldini, Sam McDermott, Douglas Finkbeiner, Dan Hooper, Tim Linden, Luigi Tibaldi, Tracy Slatyer, Meng Su, Piero Ullio and Neal Weiner for useful discussions. We thank Mark Lovell for the careful reading of the manuscript. This work makes use of SciPy [141], PyFITS²⁵, PyMinuit²⁶, IPython [142] and HEALPix [78]. This work has been supported by the US Department of Energy. F.C. acknowledges support from the European Research Council through the ERC starting grant WIMPs Kairos, P.I. G. Bertone.

²⁵http://www.stsci.edu/resources/software_hardware/pyfits

²⁶<http://code.google.com/p/pyminuit>

A Description of Galactic diffuse models

In this appendix we give in tables 5 and 6 all the parameters for the 60 Galactic diffuse models that we use to probe the range of uncertainties under the physical assumptions that could be relevant in the identification of the GC “GeV excess”.

The CR sources, as described in section 3.2, can have different radial distributions. We include this possibility by using the four source distributions (“SNR”, “Pls_L”, “Pls_Y” and “OB”) modeled from ref. [58]. The CR electron and proton injection spectra are assumed to be power-laws with indices α_e and α_p above rigidity breaks R_0^e and R_0^p respectively. The rigidity breaks are chosen to be in the narrow ranges of $2.18 < R_0^e < 3.05$ GV and $11.3 < R_0^p < 11.7$ GV. Below the rigidity breaks, CR electrons and protons are injected with power-laws of $\alpha_e^{\text{lowE}} = 1.6$ and $1.89 < \alpha_p^{\text{lowE}} < 1.96$. These injection spectra are normalized (N_e and N_p) at 34.5 and 100 GeV kinetic energies. For the diffusion scale heights and radii we use models from ref. [58], which considers ranges of $4 \leq z_D \leq 10$ kpc and for $20 \leq r_D \leq 30$ kpc. For the gasses, our spin temperature T_S choices are 150 K and 10^5 K, and E(B-V) magnitude cuts of 2 or 5 [58]. In addition, in converting the observed CO map to a H2 map for our own GDE models, we used the conversion factor X_{CO} profile of ref. [109]. Given that the 13 models from ref. [58] were compared to the full-sky data and thus could also probe the X_{CO} profile, each of these models has its own X_{CO} factor that we take as it is. The X_{CO} profile assumptions can have some impact on the overall GDE models, but given that they affect only the molecular hydrogen gas component, which is highly non-spherical and very concentrated towards the disk, they cannot compensate in any way for a spherically symmetric excess. For the 13 models that we used from ref. [58] and the re-naming of them see tables 5 and 7.

Using the webrun version of **Galprop v54**, we build GDE models that test the remaining uncertainties, i.e diffusion coefficient (for $z_D = 4$ kpc, $r_D = 20$ kpc), re-acceleration, convection, ISRF and B -field distributions. For the diffusion coefficient described in eq. 3.1, we vary the value of D_0 in the range of $2\text{--}60 \times 10^{28} \text{ cm}^2 \text{ s}^{-1}$. For the diffusive re-acceleration described in eq. 3.2, we vary the value of the Alfvén speed within 0 and 100 km s^{-1} . For the gradient of convection velocity dv/dz , we assume values between 0 and $500 \text{ km s}^{-1} \text{ kpc}^{-1}$. The Galactic magnetic field is described in eq. 3.3. In the “ B -field” column, the first three out of the nine digits refer to the $B_0 \times 10$ value in μG (thus 090 is $B_0 = 9 \mu\text{G}$), the next three to the $r_c \times 10$ in kpc and the last three to $z_c \times 10$ in kpc. We take combinations of B_0 , r_c and z_c that result in $5.8 \leq B(r=0, z=0) \leq 117 \mu\text{G}$, with the large range scaling of the B -field to be $5 \leq r_c \leq 10$ kpc and $1 \leq z_c \leq 2$ kpc. Finally, the ISRF model in the **Galprop** webrun has three multiplication factors, for the “optical”, “IR” and CMB components. We take the “optical” and “IR” factors to have values between 0.5–1.5 as our extreme options.

In figure 22, we show for all our 60 models the ratio of $TS(\text{model})/TS_{\text{min}}$, where TS_{min} refers to the TS of model F (which gives the best-fit to the data at all energies). We show that ratio for four different energy ranges that span the entire energy interval that we analyze. There are clear patterns in that ratio vs model, which are associated to the fact that GDE models with consecutive names may differ only by a specific subset of assumptions²⁷. As for the quality of the fit, our results depend at different levels on the various physical assumptions. More specifically:

- The results depend slightly on the assumptions regarding the CR source distribution, with the OB-star distribution being the least preferred.

²⁷The six models that are referred in the main text were chosen for simplicity to have names between A-F.

Name	z_D	D_0	v_A	dv/dz	Source	$\alpha_e(\alpha_p)$	$N_e(N_p)$	B -field	ISRF
A	4	5.0	32.7	50	SNR	2.43(2.47)	2.00(5.8)	090050020	1.36,1.36,1.0
B	4	28.0	31.0	0	SNR	2.43(2.39)	1.00(4.9)	105050015	1.4,1.4,1.0
C	4	5.0	32.7	0	SNR	2.43(2.39)	0.40(4.9)	250100020	1.0,1.0,1.0
D	4	5.2	32.7	0	SNR	2.43(2.39)	0.40(4.9)	050100020	0.5,0.5,1.0
E	4	2.0	32.7	0	SNR	2.43(2.39)	0.40(4.9)	050100020	1.0,1.0,1.0
F	6	8.3	32.7	0	Pls _L	2.42(2.39)	0.49(4.8)	050100020	1.0,1.0,1.0
G	6	7.9	35.4	0	Pls _L	2.42(2.39)	0.49(4.8)	050100020	1.0,1.0,1.0
H	6	7.4	33.0	0	Pls _L	2.42(2.39)	0.49(4.8)	050100020	1.0,1.0,1.0
I	6	8.8	39.6	0	Pls _L	2.42(2.39)	0.49(4.8)	050100020	1.0,1.0,1.0
J	10	10.3	32.2	0	Pls _L	2.44(2.39)	0.49(4.8)	050100020	1.0,1.0,1.0
K	10	9.0	28.6	0	OB	2.47(2.40)	0.53(5.1)	050100020	1.0,1.0,1.0
L	10	10.1	31.6	0	Pls _Y	2.45(2.39)	0.50(5.0)	050100020	1.0,1.0,1.0
M	10	9.8	30.8	0	SNR	2.46(2.39)	0.50(4.9)	050100020	1.0,1.0,1.0
N	8	8.5	30.9	0	SNR	2.45(2.39)	0.50(4.9)	050100020	1.0,1.0,1.0
O	6	7.1	31.9	0	SNR	2.44(2.39)	0.50(4.9)	050100020	1.0,1.0,1.0
P	4	5.2	32.7	0	SNR	2.43(2.39)	0.49(4.9)	050100020	1.0,1.0,1.0
Q	10	10.0	29.1	0	OB	2.46(2.39)	0.48(4.9)	050100020	1.0,1.0,1.0
R	10	10.6	31.1	0	Pls _L	2.44(2.39)	0.49(4.8)	050100020	1.0,1.0,1.0
S	4	5.2	32.7	0	SNR	2.43(2.39)	0.40(4.9)	050100020	1.0,1.0,1.0
T	4	8.0	32.7	0	SNR	2.43(2.39)	0.40(4.9)	050100020	1.0,1.0,1.0
U	4	12.0	32.7	0	SNR	2.43(2.39)	0.40(4.9)	050100020	1.0,1.0,1.0
V	4	20.0	32.7	0	SNR	2.43(2.39)	0.40(4.9)	050100020	1.0,1.0,1.0
W	4	40.0	32.7	0	SNR	2.43(2.39)	0.40(4.9)	050100020	1.0,1.0,1.0
X	4	60.0	32.7	0	SNR	2.43(2.39)	0.40(4.9)	050100020	1.0,1.0,1.0
Y	4	4.0	32.7	0	SNR	2.43(2.39)	0.40(4.9)	050100020	1.0,1.0,1.0
Z	4	3.0	32.7	0	SNR	2.43(2.39)	0.40(4.9)	050100020	1.0,1.0,1.0
GI	4	5.0	32.7	50	SNR	2.43(2.39)	0.40(4.9)	050100020	1.0,1.0,1.0
GII	4	5.0	32.7	100	SNR	2.43(2.39)	0.40(4.9)	050100020	1.0,1.0,1.0
GIII	4	5.0	32.7	200	SNR	2.43(2.39)	0.40(4.9)	050100020	1.0,1.0,1.0
GIV	4	5.0	32.7	500	SNR	2.43(2.39)	0.40(4.9)	050100020	1.0,1.0,1.0
GV	4	5.0	32.7	0	SNR	2.43(2.39)	0.40(4.9)	025100020	1.0,1.0,1.0
GVI	4	5.0	32.7	0	SNR	2.43(2.39)	0.40(4.9)	100100020	1.0,1.0,1.0
GVII	4	5.0	32.7	0	SNR	2.43(2.39)	0.40(4.9)	500100020	1.0,1.0,1.0
GVIII	4	5.0	0.0	0	SNR	2.43(2.39)	0.40(4.9)	050100020	1.0,1.0,1.0
GIX	4	5.0	16.0	0	SNR	2.43(2.39)	0.40(4.9)	050100020	1.0,1.0,1.0
GX	4	5.0	50.0	0	SNR	2.43(2.39)	0.40(4.9)	050100020	1.0,1.0,1.0
GXI	4	5.0	100.0	0	SNR	2.43(2.39)	0.40(4.9)	050100020	1.0,1.0,1.0
GXII	4	5.2	32.7	0	SNR	2.43(2.39)	0.40(4.9)	050100020	0.8,0.8,1.0
GXIII	4	5.2	32.7	0	SNR	2.43(2.39)	0.40(4.9)	050100020	1.2,1.2,1.0
GXIV	4	5.2	32.7	0	SNR	2.43(2.39)	0.40(4.9)	050100020	1.5,1.5,1.0

Table 5. Parameters of the 60 Galactic diffuse models. z_D is in kpc, D_0 is in units of $\times 10^{28} \text{cm}^3 \text{s}^{-1}$, v_A in km s^{-1} , dv/dz in $\text{km s}^{-1} \text{kpc}^{-1}$, $N_e(N_p)$ is in units of $\times 10^{-9}$ in $\text{cm}^{-2} \text{sr}^{-1} \text{s}^{-1} \text{MeV}^{-1}$ at E_{kin} of 34.5 (100) GeV. $\alpha_e(\alpha_p)$ is the electron (proton) injection index above rigidity of 2.18 (11.3) GV. All models assume $r_D = 20$ kpc apart from models “Q” and “R”, for which we take $r_D = 30$ kpc. In addition, all models have a spin temperature $T_S = 150$ K apart from “F” and “I” that have $T_S = 10^5$ K. Finally, all models have a magnitude cut in the E(B-V) of 5 apart from models “G” and “I” which have a magnitude cut of 2.

- The results depend significantly on the gas distribution, not favoring a magnitude cut of 2 in E(B-V) map.
- The diffusion scale heights of ~ 4 kpc and diffusion coefficients D_0 close to the relevant

Name	z_D	D_0	v_A	dv/dz	Source	$\alpha_e(p)$	$N_e(p)$	B -field	ISRF
GXV	4	5.8	33.0	0	SNR	2.43(2.39)	3.20(4.9)	140060020	1.2,1.2,1.0
GXVI	4	5.8	33.0	0	SNR	2.43(2.39)	3.20(4.9)	105050020	1.2,1.2,1.0
GXVII	4	5.8	33.0	0	SNR	2.43(2.39)	3.20(4.9)	170070020	1.2,1.2,1.0
GXVIII	4	5.8	33.0	0	SNR	2.43(2.39)	3.20(4.9)	105050030	1.2,1.2,1.0
GXIX	4	5.8	33.0	0	SNR	2.43(2.39)	3.20(4.9)	105050015	1.2,1.2,1.0
GXX	4	5.8	33.0	0	SNR	2.43(2.39)	3.20(4.9)	105050010	1.2,1.2,1.0
GXXI	4	10.0	33.0	0	SNR	2.43(2.39)	2.00(4.9)	105050015	1.2,1.2,1.0
GXXII	4	20.0	31.0	0	SNR	2.43(2.39)	1.00(4.9)	105050015	1.4,1.4,1.0
GXXIII	4	28.0	25.0	0	SNR	2.59(2.39)	1.20(3.4)	105050015	1.3,1.3,1.0
GXXIV	4	28.0	100.0	0	SNR	2.59(2.39)	1.20(3.4)	105050015	1.3,1.3,1.0
GXXV	4	28.0	25.0	200	SNR	2.59(2.39)	1.20(3.4)	105050015	1.3,1.3,1.0
GXXVI	4	2.0	25.0	0	SNR	2.59(2.39)	1.20(3.4)	105050015	1.3,1.3,1.0
GXXVII	4	28.0	25.0	0	SNR	2.59(2.39)	1.20(3.4)	105050015	0.5,0.5,1.0
GXXVIII	4	28.0	25.0	0	SNR	2.59(2.39)	1.20(3.4)	210050015	1.3,1.3,1.0
GXXIX	4	5.0	32.7	50	SNR	2.43(2.39)	2.0(4.9)	050100020	0.8,0.8,1.0
GXXX	4	5.0	32.7	50	SNR	2.43(2.39)	2.0(4.9)	060070020	1.0,1.0,1.0
GXXXI	4	5.0	32.7	50	SNR	2.43(2.39)	2.0(4.9)	090050020	1.0,1.0,1.0
GXXXII	4	5.0	32.7	50	SNR	2.43(2.39)	2.0(4.9)	090050020	1.36,1.36,1.0
GXXXIII	4	5.0	50.0	50	SNR	2.43(2.39)	2.0(4.9)	090050020	1.36,1.36,1.0
GXXXIV	4	5.0	80.0	50	SNR	2.43(2.39)	2.0(4.7)	090050020	1.36,1.36,1.0

Table 6. Continuing Table 5. z_D is in kpc, D_0 is in units of $\times 10^{28} \text{cm}^3 \text{s}^{-1}$, v_A in km s^{-1} , dv/dz in $\text{km s}^{-1} \text{kpc}^{-1}$, $N_e(N_p)$ in units of $\times 10^{-9}$ in $\text{cm}^{-2} \text{sr}^{-1} \text{s}^{-1} \text{MeV}^{-1}$ at E_{kin} of 34.5 (100) GeV. $\alpha_e(\alpha_p)$ is the injection index above rigidity of 2.18 (11.3) GV. All models shown in this table have $r_D = 20$ kpc, $T_S = 150$ K and a E(B-V) magnitude cut of 5.

Name in this paper	Name in [58]	Name in this paper	Name in [58]
F	$^S \text{L}^Z 6^R 20^T 100000^C 5$	M	$^S \text{S}^Z 10^R 20^T 150^C 5$
G	$^S \text{L}^Z 6^R 20^T 150^C 2$	N	$^S \text{S}^Z 8^R 20^T 150^C 5$
H	$^S \text{L}^Z 6^R 20^T 150^C 5$	O	$^S \text{S}^Z 6^R 20^T 150^C 5$
I	$^S \text{L}^Z 6^R 20^T 100000^C 2$	P	$^S \text{S}^Z 4^R 20^T 150^C 5$
J	$^S \text{L}^Z 10^R 20^T 150^C 5$	Q	$^S \text{O}^Z 10^R 30^T 150^C 5$
K	$^S \text{O}^Z 10^R 20^T 150^C 5$	R	$^S \text{L}^Z 10^R 30^T 150^C 5$
L	$^S \text{Y}^Z 10^R 20^T 150^C 5$		

Table 7. The 13 models that we used from ref. [58].

standard assumptions $\sim 5 \times 10^{28} \text{cm}^2 \text{s}^{-1}$ are preferred with values of much slower diffusion than that clearly disfavored.

- The TS ratio is insensitive to assumptions on convection with a very weak preference towards non zero values for dv/dz
- High values for the Alfvén speed give very poor TS ratio (and as a result ΔTS).
- ISRF model assumptions have a small impact on the TS ratio.
- A preference towards values of $\sim 50\text{--}100 \mu\text{G}$ in the amplitude of the B -field at the GC and with larger values for parameters r_c and z_c is observed.

Yet, we remind that these results come only from the study of the reference ROI: $2^\circ \leq |b| \leq 20^\circ$ and $|l| \leq 20^\circ$ and other constraints would need to be taken into account, together with

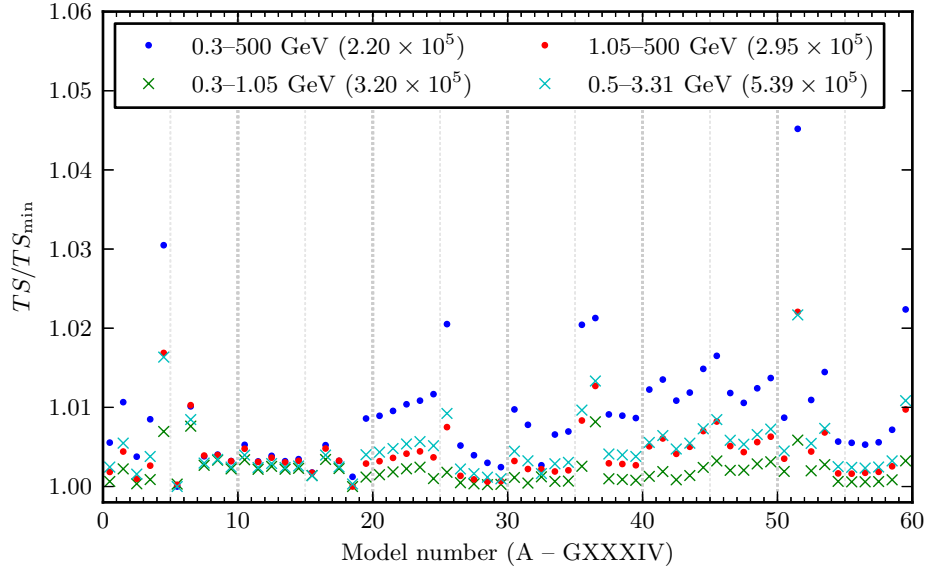


Figure 22. TS values of various GDE models used in this analysis, in different energy ranges, divided by the smallest TS value in that energy range (and indicated in the legend in parenthesis). The ordering is the same as in tables 5 and 6. Model F performs well in all energy ranges, and is used as a baseline best-fit model throughout this paper.

the fact that there are choices on the set of assumptions that lead to almost degenerate results.

Finally, in figure 23 we show the variation of the TS in function of the energy for model A and F when compared to the P6V11 diffuse model. The resulting ΔTS indicate that model A performs better than P6V11 at all energies above 1 GeV, while model F performs better than P6V11 in the entire energy range of interest.

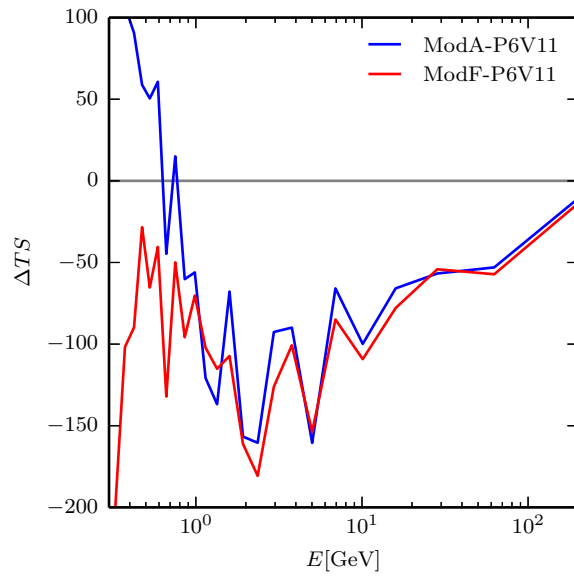


Figure 23. ΔTS value as function of energy, comparing model A and model F with the often adopted P6V11. At energies above 1 GeV, both of our models perform significantly better than P6V11 .

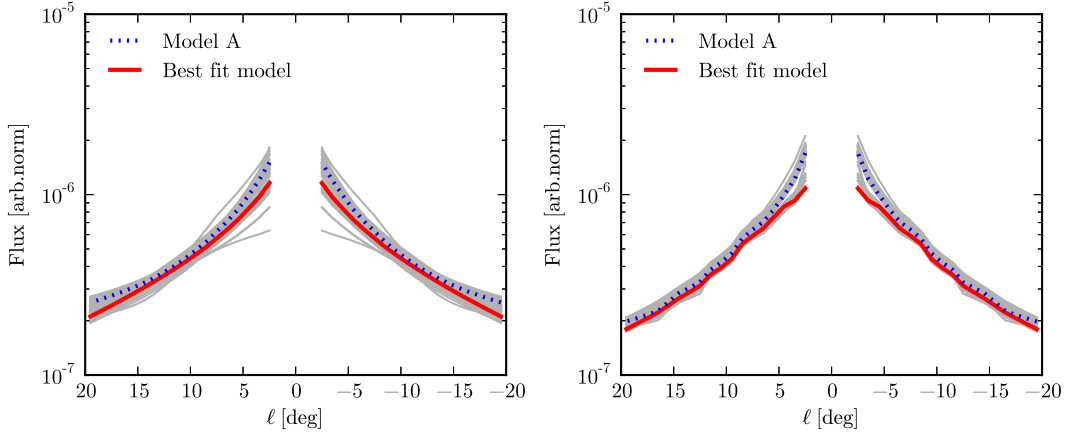


Figure 24. *Left panel:* Spread of latitude profile of ICS component for the 60 GDE models. The *red line* indicates the best-fit GDE model F. The *blue line* indicates the self-consistent GDE model A. *Right panel:* Same as left panel, but when allowing the ICS component at different latitudes to float freely (*ICS slicing*).

B Further properties of the Galactic center excess

B.1 Characterization of the morphology

We here further characterize the properties of the emission associated with the GCE template. We have seen in section 4.3 that introducing the ICS slicing helps in the determination of the morphology of the excess emission, that is expected to be much more susceptible to variations in the morphology of the GDE components. For all the results presented below the ICS slicing is applied. These additional degrees of freedom are indeed highly important in determining the profile slope. Nevertheless, we point out that this new freedom does not spoil the physical properties of the ICS emission associated to the GDE model. Figure 24 indeed confirms that allowing the ICS slices' normalizations to vary freely shrinks the dispersion due to the different GDE models but does not corrupt the latitude dependence of the ICS total flux. In figure 24 we show the measured latitude profile of the ICS component of all 60 GDE models without (left panel) and with (right panel) the slicing of the ICS component applied.

In order to investigate whether the GC excess is centered at the GC, we perform fits with a GCE template displaced along Galactic longitudes, with a displacement parameter $\Delta\ell$. The left panel of figure 25 shows the variation of the TS when moving the centre of the GCE template along ℓ for all of the 60 GDE models at 2 GeV in function of the displacement $\Delta\ell$. All 60 models indicate that the best value of the displacement parameter $\Delta\ell$ is about 0° , meaning that a GCE template centered at the GC (or slightly shifted at $\ell = 1^\circ$) is preferred. In the same panel the TS variation for different energies of the self-consistent GDE model is shown. At low energies the excess is centered at about the GC, while at high energies the morphology changes and the preferred displacement moves to $\ell \sim 4^\circ$. This general behavior holds for all analyzed models. Nevertheless, although the position with the minimum TS value moves to the west, the observed flux within the systematic uncertainties is consistent with being maximal at the GC at all energies.

In order to study the fall-off behavior of the GC excess emission, we examine how the

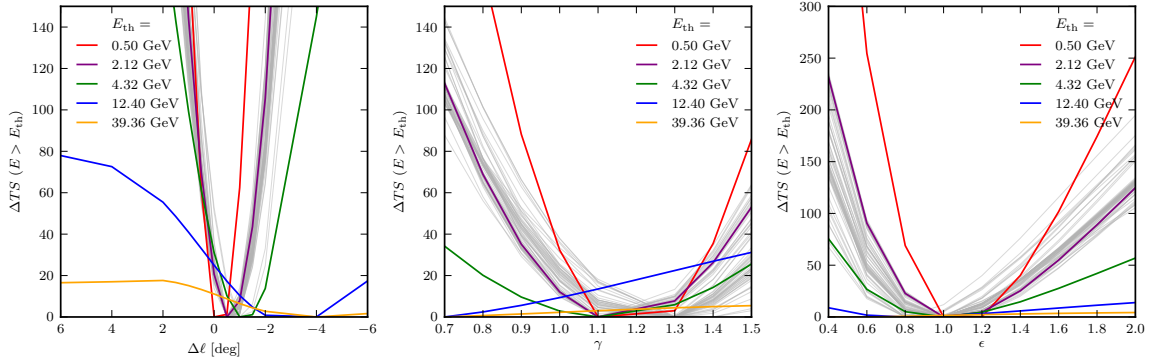


Figure 25. Using ICS latitude cuts, for the 60 GDE models (*gray lines*) and for model A (*colored lines*) at different energies we show in the *left panel* the variation of TS (ΔTS) as function of displacement of GC excess template. In the *central panel* the ΔTS as a function of slope of the GC excess template, γ . In the *right panel* the ΔTS as function of the elongation parameter ϵ .

quality of our fits changes when allowing the slope of the generalized NFW profile, γ , to vary in the range 0.7–1.5. In the central panel of figure 25, we show the resulting ΔTS as a function of the profile slope γ for all 60 GDE models at 2 GeV, when allowing the ICS component to vary as function of latitude as discussed above. In this case it is possible to constrain γ between 1.1 and 1.3 according to the results from all models. Overlaid in the same panel is the result for the self-consistent GDE model at different energies. As in the case of the displacement, at low energy (consistently for 0.5, 2, and 4 GeV) the fits prefers $\gamma = 1.1$, while the curves corresponding to higher energies do not constrain γ (at least in the range explored) mainly because of the lack of enough events.

Finally, in order to test the sphericity of the GC excess, we build templates that are elongated in a direction parallel to the disk or perpendicular to it. We parametrize the angle ξ of eq. 2.8 as $\cos \xi \equiv \cos b \cos(\ell/\epsilon)$, instead of the standard definition $\cos \xi \equiv \cos b \cos \ell$. Here, ϵ can be thought of as an effective “elongation scale factor”: $\epsilon < 1$ leads to an GC excess that is elongated perpendicularly to the Galactic disk, $\epsilon = 1$ corresponds to a spherical symmetric profile, and $\epsilon > 1$ stretches the profile along the direction of the disk. The right panel of figure 25 shows the variation of the TS value as function of the elongation scale factor ϵ for the different GDE models and for model A at different energies. Values of $\epsilon = 1$ are preferred at all energies and for all models.

We can thus conclude that we find the excess emission associated to the GCE template to be:

- Centered at the GC ($\ell \sim 0^\circ$);
- With a fall-off behavior in radius consistent with a generalized NFW profile with $\gamma=1.1$ –1.3;
- Not elongated in a direction parallel or perpendicular to the Galactic disk and, thus, most likely spherically symmetric.

B.2 Correlation with *Fermi* bubbles

The template associated to the *Fermi* bubbles is, as explained in section 2.3, a brightness-uniform template that covers the region where the bubbles are defined accordingly to ref. [24].

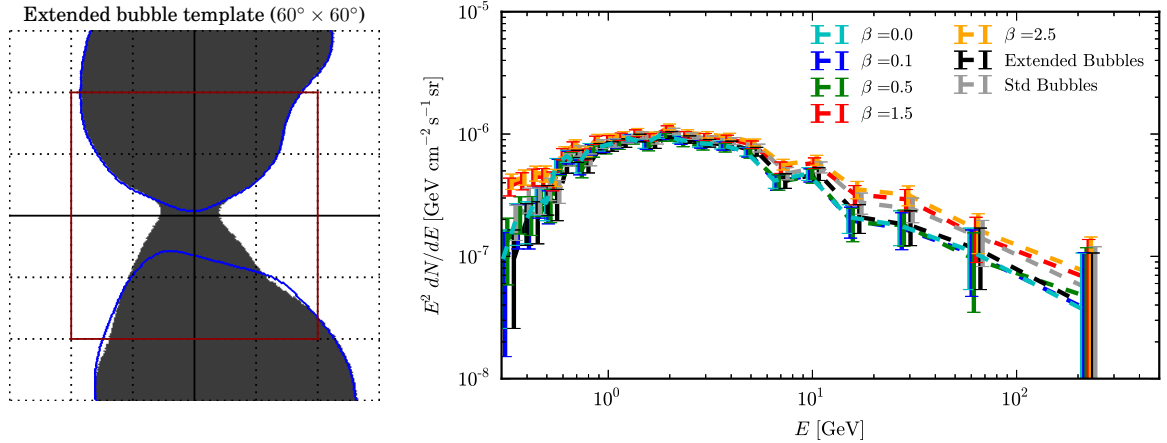


Figure 26. *Left panel:* Extended (shaded area) and standard (blue line, from ref. [24]) *Fermi* bubbles templates used in this work. The red square indicates our ROI. *Right panel:* Spectrum of GC excess when a latitude-dependent bubbles template is included in the fit (results are given for model A).

Latest studies of the *Fermi* bubbles reanalyzed this region and the emission associated to it [83]. The LAT Collaboration analysis cuts the disk at $|b| > 10^\circ$. Nevertheless, it is likely that the region of the bubbles extends down to the GC, also in the light of the possible astrophysical processes that have been attempted to explain this yet unknown emission, e.g. emission of a jet from the central black hole, wind from SN explosion close to the GC, 1st or 2nd order *Fermi* acceleration of CR electrons [143–147]. Therefore we consider also a new definition of the *Fermi* bubbles edges²⁸, that extends the bubbles down to the GC. This new region is displayed in figure 26, left panel, together with the contour of the bubbles region as defined in ref. [24]. The spectrum associated with the GCE template when the “extended” bubbles template is adopted is displayed in figure 26 (right panel). The new bubbles template is consistent with the “standard” one – i.e. used as standard working hypothesis – at low energies, $E \leq 5$ GeV, while it differs at high energies of about 30% at 100 GeV.

We then investigate the possibility that part of the emission absorbed by the GCE template, in particular the high energy end of the spectrum in figure 14, might be correlated spatially with the *Fermi* bubbles. To this end, we adopt an additional template for the bubbles (built from the new extended bubbles template and in addition to this one), allowing its intensity to be dependent on the latitude $\propto |b|^{-\beta}$, with $\beta < 1$ or $\beta > 1$. The emission absorbed by the GCE template when adding a latitude dependent template for the *Fermi* bubbles is shown in figure 26 for different values of the index β . By comparing the TS values of the different templates, it emerges that the fit prefers a template with a very mild latitude dependence, $\beta = 0.1$, as well as $\beta = 0$ and the extended bubbles template. The standard template adopted in the analysis is only slightly worse than the best-fit one ($\Delta TS = 32$), while $\beta \geq 0.5$ is highly disfavored by the fit ($\Delta TS \geq \mathcal{O}(100)$). This means that the GCE template does not lose too much power when using the latitude-dependent bubbles template, thus confirming the robustness of our results derived under the assumption of uniform-brightness template.

²⁸Meng Su, Private Communication.

C Systematic uncertainties

C.1 An analytical model for the empirical model uncertainty

In subsection 4.2 we estimated the model uncertainties from a fit to 22 test regions along the Galactic disk. The resulting fluctuations were shown in figure 12 in terms of mean and standard deviation (left panel), as well decomposed into their principal components (right panel). As can be seen from this plot, the first three principal components are sizeable and larger than or comparable to the statistical error, and appear to have a relatively well defined functional dependence on energy. We will show here that this functional dependence is actually expected as the result of uncertainties in the normalization and slope of the main background components ICS and π^0 +Bremss, and can be well fitted with a simple model.

We will start by assuming that the true background flux associated with component k in a given ROI is related to the measured background flux as determined by our template analysis by

$$\frac{dN_k^{\text{true}}}{dE} = (1 + \alpha_k) \left(\frac{E}{E_{\text{ref}}} \right)^{\gamma_k} \frac{dN_k}{dE}, \quad (\text{C.1})$$

where, α_k and γ_k are parameters that account for small corrections in the normalization and slope of the flux. These two parameters are unknown, but assumed to be normal distributed with mean zero and standard deviation $\Delta\alpha_k$ and $\Delta\gamma_k$.²⁹

We further assume that any mis-modeling of the background will be absorbed by the GCE template, hence

$$\frac{dN_{\text{GCE}}^{\text{true}}}{dE} = \left(1 - \sum_k \left(\alpha_k - \gamma_k \ln \frac{E}{E_{\text{ref}}} \right) \right) \frac{dN_{\text{GCE}}}{dE}, \quad (\text{C.2})$$

where we neglect second and higher order terms in α_k and γ_k . If only a fraction of mis-modeling is absorbed by the GCE template, this can be accounted for by a rescaling of $\Delta\alpha_k$ and $\Delta\gamma_k$.

The above uncertainty in the GCE spectrum corresponds to a correlation matrix with the simple form

$$\Sigma_{ij, \text{mod}} \simeq \sum_k \left(\Delta\alpha_k^2 + \Delta\gamma_k^2 \ln \frac{E_i}{E_{\text{ref}}} \ln \frac{E_j}{E_{\text{ref}}} \right) \frac{dN_k}{dE_i} \frac{dN_k}{dE_j}. \quad (\text{C.3})$$

This is true as long as the background variations can be modeled as a multivariate normal distribution, which requires here roughly $\Delta\alpha_k \lesssim 0.3$ and $\Delta\gamma_k \lesssim 0.1$, which we will find to be the case in the present situation.

The background fluxes are derived from the data in our baseline ROI. We will only take into account the dominant π^0 +Bremss and ICS components, and parametrize them analytically in the simple approximate form

$$\frac{dN_{\pi^0+B}}{dE} = 1.0 \times 10^{-5} \frac{x^{-2}}{\sqrt{x^{1.2} + x^{-0.4}}} \text{GeV}^{-1} \text{cm}^{-2} \text{s}^{-1} \text{sr}^{-1} \quad (\text{C.4})$$

²⁹Since the errors that we will discuss are typically very small, a more precise modeling of these uncertainties in terms of a e.g. log-normal distribution is not of relevance here.

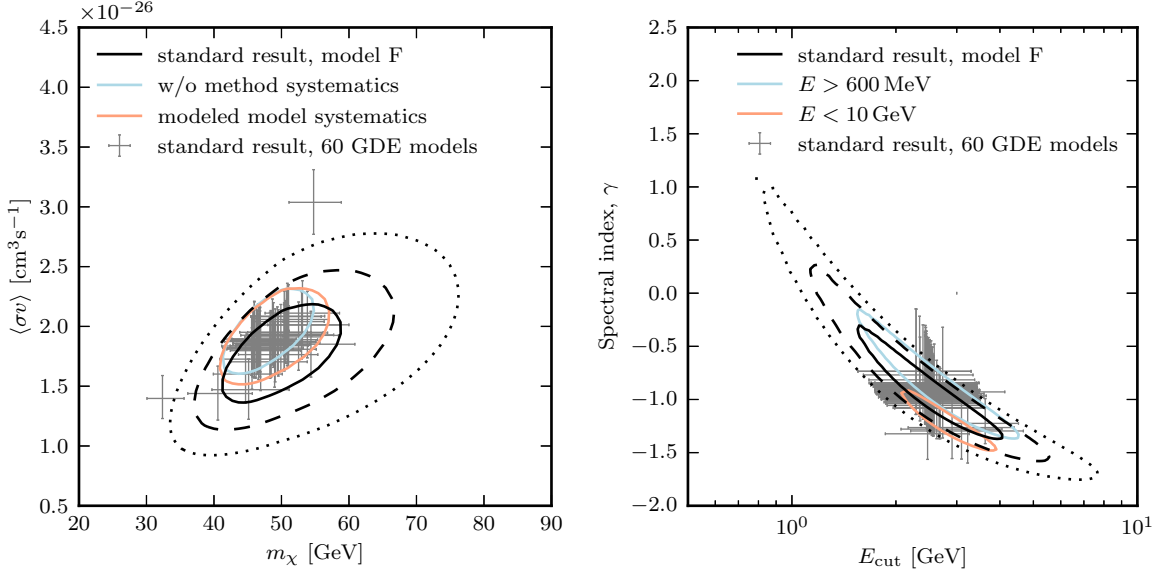


Figure 27. *Left panel:* Like left panel of figure 18 for $\bar{b}b$ final states (black contours, based on model F), but showing in addition the effect of modeling the background model systematics (light pink contour), of neglecting the method systematics (light blue contour), and the $\pm 1\sigma$ errors that one obtains for all of the 60 GDE (gray crosses). *Right panel:* Like right panel of figure 20, but showing in addition the results in the case of restricted energy ranges in the fit (light blue and red curves; only 68% CL contours for clarity), and using the 60 GDE models instead (gray crosses).

and

$$\frac{dN_{\text{ICS}}}{dE} = 4.0 \times 10^{-6} x^{-2.3} \text{GeV}^{-1} \text{cm}^{-2} \text{s}^{-1} \text{sr}^{-1}, \quad (\text{C.5})$$

where $x \equiv E/1 \text{ GeV}$. This parametrization is sufficiently accurate for the present purpose. As pivot point for the variations we adopt $E_{\text{ref}} = 3 \text{ GeV}$, which is again not critical.

We then perform a simple χ^2 fit to the three principal components shown in figure 12, giving equal weight to every energy bin and all three components. As a result, we find the best-fit values $\Delta\alpha_{\pi^0+B} \simeq 0.031$, $\Delta\gamma_{\pi^0+B} \lesssim 10^{-4}$, $\Delta\alpha_{\text{ICS}} \simeq 0.025$ and $\Delta\gamma_{\text{ICS}} \simeq 0.0093$. The corresponding model predictions are again shown in figure 12, and provide overall a good description of the observed fluctuations.

Taking the above results at face value and referring to fluxes averaged over our baseline ROI as e.g. shown in figure 8, the impact of typical mis-modelling of the ICS or π^0+B components as observed along the Galactic plane is expected to affect the GCE spectrum only at the level of a few percent of the background components. Yet, since the background are one order of magnitude stronger, this effect can be still sizeable. In fact, it constitutes one of the major uncertainties when discussing spectral and morphological properties of the GCE excess.

C.2 Various method uncertainties

In figure 27 we show how our results are affected by the most critical analysis choices. In the left panel, we show a fit to the flux in figure 14 with a $\bar{b}b$ spectrum. We compare the results that we find for our baseline analysis choices with the results obtained when neglecting the

method uncertainty (cf. figure 13), or when adopting one of the other 59 GDE scenarios to model the backgrounds. We find that our results are largely consistent; outliers correspond to GDE models which give a particularly bad TS value.

In the right panel, we show how the fit of a power-law with exponential cutoff is affected by various analysis choices (cf. figure 20). We show the contours that we obtain when excluding data below 600 MeV or above 10 GeV (only 68% CL contours for clarity), as well as the results obtained when using one of the other 59 GDE models. Again, our results remain consistent. Note that excluding data above 10 GeV has the effect of lowering the value of the spectral index γ . This can be understood by realizing that the power-law like behaviour of the GCE (see figure 14) at energies above 10 GeV prefers a larger subtraction of a smooth background (encoded in the correlated model uncertainties, see appendix. C.1) when fitted with an exponential cutoff. This subtraction necessarily affects the flux below 1 GeV and makes the spectrum harder.

D Miscellaneous

In figure 28, we show the spectra of the individual background components, as observed in each of the ten segments, for all 60 GDE models. We observe only small variations in the main GDE components, with the largest variations at low energies in the subdominant *Fermi* bubbles and the isotropic emissions. For reference, we also show the GC excess spectrum for *one* of the GDE models (model F); the envelope for all other models is shown in figure 16.

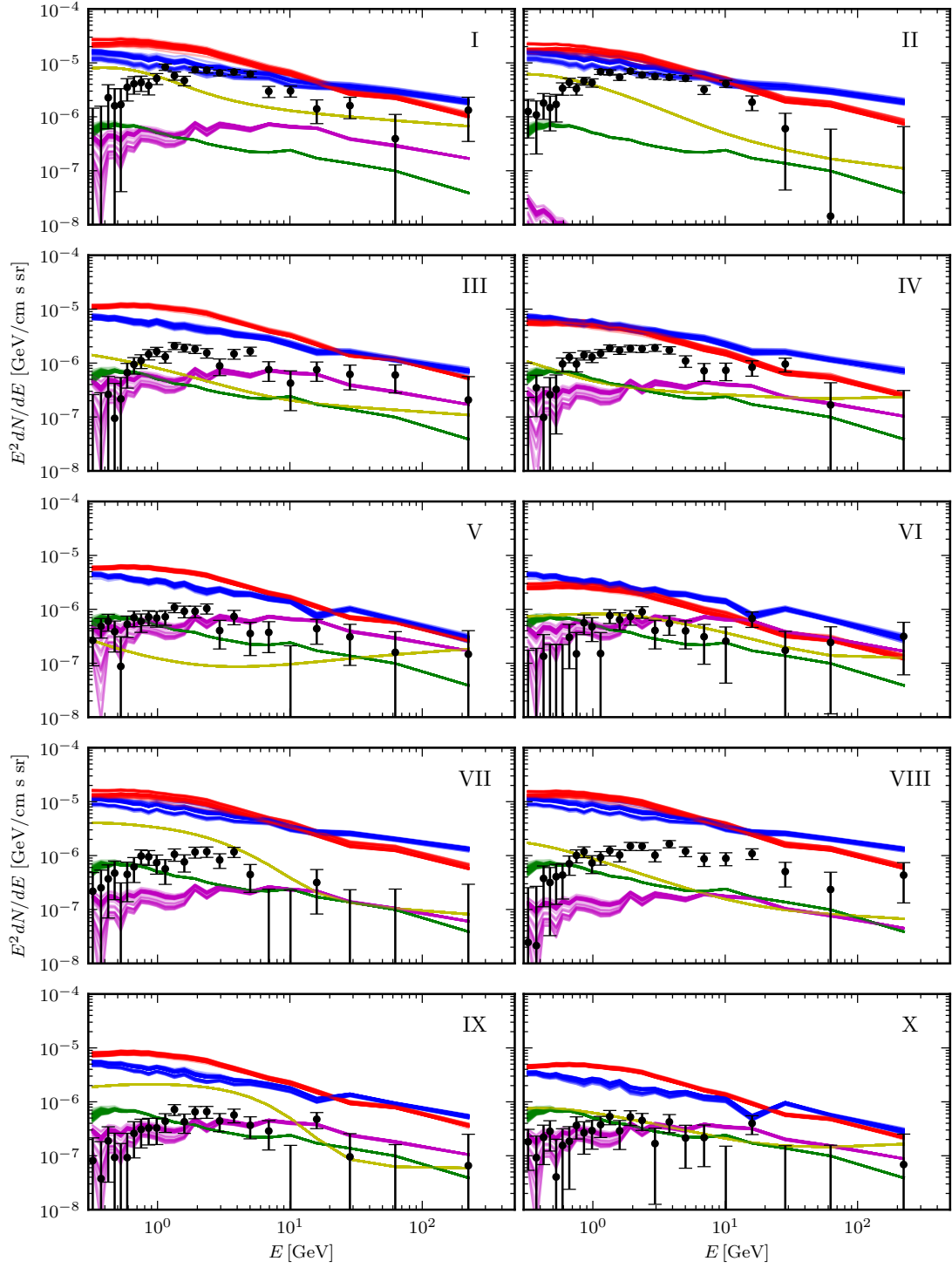


Figure 28. Energy spectra of the different background components (π^0 +Bremss, ICS, the isotropic, bubbles, PSCs) in the template fit, for *all* 60 GDE models, averaged over the segments shown in figure 15. The color coding is the same as in figure 8. The black points show the results for the GC excess for model F, as in figure 16.

References

- [1] **PAMELA** Collaboration, S. Orsi, *PAMELA: A payload for antimatter matter exploration and light nuclei astrophysics*, *Nucl. Instrum. Meth.* **A580** (2007) 880–883.
- [2] **PAMELA** Collaboration, P. Carlson, *PAMELA science*, *Int. J. Mod. Phys.* **A20** (2005) 6731–6734.
- [3] www.ams02.org.
- [4] N. Gehrels and P. Michelson, *GLAST: the next-generation high energy gamma-ray astronomy mission*, *Astroparticle Physics* **11** (June, 1999) 277–282.
- [5] R. Rando and f. t. F. L. Collaboration, *Post-launch performance of the Fermi Large Area Telescope*, [arXiv:0907.0626](https://arxiv.org/abs/0907.0626).
- [6] **WMAP** Collaboration, C. Bennett *et. al.*, *Nine-Year Wilkinson Microwave Anisotropy Probe (WMAP) Observations: Final Maps and Results*, *Astrophys.J.Suppl.* **208** (2013) 20, [[arXiv:1212.5225](https://arxiv.org/abs/1212.5225)].
- [7] **Planck Collaboration** Collaboration, J. Tauber *et. al.*, *The Scientific programme of Planck*, [astro-ph/0604069](https://arxiv.org/abs/astro-ph/0604069).
- [8] K. A. Eriksen, J. P. Hughes, C. Badenes, R. Fesen, P. Ghavamian, *et. al.*, *Evidence For Particle Acceleration to the Knee of the Cosmic Ray Spectrum in Tycho’s Supernova Remnant*, [arXiv:1101.1454](https://arxiv.org/abs/1101.1454).
- [9] C. Winkler, T.-L. Courvoisier, G. Di Cocco, N. Gehrels, A. Gimenez, *et. al.*, *The INTEGRAL mission*, *Astron.Astrophys.* **411** (2003) L1–L6.
- [10] **MAGIC Collaboration** Collaboration, J. Albert *et. al.*, *Observation of gamma-rays from the galactic center with the magic telescope*, *Astrophys.J.* **638** (2006) L101–L104, [[astro-ph/0512469](https://arxiv.org/abs/astro-ph/0512469)].
- [11] **H.E.S.S. Collaboration** Collaboration, F. Aharonian *et. al.*, *A New population of very high energy gamma-ray sources in the Milky Way*, *Science* **307** (2005) 1938–1942, [[astro-ph/0504380](https://arxiv.org/abs/astro-ph/0504380)].
- [12] **VERITAS Collaboration** Collaboration, V. Acciari *et. al.*, *Observation of Extended VHE Emission from the Supernova Remnant IC 443 with VERITAS*, *Astrophys.J.* **698** (2009) L133–L137, [[arXiv:0905.3291](https://arxiv.org/abs/0905.3291)].
- [13] **IceCube Collaboration** Collaboration, M. Aartsen *et. al.*, *Observation of High-Energy Astrophysical Neutrinos in Three Years of IceCube Data*, [arXiv:1405.5303](https://arxiv.org/abs/1405.5303).
- [14] Q. Yuan, S. Liu, Z. Fan, X. Bi, and C. L. Fryer, *Modeling the Multi-Wavelength Emission of Shell-Type Supernova Remnant RX J1713.7-3946*, *Astrophys.J.* **735** (2011) 120, [[arXiv:1011.0145](https://arxiv.org/abs/1011.0145)].
- [15] T. Tanaka, A. Allafort, J. Ballet, S. Funk, F. Giordano, *et. al.*, *Gamma-Ray Observations of the Supernova Remnant RX J0852.0-4622 with the Fermi LAT*, *Astrophys.J.* **740** (2011) L51, [[arXiv:1109.4658](https://arxiv.org/abs/1109.4658)].
- [16] D. Castro, P. Slane, D. C. Ellison, and D. J. Patnaude, *Fermi-LAT Observations and A Broadband Study of Supernova Remnant CTB 109*, *Astrophys.J.* **756** (2012) 88, [[arXiv:1207.1432](https://arxiv.org/abs/1207.1432)].
- [17] E. Berezhko, L. Ksenofontov, and H. Voelk, *Nonthermal emission of supernova remnant SN 1006 revisited: theoretical model and the H.E.S.S. results*, *Astrophys.J.* **759** (2012) 12, [[arXiv:1209.2789](https://arxiv.org/abs/1209.2789)].
- [18] D. Castro, P. Slane, A. Carlton, and E. Figueroa-Feliciano, *Fermi-LAT Observations of Supernova Remnants Interacting with Molecular Clouds: W41, MSH 17-39, and G337.7-0.1*,

- Astrophys.J.* **774** (2013) 36, [[arXiv:1305.3623](#)].
- [19] L. Saha, T. Ergin, P. Majumdar, M. Bozkurt, and E. Ercan, *Origin of gamma-ray emission in the shell of Cassiopeia A*, [arXiv:1401.5626](#).
 - [20] M. Cardillo, M. Tavani, A. Giuliani, S. Yoshiike, H. Sano, *et. al.*, *The Supernova Remnant W44: confirmations and challenges for cosmic-ray acceleration*, [arXiv:1403.1250](#).
 - [21] T. Fukuda, S. Yoshiike, H. Sano, K. Torii, H. Yamamoto, *et. al.*, *Interstellar protons in the TeV γ -ray SNR HESS J1731-347: Possible evidence for the coexistence of hadronic and leptonic γ -rays*, *Astrophys.J.* **788** (2014) 94, [[arXiv:1405.2599](#)].
 - [22] **The H. E. S. S. Collaboration, Fermi-LAT Collaboration** Collaboration, A. Abramowski *et. al.*, *Probing the gamma-ray emission from HESS J1834-087 using H.E.S.S. and Fermi LAT observations*, [arXiv:1407.0862](#).
 - [23] G. Dobler, D. P. Finkbeiner, I. Cholis, T. R. Slatyer, and N. Weiner, *The Fermi Haze: A Gamma-Ray Counterpart to the Microwave Haze*, *Astrophys.J.* **717** (2010) 825–842, [[arXiv:0910.4583](#)].
 - [24] M. Su, T. R. Slatyer, and D. P. Finkbeiner, *Giant Gamma-ray Bubbles from Fermi-LAT: AGN Activity or Bipolar Galactic Wind?*, *Astrophys. J.* **724** (2010) 1044–1082, [[arXiv:1005.5480](#)].
 - [25] D. P. Finkbeiner, *Microwave ism emission observed by wmap*, *Astrophys.J.* **614** (2004) 186–193, [[astro-ph/0311547](#)].
 - [26] G. Dobler and D. P. Finkbeiner, *Extended Anomalous Foreground Emission in the WMAP 3-Year Data*, *Astrophys.J.* **680** (2008) 1222–1234, [[arXiv:0712.1038](#)].
 - [27] **Planck Collaboration** Collaboration, P. Ade *et. al.*, *Planck Intermediate Results. IX. Detection of the Galactic haze with Planck*, [arXiv:1208.5483](#).
 - [28] **Fermi-LAT Collaboration** Collaboration, *The Fermi-LAT high-latitude Survey: Source Count Distributions and the Origin of the Extragalactic Diffuse Background*, *Astrophys.J.* **720** (2010) 435–453, [[arXiv:1003.0895](#)].
 - [29] M. Ajello, R. Romani, D. Gasparri, M. Shaw, J. Bolmer, *et. al.*, *The Cosmic Evolution of Fermi BL Lacertae Objects*, *Astrophys.J.* **780** (2014) 73, [[arXiv:1310.0006](#)].
 - [30] **Fermi LAT Collaboration** Collaboration, A. Abdo, *Detection of Gamma-Ray Emission from the Starburst Galaxies M82 and NGC 253 with the Large Area Telescope on Fermi*, *Astrophys.J.* **709** (2010) L152–L157, [[arXiv:0911.5327](#)].
 - [31] B. C. Lacki, T. A. Thompson, E. Quataert, A. Loeb, and E. Waxman, *On The GeV and TeV Detections of the Starburst Galaxies M82 and NGC 253*, *Astrophys.J.* **734** (2011) 107, [[arXiv:1003.3257](#)].
 - [32] **Fermi LAT Collaboration** Collaboration, M. Ackermann *et. al.*, *GeV Observations of Star-forming Galaxies with Fermi LAT*, *Astrophys.J.* **755** (2012) 164, [[arXiv:1206.1346](#)].
 - [33] **Fermi LAT collaboration** Collaboration, A. Abdo *et. al.*, *The First Fermi Large Area Telescope Catalog of Gamma-ray Pulsars*, *Astrophys.J.Suppl.* **187** (2010) 460–494, [[arXiv:0910.1608](#)].
 - [34] **The Fermi-LAT collaboration** Collaboration, A. Abdo *et. al.*, *The Second Fermi Large Area Telescope Catalog of Gamma-ray Pulsars*, *Astrophys.J.Suppl.* **208** (2013) 17, [[arXiv:1305.4385](#)].
 - [35] I. Cholis, D. Hooper, and T. Linden, *A New Determination of the Spectra and Luminosity Function of Gamma-Ray Millisecond Pulsars*, [arXiv:1407.5583](#).
 - [36] **Fermi-LAT collaboration** Collaboration, A. Abdo *et. al.*, *The Spectrum of the Isotropic Diffuse Gamma-Ray Emission Derived From First-Year Fermi Large Area Telescope Data*, *Phys.Rev.Lett.* **104** (2010) 101101, [[arXiv:1002.3603](#)].

- [37] M. Ackermann, *Intensity and origin of the extragalactic gamma-ray background*, 2012.
- [38] **Fermi LAT Collaboration** Collaboration, M. Ackermann *et. al.*, *Anisotropies in the diffuse gamma-ray background measured by the Fermi LAT*, *Phys.Rev.* **D85** (2012) 083007, [[arXiv:1202.2856](#)].
- [39] A. Cuoco, E. Komatsu, and J. Siegal-Gaskins, *Joint anisotropy and source count constraints on the contribution of blazars to the diffuse gamma-ray background*, *Phys.Rev.* **D86** (2012) 063004, [[arXiv:1202.5309](#)].
- [40] F. W. Stecker and T. M. Venters, *Components of the Extragalactic Gamma Ray Background*, *Astrophys.J.* **736** (2011) 40, [[arXiv:1012.3678](#)].
- [41] R. Makiya, T. Totani, and M. Kobayashi, *Contribution from Star-Forming Galaxies to the Cosmic Gamma-Ray Background Radiation*, *Astrophys.J.* **728** (2011) 158, [[arXiv:1005.1390](#)].
- [42] V. Berezhinsky, A. Gazizov, M. Kachelriess, and S. Ostapchenko, *Restricting UHECRs and cosmogenic neutrinos with Fermi-LAT*, *Phys.Lett.* **B695** (2011) 13–18, [[arXiv:1003.1496](#)].
- [43] M. Ahlers, L. Anchordoqui, M. Gonzalez-Garcia, F. Halzen, and S. Sarkar, *GZK Neutrinos after the Fermi-LAT Diffuse Photon Flux Measurement*, *Astropart.Phys.* **34** (2010) 106–115, [[arXiv:1005.2620](#)].
- [44] K. Murase, J. F. Beacom, and H. Takami, *Gamma-Ray and Neutrino Backgrounds as Probes of the High-Energy Universe: Hints of Cascades, General Constraints, and Implications for TeV Searches*, *JCAP* **1208** (2012) 030, [[arXiv:1205.5755](#)].
- [45] **Planck Collaboration** Collaboration, P. Ade *et. al.*, *Planck 2013 results. XVI. Cosmological parameters*, *Astron.Astrophys.* (2014) [[arXiv:1303.5076](#)].
- [46] G. Jungman, M. Kamionkowski, and K. Griest, *Supersymmetric dark matter*, *Phys.Rept.* **267** (1996) 195–373, [[hep-ph/9506380](#)].
- [47] G. Bertone, D. Hooper, and J. Silk, *Particle dark matter: Evidence, candidates and constraints*, *Phys.Rept.* **405** (2005) 279–390, [[hep-ph/0404175](#)].
- [48] L. Bergstrom, *Dark Matter Evidence, Particle Physics Candidates and Detection Methods*, *Annalen Phys.* **524** (2012) 479–496, [[arXiv:1205.4882](#)].
- [49] L. Goodenough and D. Hooper, *Possible Evidence For Dark Matter Annihilation In The Inner Milky Way From The Fermi Gamma Ray Space Telescope*, [[arXiv:0910.2998](#)].
- [50] D. Hooper and L. Goodenough, *Dark Matter Annihilation in The Galactic Center As Seen by the Fermi Gamma Ray Space Telescope*, *Phys.Lett.* **B697** (2011) 412–428, [[arXiv:1010.2752](#)].
- [51] D. Hooper and T. Linden, *On The Origin Of The Gamma Rays From The Galactic Center*, *Phys.Rev.* **D84** (2011) 123005, [[arXiv:1110.0006](#)].
- [52] K. N. Abazajian and M. Kaplinghat, *Detection of a Gamma-Ray Source in the Galactic Center Consistent with Extended Emission from Dark Matter Annihilation and Concentrated Astrophysical Emission*, *Phys.Rev.* **D86** (2012) 083511, [[arXiv:1207.6047](#)].
- [53] O. Macias and C. Gordon, *The Contribution of Cosmic Rays Interacting With Molecular Clouds to the Galactic Center Gamma-Ray Excess*, *Phys.Rev.* **D89** (2014) 063515, [[arXiv:1312.6671](#)].
- [54] K. N. Abazajian, N. Canac, S. Horiuchi, and M. Kaplinghat, *Astrophysical and Dark Matter Interpretations of Extended Gamma Ray Emission from the Galactic Center*, [[arXiv:1402.4090](#)].
- [55] T. Daylan, D. P. Finkbeiner, D. Hooper, T. Linden, S. K. N. Portillo, *et. al.*, *The Characterization of the Gamma-Ray Signal from the Central Milky Way: A Compelling Case for Annihilating Dark Matter*, [[arXiv:1402.6703](#)].

- [56] B. Zhou, Y.-F. Liang, X. Huang, X. Li, Y.-Z. Fan, *et. al.*, *GeV excess in the Milky Way: Depending on Diffuse Galactic gamma ray Emission template?*, [arXiv:1406.6948](#).
- [57] A. Boyarsky, D. Malyshev, and O. Ruchayskiy, *A comment on the emission from the Galactic Center as seen by the Fermi telescope*, *Phys.Lett.* **B705** (2011) 165–169, [[arXiv:1012.5839](#)].
- [58] **Fermi-LAT Collaboration** Collaboration, *Fermi-LAT Observations of the Diffuse Gamma-Ray Emission: Implications for Cosmic Rays and the Interstellar Medium*, *Astrophys.J.* **750** (2012) 3, [[arXiv:1202.4039](#)].
- [59] A. W. Strong, I. V. Moskalenko, and O. Reimer, *Diffuse galactic continuum gamma rays. A Model compatible with EGRET data and cosmic-ray measurements*, *Astrophys.J.* **613** (2004) 962–976, [[astro-ph/0406254](#)].
- [60] P. D. Serpico and G. Zaharijas, *Optimal angular window for observing Dark Matter annihilation from the Galactic Center region: the case of γ^- ray lines*, *Astropart.Phys.* **29** (2008) 380–385, [[arXiv:0802.3245](#)].
- [61] E. Nezri, J. Lavalle, and R. Teyssier, *Indirect dark matter searches: towards a consistent top-bottom approach for studying the gamma-ray signals and associated backgrounds*, *Phys.Rev.* **D86** (2012) 063524, [[arXiv:1204.4121](#)].
- [62] D. Hooper and T. R. Slatyer, *Two Emission Mechanisms in the Fermi Bubbles: A Possible Signal of Annihilating Dark Matter*, *Phys.Dark Univ.* **2** (2013) 118–138, [[arXiv:1302.6589](#)].
- [63] W.-C. Huang, A. Urbano, and W. Xue, *Fermi Bubbles under Dark Matter Scrutiny. Part I: Astrophysical Analysis*, [arXiv:1307.6862](#).
- [64] K. N. Abazajian, *The Consistency of Fermi-LAT Observations of the Galactic Center with a Millisecond Pulsar Population in the Central Stellar Cluster*, *JCAP* **1103** (2011) 010, [[arXiv:1011.4275](#)].
- [65] C. Gordon and O. Macias, *Dark Matter and Pulsar Model Constraints from Galactic Center Fermi-LAT Gamma Ray Observations*, *Phys.Rev.* **D88** (2013) 083521, [[arXiv:1306.5725](#)].
- [66] Q. Yuan and B. Zhang, *Millisecond pulsar interpretation of the Galactic center gamma-ray excess*, [arXiv:1404.2318](#).
- [67] W. Wang, Z. Jiang, and K. Cheng, *Contribution to diffuse gamma-rays in the Galactic Center region from unresolved millisecond pulsars*, *Mon.Not.Roy.Astron.Soc.* **358** (2005) 263–269, [[astro-ph/0501245](#)].
- [68] D. Hooper, I. Cholis, T. Linden, J. Siegal-Gaskins, and T. Slatyer, *Millisecond pulsars Cannot Account for the Inner Galaxy’s GeV Excess*, *Phys.Rev.* **D88** (2013) 083009, [[arXiv:1305.0830](#)].
- [69] F. Calore, M. Di Mauro, and F. Donato, *Diffuse gamma-ray emission from galactic Millisecond Pulsars*, [arXiv:1406.2706](#).
- [70] I. Cholis, D. Hooper, and T. Linden, *Challenges in Explaining the Galactic Center Gamma-Ray Excess with Millisecond Pulsars*, [arXiv:1407.5625](#).
- [71] F. Yusef-Zadeh, J. W. Hewitt, M. Wardle, V. Tatischeff, D. A. Roberts, W. Cotton, H. Uchiyama, M. Nobukawa, T. G. Tsuru, C. Heinke, and M. Royster, *Interacting Cosmic Rays with Molecular Clouds: A Bremsstrahlung Origin of Diffuse High-energy Emission from the Inner 2deg \times 1deg of the Galactic Center*, *Astrophys.J.* **762** (Jan., 2013) 33, [[arXiv:1206.6882](#)].
- [72] T. Linden, E. Lovegrove, and S. Profumo, *The Morphology of Hadronic Emission Models for the Gamma-Ray Source at the Galactic Center*, *Astrophys.J.* **753** (2012) 41, [[arXiv:1203.3539](#)].
- [73] **H.E.S.S. Collaboration** Collaboration, F. Aharonian *et. al.*, *Discovery of very-high-energy*

- gamma-rays from the galactic centre ridge, *Nature* **439** (2006) 695–698, [[astro-ph/0603021](#)].
- [74] F. Yusef-Zadeh, J. Hewitt, M. Wardle, V. Tatischeff, D. Roberts, *et. al.*, *Interacting Cosmic Rays with Molecular Clouds: A Bremsstrahlung Origin of Diffuse High Energy Emission from the Inner 2deg by 1deg of the Galactic Center*, *Astrophys.J.* **762** (2013) 33, [[arXiv:1206.6882](#)].
 - [75] E. Carlson and S. Profumo, *Cosmic Ray Protons in the Inner Galaxy and the Galactic Center Gamma-Ray Excess*, [arXiv:1405.7685](#).
 - [76] J. Petrovic, P. D. Serpico, and G. Zaharijas, *Galactic Center gamma-ray "excess" from an active past of the Galactic Centre?*, [arXiv:1405.7928](#).
 - [77] S. K. N. Portillo and D. P. Finkbeiner, *Sharper Fermi LAT Images: instrument response functions for an improved event selection*, [arXiv:1406.0507](#).
 - [78] K. Gorski, E. Hivon, A. Banday, B. Wandelt, F. Hansen, *et. al.*, *HEALPix - A Framework for high resolution discretization, and fast analysis of data distributed on the sphere*, *Astrophys.J.* **622** (2005) 759–771, [[astro-ph/0409513](#)].
 - [79] W. Cash, *Parameter estimation in astronomy through application of the likelihood ratio*, *Astrophys.J.* **228** (1979) 939–947.
 - [80] **Fermi LAT Collaboration**, A. A. Abdo *et. al.*, *Fermi Large Area Telescope Second Source Catalog*, [arXiv:1108.1435](#).
 - [81] A. Franckowiak and M. D., *Spectrum of the fermi bubbles*, 2013.
 - [82] A. W. Strong, I. V. Moskalenko, and O. Reimer, *Diffuse continuum gamma-rays from the galaxy*, *Astrophys.J.* **537** (2000) 763–784, [[astro-ph/9811296](#)].
 - [83] **Fermi-LAT Collaboration** Collaboration, *The Spectrum and Morphology of the Fermi Bubbles*, [arXiv:1407.7905](#).
 - [84] C. Vera-Ciro, L. V. Sales, A. Helmi, and J. F. Navarro, *The shape of dark matter subhalos in the Aquarius simulations*, [arXiv:1402.0903](#).
 - [85] T. Kamae, N. Karlsson, T. Mizuno, T. Abe, and T. Koi, *Parameterization of gamma, e^+ - and neutrino spectra produced by $p\ p$ interaction in astronomical environment*, *Astrophys. J.* **647** (2006) 692–708, [[astro-ph/0605581](#)].
 - [86] S. R. Kelner, F. A. Aharonian, and V. V. Bugayov, *Energy spectra of gamma-rays, electrons and neutrinos produced at proton proton interactions in the very high energy regime*, *Phys. Rev.* **D74** (2006) 034018, [[astro-ph/0606058](#)].
 - [87] H. Koch and J. Motz, *Bremsstrahlung Cross-Section Formulas and Related Data*, *Rev.Mod.Phys.* **31** (1959) 920–955.
 - [88] R. J. Gould, *High-Energy Bremsstrahlung in Collisions of Electrons with One- and Two-Electron Atoms*, *Physical Review* **185** (Sept., 1969) 72–79.
 - [89] G. Blumenthal and R. Gould, *Bremsstrahlung, synchrotron radiation, and compton scattering of high-energy electrons traversing dilute gases*, *Rev.Mod.Phys.* **42** (1970) 237–270.
 - [90] F. C. Jones, *Calculated Spectrum of Inverse-Compton-Scattered Photons*, *Phys.Rev.* **167** (1968) 1159–1169.
 - [91] R. Trotta, G. Johannesson, I. Moskalenko, T. Porter, R. R. de Austri, *et. al.*, *Constraints on cosmic-ray propagation models from a global Bayesian analysis*, *Astrophys.J.* **729** (2011) 106, [[arXiv:1011.0037](#)].
 - [92] C. Evoli, D. Gaggero, D. Grasso, and L. Maccione, *Cosmic-Ray Nuclei, Antiprotons and Gamma-rays in the Galaxy: a New Diffusion Model*, *JCAP* **0810** (2008) 018, [[arXiv:0807.4730](#)].

- [93] I. Cholis and D. Hooper, *Constraining the origin of the rising cosmic ray positron fraction with the boron-to-carbon ratio*, *Phys.Rev.* **D89** (2014), no. 4 043013, [[arXiv:1312.2952](#)].
- [94] I. Cholis, M. Tavakoli, C. Evoli, L. Maccione, and P. Ullio, *Diffuse Galactic Gamma Rays at intermediate and high latitudes. I. Constraints on the ISM properties*, *JCAP* **1205** (2012) 004, [[arXiv:1106.5073](#)].
- [95] A. Hryczuk, I. Cholis, R. Iengo, M. Tavakoli, and P. Ullio, *Indirect Detection Analysis: Wino Dark Matter Case Study*, [arXiv:1401.6212](#).
- [96] C. Evoli, I. Cholis, D. Grasso, L. Maccione, and P. Ullio, *Antiprotons from dark matter annihilation in the Galaxy: astrophysical uncertainties*, *Phys.Rev.* **D85** (2012) 123511, [[arXiv:1108.0664](#)].
- [97] M. Cirelli and G. Giesen, *Antiprotons from Dark Matter: Current constraints and future sensitivities*, *JCAP* **1304** (2013) 015, [[arXiv:1301.7079](#)].
- [98] M. Cirelli, D. Gaggero, G. Giesen, M. Taoso, and A. Urbano, *Antiproton constraints on the GeV gamma-ray excess: a comprehensive analysis*, [arXiv:1407.2173](#).
- [99] I. Cholis and D. Hooper, *Dark Matter and Pulsar Origins of the Rising Cosmic Ray Positron Fraction in Light of New Data From AMS*, *Phys.Rev.* **D88** (2013) 023013, [[arXiv:1304.1840](#)].
- [100] M. Tavakoli, I. Cholis, C. Evoli, and P. Ullio, *Constraints on dark matter annihilations from diffuse gamma-ray emission in the Galaxy*, *JCAP* **1401** (2014) 017, [[arXiv:1308.4135](#)].
- [101] H. Nakanishi and Y. Sofue, *Three-dimensional distribution of the ISM in the Milky Way Galaxy: 1. The HI disk*, *Publ.Astron.Soc.Jap.* **55** (2003) 191, [[astro-ph/0304338](#)].
- [102] M. Tavakoli, *Three Dimensional Distribution of Atomic Hydrogen in the Milky Way*, [arXiv:1207.6150](#).
- [103] M. Pohl, P. Englmaier, and N. Bissantz, *3D Distribution of Molecular Gas in the Barred Milky Way*, *Astrophys.J.* **677** (2008) 283–291, [[arXiv:0712.4264](#)].
- [104] G. Dobler, I. Cholis, and N. Weiner, *The Fermi Gamma-Ray Haze from Dark Matter Annihilations and Anisotropic Diffusion*, *Astrophys.J.* **741** (2011) 25, [[arXiv:1102.5095](#)].
- [105] D. Gaggero, L. Maccione, G. Di Bernardo, C. Evoli, and D. Grasso, *Three-Dimensional Model of Cosmic-Ray Lepton Propagation Reproduces Data from the Alpha Magnetic Spectrometer on the International Space Station*, *Phys.Rev.Lett.* **111** (2013), no. 2 021102, [[arXiv:1304.6718](#)].
- [106] A. W. Strong, I. V. Moskalenko, and V. S. Ptuskin, *Cosmic-ray propagation and interactions in the Galaxy*, *Ann.Rev.Nucl.Part.Sci.* **57** (2007) 285–327, [[astro-ph/0701517](#)].
- [107] <http://galprop.stanford.edu/>.
- [108] A. W. Strong, I. V. Moskalenko, T. A. Porter, n. J ohannesso, E. Orlando, D. W. Digel, and A. E. Vladimirov, *Galprop version 54: Explanatory supplement*, 2011.
- [109] A. Strong, I. Moskalenko, O. Reimer, S. Digel, and R. Diehl, *The distribution of cosmic-ray sources in the galaxy, gamma-rays, and the gradient in the co-to-h2 relation*, *Astron.Astrophys.* **422** (2004) L47–L50, [[astro-ph/0405275](#)].
- [110] T. A. Porter, I. V. Moskalenko, A. W. Strong, E. Orlando, and L. Bouchet, *Inverse Compton Origin of the Hard X-Ray and Soft Gamma-Ray Emission from the Galactic Ridge*, *Astrophys.J.* **682** (2008) 400–407, [[arXiv:0804.1774](#)].
- [111] R. M. Crocker, D. Jones, F. Melia, J. Ott, and R. J. Protheroe, *A lower limit of 50 microgauss for the magnetic field near the Galactic Centre*, *Nature* **468** (2010) 65, [[arXiv:1001.1275](#)].
- [112] G. L. Case and D. Bhattacharya, *A new sigma-d relation and its application to the galactic supernova remnant distribution*, *Astrophys.J.* **504** (1998) 761, [[astro-ph/9807162](#)].
- [113] D. Lorimer, A. Faulkner, A. Lyne, R. Manchester, M. Kramer, *et. al.*, *The Parkes multibeam*

- pulsar survey: VI. Discovery and timing of 142 pulsars and a Galactic population analysis, *Mon.Not.Roy.Astron.Soc.* **372** (2006) 777–800, [[astro-ph/0607640](#)].
- [114] I. Yusifov and I. Kucuk, *Revisiting the radial distribution of pulsars in the galaxy*, *Astron.Astrophys.* **422** (2004) 545–553, [[astro-ph/0405559](#)].
 - [115] L. Bronfman, S. Casassus, J. May, and L. Nyman, *The radial distribution of ob star formation in the galaxy*, [astro-ph/0006104](#).
 - [116] I. A. Grenier, J.-M. Casandjian, and R. Terrier, *Unveiling Extensive Clouds of Dark Gas in the Solar Neighborhood*, *Science* **307** (Feb., 2005) 1292–1295.
 - [117] D. J. Schlegel, D. P. Finkbeiner, and M. Davis, *Maps of dust IR emission for use in estimation of reddening and CMBR foregrounds*, *Astrophys.J.* **500** (1998) 525, [[astro-ph/9710327](#)].
 - [118] R. Jansson, G. R. Farrar, A. H. Waelkens, and T. A. Ensslin, *Constraining models of the large scale Galactic magnetic field with WMAP5 polarization data and extragalactic Rotation Measure sources*, *JCAP* **0907** (2009) 021, [[arXiv:0905.2228](#)].
 - [119] T. Dame, D. Hartmann, and P. Thaddeus, *The Milky Way in molecular clouds: A New complete co survey*, *Astrophys.J.* **547** (2001) 792–813, [[astro-ph/0009217](#)].
 - [120] S. Levshakov, C. Henkel, D. Reimers, M. Wang, R. Mao, *et. al.*, *Star-forming regions of the Aquila rift cloud complex. I. NH₃ tracers of dense molecular cores*, *Astron.Astrophys.* **553** (2013) A58, [[arXiv:1303.2052](#)].
 - [121] J. Knude, *2mass/Hipparcos Extinctions and Distances in the Serpens - Aquila Region.IV. Error Propagation. Individual stars and mean values*, [arXiv:1103.0455](#).
 - [122] T. P. Robitaille and B. A. Whitney, *The present-day star formation rate of the Milky-Way determined from Spitzer detected young stellar objects*, *Astrophys.J.* **710** (2010) L11–L15, [[arXiv:1001.3672](#)].
 - [123] P. Gondolo, J. Edsjo, P. Ullio, L. Bergstrom, M. Schelke, *et. al.*, *DarkSUSY: Computing supersymmetric dark matter properties numerically*, *JCAP* **0407** (2004) 008, [[astro-ph/0406204](#)].
 - [124] R. Voss and M. Gilfanov, *A study of the population of LMXBs in the bulge of M31*, *Astron.Astrophys.* (2006) [[astro-ph/0610649](#)].
 - [125] K. N. Abazajian and M. Kaplinghat, *Detection of a gamma-ray source in the Galactic Center consistent with extended emission from dark matter annihilation and concentrated astrophysical emission*, *Phys.Rev.* **D 86** (Oct., 2012) 083511, [[arXiv:1207.6047](#)].
 - [126] T. Bringmann, M. Vollmann, and C. Weniger, *Updated cosmic-ray and radio constraints on light dark matter: Implications for the GeV gamma-ray excess at the Galactic center*, [arXiv:1406.6027](#).
 - [127] **Fermi-LAT Collaboration** Collaboration, M. Ackermann *et. al.*, *Dark Matter Constraints from Observations of 25 Milky Way Satellite Galaxies with the Fermi Large Area Telescope*, *Phys.Rev.* **D89** (2014) 042001, [[arXiv:1310.0828](#)].
 - [128] I. Cholis and P. Salucci, *Extracting limits on Dark Matter annihilation from gamma-ray observations towards dwarf spheroidal galaxies*, *Phys.Rev.* **D86** (2012) 023528, [[arXiv:1203.2954](#)].
 - [129] A. Geringer-Sameth and S. M. Koushiappas, *Exclusion of canonical WIMPs by the joint analysis of Milky Way dwarfs with Fermi*, *Phys.Rev.Lett.* **107** (2011) 241303, [[arXiv:1108.2914](#)].
 - [130] F. Donato, D. Maurin, P. Brun, T. Delahaye, and P. Salati, *Constraints on WIMP Dark Matter from the High Energy PAMELA \bar{p}/p data*, *Phys. Rev. Lett.* **102** (2009) 071301, [[arXiv:0810.5292](#)].

- [131] I. Cholis, *New Constraints from PAMELA anti-proton data on Annihilating and Decaying Dark Matter*, *JCAP* **1109** (2011) 007, [[arXiv:1007.1160](#)].
- [132] L. Bergstrom, T. Bringmann, I. Cholis, D. Hooper, and C. Weniger, *New limits on dark matter annihilation from AMS cosmic ray positron data*, *Phys.Rev.Lett.* **111** (2013) 171101, [[arXiv:1306.3983](#)].
- [133] A. Ibarra, A. S. Lamperstorfer, and J. Silk, *Dark matter annihilations and decays after the AMS-02 positron measurements*, *Phys.Rev.* **D89** (2014) 063539, [[arXiv:1309.2570](#)].
- [134] I. Cholis, D. Hooper, and T. Linden, *A Critical Reevaluation of Radio Constraints on Annihilating Dark Matter*, [arXiv:1408.6224](#).
- [135] S. Galli, F. Iocco, G. Bertone, and A. Melchiorri, *CMB constraints on Dark Matter models with large annihilation cross-section*, *Phys.Rev.* **D80** (2009) 023505, [[arXiv:0905.0003](#)].
- [136] T. R. Slatyer, N. Padmanabhan, and D. P. Finkbeiner, *CMB Constraints on WIMP Annihilation: Energy Absorption During the Recombination Epoch*, *Phys.Rev.* **D80** (2009) 043526, [[arXiv:0906.1197](#)].
- [137] S. Galli, F. Iocco, G. Bertone, and A. Melchiorri, *Updated CMB constraints on Dark Matter annihilation cross-sections*, *Phys.Rev.* **D84** (2011) 027302, [[arXiv:1106.1528](#)].
- [138] C. Evoli, S. Pandolfi, and A. Ferrara, *CMB constraints on light dark matter candidates*, [arXiv:1210.6845](#).
- [139] L. Lopez-Honorez, O. Mena, S. Palomares-Ruiz, and A. C. Vincent, *Constraints on dark matter annihilation from CMB observations before Planck*, *JCAP* **1307** (2013) 046, [[arXiv:1303.5094](#)].
- [140] D. Hooper and T. Linden, *Origin of the gamma rays from the Galactic Center*, *Phys.Rev.* **D 84** (Dec., 2011) 123005, [[arXiv:1110.0006](#)].
- [141] E. Jones, T. Oliphant, P. Peterson, *et. al.*, *SciPy: Open source scientific tools for Python*, 2001.
- [142] F. Pérez and B. E. Granger, *IPython: a System for Interactive Scientific Computing*, *Comput. Sci. Eng.* **9** (2007), no. 3 21–29.
- [143] F. Guo and W. G. Mathews, *The Fermi Bubbles. I. Possible Evidence for Recent AGN Jet Activity in the Galaxy*, *Astrophys.J.* **756** (2012) 181, [[arXiv:1103.0055](#)].
- [144] F. Guo, W. G. Mathews, G. Dobler, and S. P. Oh, *The Fermi Bubbles II: The Potential Roles of Viscosity and Cosmic Ray Diffusion in Jet Models*, *Astrophys.J.* **756** (2012) 182, [[arXiv:1110.0834](#)].
- [145] R. M. Crocker and F. Aharonian, *The Fermi Bubbles: Giant, Multi-Billion-Year-Old Reservoirs of Galactic Center Cosmic Rays*, *Phys.Rev.Lett.* **106** (2011) 101102, [[arXiv:1008.2658](#)].
- [146] K. Cheng, D. Chernyshov, V. Dogiel, C.-M. Ko, and W.-H. Ip, *Origin of the Fermi Bubble*, *Astrophys.J.* **731** (2011) L17, [[arXiv:1103.1002](#)].
- [147] P. Mertsch and S. Sarkar, *Fermi gamma-ray ‘bubbles’ from stochastic acceleration of electrons*, *Phys.Rev.Lett.* **107** (2011) 091101, [[arXiv:1104.3585](#)].